Development of Chemical Sensors using Novel Infrared Sources

By

John R. Donohue B.Sc. (Hons)

A Thesis presented

to

Dublin City University

For The Degree Of Master of Science

Research Supervisor:

Prof. B.D. MacCraith,

School of Physical Sciences,

Dublin City University.

Jan 2006

Declaration

I hereby certify that this material, which I now submit for assessment on the programme of study leading to the award of M.Sc. is entirely my own work and has not been taken from the work of others, save and to the extent that such work has been cited and acknowledged within the text of my work.

Signed: John Donohue

ID No.: 51179288

Date: 23.1.06.

Contents

List of Figures

List of Tables

Abstract

Two chemical sensors based on the common principle of infrared spectroscopy using thulium doped zirconium fluoride glass and quantum cascade lasers are described. Exploiting optically absorbing molecular vibrations, IR optical sensors offer highly selective *in situ* sensing in compact packages.

The near infrared (NIR) fluorescence of the thulium doped zirconium fluoride (ZBLAN:Tm^{3+}) glass was characterised. A relative humidity sensor was developed using ZBLAN:Tm^{3+} fluorescence as a modulatable infrared spectroscopic source. The optical components, NIR detector, and detector electronics were integrated in an industrial prototype device. Relative humidity measurements were carried out to characterise the sensor.

Two quantum cascade lasers (QCLs) were used for sensing a number of analytes in the mid infrared (MIR) spectral range in a common-base optical configuration. The first laser, a distributed feedback device emitting at 6μm, was integrated into a silver halide optical fibre and a hollow waveguide, for liquid water and gaseous propylene sensing, respectively. The second laser, a Fabry-Perot device emitting at 5.625μm, was used for acetone, acetic acid and formaldehyde sensing using open path optical cells and a hollow waveguide. The second QCL was also used for the development of a pulse averaging and referencing system to eliminate sensor noise due to laser amplitude fluctuations.

Chapter 1

Introduction

1.1 Background

Optical spectroscopic sensing offers many advantages over alternative sensing methodologies. Compared to well-established statistical methods employed in industrial quality control, optical sensing offers total coverage of production line facilities allowing continuous *in situ* (non-invasive) monitoring. In the case of chemical sensing, optical sensing allows rapid and relatively straightforward sample analysis.

Through broadband absorption-based spectroscopic analysis, the entirety of a sample can be described provided all the components absorb at a particular frequency in the range emitted by the source. Particular optical absorptions can be selected for sensing to minimise cross-sensitivity with interfering components, thus allowing single frequency spectroscopy using coherent sources such as lasers. Optical absorptions due to molecular-specific vibrational and rotational electronic transitions in the mid infrared (MIR) spectral region are particularly well suited to this role.

In roles such as pollution monitoring and medical analysis, optical sensing can provide viable solutions for cases where rapid chemical analysis is vital. Sample pretreatment is rarely required, provided careful spectroscopic source selection and optical configuration design has been carried out. If a source, e.g. a laser, emits outside the atmospheric absorption windows, then ambient water vapour and carbon dioxide can interfere with sensing and steps such as nitrogen purging or dessication must be carried out. Incorrect selection of absorption feature and optical path length will limit the capability of the sensor. However, compared to other state-of-the-art methods such as gas chromatography-mass spectrometry (GCMS) or high pressure liquid chromatography (HPLC), optical sensing

provides sensitive and selective analysis without relying on sophisticated pre-treatment steps.

1.2 Optical Sources

Recently, many novel IR sources have been investigated for use in spectroscopic applications. Near infrared (NIR) sources, for probing the overtone or combination frequencies of fundamental absorptions, are limited by optical intensity instability in the case of light emitting diodes (LEDs), or a lack of available wavelengths to fully cover the region (as with NIR lasers). The MIR may be accessed using cryogenic lead-salt lasers, difference frequency generators, optical parametric oscillators, and doped fiber lasers.

A novel method to generate light over the NIR spectral range is via the fluorescence of rare-earth ions. The stable trivalently ionic states of most of the rare-earth elements fluoresce from the visible range up to 2.85μm (in the case of holmium, for example). The fluorescent $^3F_4 \rightarrow {}^3H_6$ transition of thulium (Tm^{3+}) centered at 1.83μm exhibits considerable spectral overlap with the $\nu_2 + \nu_3$ combination absorption of water. This effect is exploited in this work.

The quantum cascade laser (QCL), although only invented in 1994, has proven to be an invaluable addition to the MIR spectroscopist's armoury since it became commercially available at the beginning of the decade. Using electron transitions between closely spaced energy levels in the conduction band, thus avoiding bandgap recombinations between electrons and holes, and a cascading energy level scheme to achieve population inversion, high power MIR lasers have been developed. Through careful bandgap engineering and recent advances in semiconductor material processing technology, QCLs are now making an impact in many IR sensing applications.

1.3 Objectives

The objective of this thesis was to apply novel infrared optical sources to a variety of optical sensing applications. These included relative humidity (RH) sensing, monitoring the water content of solvents, and the detection of volatile organic compounds (VOCs) that are known to be present in exhaled human breath.

The modulated NIR fluorescence of thulium-doped fluorozirconate glass (known as ZBLAN:Tm^{3+}) was implemented into a sensor designed to detect relative humidity changes in nitrogen. The remit of this thesis was the further development

of proof-of-concept experiments, carried out prior to the author's involvement, to develop a prototype device suitable for industrial deployment.

In order to accomplish this, the optical configuration was redesigned to improve the sensor's characteristics. Changes in the detector and detection electronics were also investigated to optimise the sensor's response to changing relative humidities. Finally, a new sensing platform to accommodate the Tm^{3+}-doped fluorescence source, excitation laser, and IR detector in one discrete device was designed.

Two quantum cascade lasers, a distributed feedback laser operating at 6.0μm (DFB-QCL) and a Fabry-Perot device at 5.635μm (FP-QCL), were incorporated into a range of MIR sensing configurations using a common base approach for optical configuration. The objective here was to prove the viability of QCLs as MIR sources for a wide range of spectroscopic applications. Liquid and gas phase sensing experiments were carried out using open path cells, silver halide optical fibres, and hollow waveguides (silver and silver iodide-coated silica tubes with long optical path lengths).

For both sets of spectroscopic sensors (NIR fluorescence and MIR QCLs), it was required to construct calibration experiments to fully characterise each sensor's response to it's respective analyte. In the case of the NIR fluorescence RH sensor, N_2 humidifying and mixing with dry N_2 was sufficient, whereas the QCLs were designed to detect more volatile chemicals and required more specialised calibration standards.

A number of methods for reducing QCL intensity fluctuations were investigated. This was carried out to reduce spectroscopic absorbance noise arising from the intensity fluctuations. Methods applied included averaging and Gaussian and Lorentzian lineshape fitting. A program was instigated to determine if the QCL fluctuations could be referenced against pulse driver pulses that were found to exhibit similar amplitude fluctuations. QCL temperature fluctuations were minimised by maintaining a very short laser pulse duration (~20ns), thus reducing the current through the laser, as well as by implementing thermoelectric cooling using a Peltier cooler.

Chapter 2

Theoretical Background

2.1 Introduction to Spectroscopy

The birth of absorption spectroscopy is attributed to Joseph von Fraunhofer, who discovered dark lines in spectra taken of the sun. This had been previously noted over a decade before by William Wollaston when investigating the newly-discovered ultra violet region using narrow slits, but was never followed up. Fraunhofer noted that two of the dark lines coincided with that of a lamp flame, which was later determined to be due to sodium. Although never determining the actual source of these lines, this was the first detailed account of what became known as an *absorption spectrum* [1].

Some of the most noted physicists of the time picked up where Fraunhofer left off, igniting a flurry of spectroscopic research. Luminaries such as Brewster, Foucault, Bunsen and Kirchoff devoted themselves to unravelling the secrets hidden in light. The latter two worked laboriously at cataloguing an enormous range of chemicals and compounds by heating them in a flame and observing the resulting *emission spectra*, a technique discovered by John Herschel and W.H. Fox Talbot. They discovered that the spectral lines of a given element remained fixed (spectrally speaking) regardless of whatever compound it was in. They also explained Fraunhofer's lines in the solar spectrum as elements within the sun's atmosphere absorbing light emitted by the sun itself. They had laid the foundations for experimental spectroscopy.

Rigorous mathematical analysis of spectroscopic phenomena was carried out in order to explain the placing of spectral lines. Some empirical formulations were derived, the most prevalent of which was put forward by Johann Balmer. With it, he was successfully able to determine the spectral lines of atomic hydrogen,

$$\frac{1}{\lambda} = R\left(\frac{1}{4} - \frac{1}{n^2}\right) \tag{2.1}$$

where λ is the wavelength of light, n is an integer greater than 2, and R is a constant, later called the Rydberg constant. This however revealed little about the actual mechanism of spectroscopy.

It fell to Niels Bohr to accurately describe the inner workings of spectroscopy. Combining classical and quantum physics by quantising angular momentum and using classical expressions for the forces acting on an electron, he was able to derive fixed energy states for electrons [2]. Reasoning that absorption and emission are the results of electrons moving from one fixed energy state to another, he succeeded in developing a robust model that not only proved quantum theory was more than an abstract diversion and facilitated a new model of the atom, but solved the centuries-old puzzle of spectroscopy.

2.1.1 Analysis of Infrared Spectroscopy

The infrared spectral region was discovered by William Herschel in 1800 while investigating the heating properties of different colours of the visible spectrum [3]. A control thermometer he had placed outside the red region registered heating greater than in any of the colour regions. Since then, the infrared region has been loosely divided into three main regions, defined by wavelength: the near infrared (780nm–3μm), mid infrared (3–15μm), and far infrared (15–1000μm).

Although the Bohr model of the atom had revolutionised physics, due to it being based on the most primitive element (hydrogen) a number of refinements to the model had to be introduced to explain remaining phenomena. In the case of infrared spectroscopy, this involved the development of a model to adequately describe molecular vibrations. Selected aspects of the quantum mechanical model are discussed with their relation to infrared absorption spectroscopy. A more detailed analysis can be found in [4].

(a) Vibrational Modes

If the simple harmonic oscillator model of vibration is applied to the motion of a diatomic molecule, quantum mechanics defines the vibrational energy as

$$E_v = h\nu\left(n + \frac{1}{2}\right) \tag{2.2}$$

where n is the vibrational quantum number i.e. only vibrations of a fixed frequency or harmonic of that frequency would be allowed. Classically, a harmonic oscillator is defined by

$$F = -kx = m\left(\frac{d^2x}{dt^2}\right) \tag{2.3}$$

where the force F is directed towards the equilibrium position of mass m and k is the force constant. The frequency of oscillation is then given by

$$\nu_{osc} = \frac{1}{2\pi}\sqrt{\frac{k}{m}} \tag{2.4}$$

The restoring force can be expressed in terms of the potential energy of the system V by

$$F = -\frac{dV}{dx} \tag{2.5}$$

and therefore the classical potential energy for a harmonic oscillator is derived from (2.3)

$$-\frac{dV}{dx} = -kx \tag{2.6}$$

$$V = k\int x dx \tag{2.7}$$

$$V = \frac{1}{2}kx^2 \tag{2.8}$$

However, this leads to the conclusion that the potential energy increases indefinitely with increasing displacement, and by implication so to does the restoring force. Experience contradicts this: at large distances, the interatomic force dwindles to practically zero (the molecule *dissociates*), and, as such, the potential energy is constant (Equation 2.5). The picture of the behaviour of a diatomic molecule is not complete; the simple harmonic oscillator model is not enough to fully explain the reality of the situation.

It is required to introduce *anharmonicity constants* and a higher order description of the potential curve to better describe the behaviour of the system. Therefore, the vibrational energy levels in a diatomic molecule now become

$$E_n = h\nu\left(n+\frac{1}{2}\right) + h\nu\chi\left(n+\frac{1}{2}\right)^2 + h\nu y\left(n+\frac{1}{2}\right)^3 + \ldots \tag{2.9}$$

where ν is the oscillation frequency, and χ and y are the higher order determinants describing the second and third order anharmonicity constants. In terms of wavenumbers (cm^{-1}) and defining $\bar{\nu_0} = \nu_0/c$, the equation can be expressed as

$$E_n = hc\bar{\nu_0}\left(n+\frac{1}{2}\right) + hc\bar{\nu_0}\left(n+\frac{1}{2}\right)^2\chi + hc\bar{\nu_0}\left(n+\frac{1}{2}\right)^3 y + \ldots \tag{2.10}$$

or by dividing across by hc, as

$$G(n) = \bar{\nu_0}\left(n+\frac{1}{2}\right) + \bar{\nu_0}\chi\left(n+\frac{1}{2}\right)^2 + \bar{\nu_0}y\left(n+\frac{1}{2}\right)^3 + \ldots \tag{2.11}$$

which describes the vibrational energy of an anharmonic oscillator.

For a simple harmonic oscillating molecule, the only vibrational transitions allowed are those that obey the vibrational selection rule

$$\Delta n = n' - n'' = \pm 1 \tag{2.12}$$

where n' and n'' are the vibrational quantum numbers of the initial and final states of the vibrational transition. In an anharmonically oscillating molecule, this rule no longer applies and electrons can move to any vibrational level, provided they have sufficient energy to do so. As the inter-vibrational energy spacings are generally larger than the thermal energy kT (k Boltzmann Constant, T temperature), the majority of electrons reside in the state defined by $n = 0$.

(b) Rotational Modes

If we consider two masses m_1 and m_2 rotating about an axis passing through their common centre of mass, and assume the separation of the masses remains constant (also known as a *rigid rotator*), the moment of inertia I is then given classically as

$$I = m_1 {r_1}^2 + m_2 {r_2}^2 \tag{2.13}$$

where r_1 and r_2 are the respective distances m_1 and m_2 are from their common centre of mass. If

$$r_1 = \frac{m_2}{m_1 + m_2} r \tag{2.14}$$

and

$$r_2 = \frac{m_1}{m_1 + m_2} r \tag{2.15}$$

where

$$r = r_1 + r_2 \tag{2.16}$$

then (2.13) becomes

$$I = \frac{m_1 m_2}{m_1 + m_2} r^2 \tag{2.17}$$

If $\frac{m_1 m_2}{m_1 + m_2} = \mu$, the reduced mass of the system, then (2.17) becomes

$$I = \mu r^2 \tag{2.18}$$

Classically the energy of this rotation is given by

$$E_r = \frac{I\omega^2}{2} = \frac{L^2}{2I} \tag{2.19}$$

where L is the angular momentum.

As quantum theory dictates that angular momentum is quantised, this implies that so too must the rotational kinetic energy of our diatomic molecule. The angular momentum is quantised as

$$L = \sqrt{J(J+1)}\,\hbar \tag{2.20}$$

where J is the rotational quantum number.

From (2.19), the rotational kinetic energy is now defined as

$$E_r[J] = \frac{J(J+1)\hbar^2}{2I} = \frac{J(J+1)\hbar^2}{2\mu r^2} \tag{2.21}$$

Letting $B = \frac{\hbar^2}{2\mu r^2}$, the rotational constant, (2.21) reduces to

$$E_r[J] = BJ(J+1) \tag{2.22}$$

Dividing across by hc, an expression in wavenumbers $F_{\tilde{\nu}}[J]$ is achieved, along with a new definition of the rotational constant B, for the rotational energy of a rigid rotator:

$$F_{\tilde{\nu}}[J] = \frac{E_r[J]}{hc} = B_{\nu} J(J+1) \tag{2.23}$$

$$B_{\tilde{\nu}} = \frac{\hbar^2/2\mu r^2}{hc} = \frac{h}{8\pi^2 c\mu r^2} \tag{2.24}$$

So far, the effect the molecules have on each other due to centrifugal force has not been accounted for. This comes about as a consequence of the molecules vibrating: clearly they cannot do so if held rigidly in place along their axis of vibration. As a consequence, the rigid rotator model must be changed to accommodate this, and so the non-rigid rotator model is introduced.

We assume that one of the molecules is stationary with regards to vibration (but still rotating), and that the other molecule is vibrating along the axis joining them. Consider now that the vibrating atom m_2 is displaced by an amount $r_c - r_e$ from its equilibrium position r_e. There now exists a restoring force

$$F_r = k(r_c - r_e) \tag{2.25}$$

that is balanced by the centrifugal force

$$F_c = \nu\omega^2 r_c \tag{2.26}$$

As $L = I\omega = \mu\omega {r_c}^2$ from (2.19),

$$L^2 = \mu r_c\,\omega^2 \cdot \mu {r_c}^3 = J(J+1)\,\hbar^2 \tag{2.27}$$

$$\Rightarrow F_c = \frac{L^2}{\mu {r_c}^3} = \frac{J(J+1)\hbar^2}{\mu {r_c}^3} \tag{2.28}$$

Equating F_r (2.25) and F_c (2.28), $r_c - r_e$ can be expressed in terms of J

$$r_c - r_e = \frac{J(J+1)\hbar^2}{k\mu {r_c}^3} \tag{2.29}$$

Thus, the rotational energy of this distorted molecule is now

$$E_{rot} = \underbrace{\frac{\hbar^2 J(J+1)}{2\mu {r_e}^2}}_{\text{rigid rotator (2.21)}} + \underbrace{\frac{k(r_c - r_e)^2}{2}}_{\text{non-rigid correction}} \tag{2.30}$$

The latter term in Equation 2.30 is derived from integrating F_r (2.25).

From Equation 2.29,

$$E_{rot} = \frac{\hbar^2 J(J+1)}{2\mu {r_e}^2} + \frac{k}{2}\left[\frac{J(J+1)\hbar^2}{k\mu {r_c}^3}\right]^2 \tag{2.31}$$

$$\Rightarrow E_{rot} = BJ(J+1) + D[J(J+1)]^2 \tag{2.32}$$

where B is the rotational constant defined earlier, and D is the *centrifugal constant.* In general, D is much smaller than B, and can be left out of further calculations.

The selection rule for rotational modes is

$$\Delta J = J' - J'' = \pm 1 \tag{2.33}$$

but the interaction of vibrations with rotations must be taken into account. This can be accomplished by defining α_e, the *vibration-rotation interaction constant,* and integrating it into the rotational constant by

$$B_{\bar{\nu}}(n) = B_{\bar{\nu}}(e) - \alpha_e(n + 1/2) + \ldots \tag{2.34}$$

where $B_{\nu}(e)$ is the hypothetical rotational constant in the absence of vibration. Recall that for a rigid rotator

$$B_{\bar{\nu}} = \frac{h}{8\pi^2 \mu c {r_e}^2}$$

If the molecule is vibrating, then the interatomic spacing r_e is changing. Therefore

$$B_{\bar{\nu}}(n) = \frac{h}{8\pi^2 \mu c} \int \frac{1}{{r_e}^2} \tag{2.35}$$

Due to the anharmonicity of the vibration, the mean nuclear separation will be slightly greater than r_e. To a first approximation, this is solved by the introduction of α, and gives the value of the rotational constant B_v in the vibrational state as

$$B_{\bar{\nu}}(n) = B_{\bar{\nu}}(e) - \alpha(n + 1/2) \tag{2.36}$$

Similarly, D has an additional term which is used to help define it in a vibrational state

$$D_{\bar{\nu}}(n) = D_{\bar{\nu}}(e) - \beta(n + 1/2) + \ldots \tag{2.37}$$

We can ignore it however, as $D_{\bar{\nu}}(n)$ is very small compared to $B_{\bar{\nu}}(n)$. Thus, the rotational energy of an atom is given by

$$F[J] = B_{\bar{\nu}}(n)J(J+1) \tag{2.38}$$

The change in energy of a purely rotational transition from one state J' to another J'' is given by

$$\Delta F[J] = F[J'] - F[J''] \tag{2.39}$$

$$= B_{\bar{\nu}}J'(J'+1) - B_{\bar{\nu}}J''(J''+1) \tag{2.40}$$

When a vibrational transition occurs, it is very often accompanied by a simultaneous rotational transition. Therefore the total change in energy of a $n' \rightarrow n''$ vibrational transition is defined as

$$\begin{aligned}
\Delta E &= \Delta G(n) + \Delta F[J] \\
&= G(n') - G(n'') + B_{\bar{\nu}}(n)J'(J'+1) - B_{\bar{\nu}}(n)J''(J''+1) \\
\Delta E_{v,r} &= [\bar{\nu_0}(n'+1/2) + \bar{\nu_0}\chi_e(n'+1/2)^2 + \bar{\nu_0}y_e(n'+1/2)^3 + \ldots] \\
&\quad -[\bar{\nu_0}(n''+1/2) + \bar{\nu_0}\chi_e(n''+1/2)^2 + \bar{\nu_0}y_e(n''+1/2)^3 + \ldots] \\
&\quad +B_{\bar{\nu}}(n')J'(J'+1) - B_{\bar{\nu}}(n'')J''(J''+1)
\end{aligned}$$

where the adjusted rotational constant $B_{\bar{\nu}}(n'')$ accounts for the fact that the molecule most likely has a different moment of inertia in the new state than the old state:

$$B_{\bar{\nu}}(n') = \frac{h}{8\pi^2 cI'} \qquad \text{and} \qquad B_{\bar{\nu}}(n'') = \frac{h}{8\pi^2 cI''}$$

(c) Electronic Transitions and Spectra

The effect an electron changing energy states has on a molecule will now be discussed. When an electron changes orbit (an electronic transition), it usually causes the molecule to change its rotational and vibrational state simultaneously. The total change in energy can then be written as

$$\Delta E = (E_{e'} - E_{e''}) + (E_{v'} - E_{v''}) + (E_{r'} - E_{r''}) = h\bar{\nu} \tag{2.41}$$

i.e. the total energy change is equal to the sum of the electronic, vibrational and rotational energy change, where $\bar{\nu}$ is the frequency at which radiation is emitted or absorbed by the electronic transition.

As the molecule is vibrating anharmonically, the selection rule $\Delta n = \pm 1$ no longer applies. The rotational selection rule (Eq. 2.33) $\Delta J = \pm 1$ still applies i.e. J' can equal $J'' - 1$ or $J'' + 1$.

If we write $(E_{e'} - E_{e''}) + (E_{v'} - E_{v''})$ as $h\bar{\nu}_0 c$, where $\bar{\nu}_0$ is the frequency of the electronic-vibrational transition in wavenumbers (cm^{-1}), then (Eq. 2.41) can be rewritten as

$$\Delta E = h\bar{\nu}_0\, c + (E_{r'} - E_{r''}) \tag{2.42}$$

$$\frac{\Delta E}{hc} = \bar{\nu}_0 + B_{\bar{\nu}}(n')J'(J'+1) - B_{\bar{\nu}}(n'')J''(J''+1) \tag{2.43}$$

$$\Rightarrow \bar{\nu} = \bar{\nu}_0 + B'J'(J'+1) - B''J''(J''+1) \tag{2.44}$$

where ν gives the wavenumbers of the spectral lines for a transition between two given vibrational states v' and v''. For brevity, $B_{\bar{\nu}}(n')$ and $B_{\bar{\nu}}(n'')$ are expressed as B' and B'' respectively.

Consider the change in rotational states $J' = J'' + 1$ for a simultaneous electronic-vibrational transition: (Eq. 2.44) becomes

$$\bar{\nu} = \bar{\nu}_0 + B'(J''+1)(J''+2) - B''J''(J''+1) \tag{2.45}$$

$$= \bar{\nu}_0 + B'(J''^2 + 3J'' + 2) - B''(J''^2 + J'') \tag{2.46}$$

$$= \bar{\nu}_0 + 2B' + (3B' - B'')J'' + (B' - B'')J''^2 \tag{2.47}$$

As B' and B'' may differ due to I' and I'' in the different vibrational levels, this can lead to a rapid change in the size of the interval between successive lines. The series of lines generated when $J' = J'' + 1$ by Equation 2.47 is termed the **R branch**.

Similarly, the **P branch** denotes the series generated when $J' = J'' - 1$:

$$\bar{\nu} = \bar{\nu}_0 - (B' + B'')J'' + (B' - B'')J''^2 \tag{2.48}$$

There are now two series of lines for a given electron-vibrational transition.

$$J' = J'' + 1 \rightarrow \bar{\nu}_R = \bar{\nu}_0 + 2B' + (3B' - B'')J'' + (B' - B'')J''^2 \tag{2.49}$$

$$J' = J'' - 1 \rightarrow \bar{\nu}_P = \bar{\nu}_0 - (B' - B'')J'' + (B' - B'')J''^2 \tag{2.50}$$

Note that at large values of J'', the previously small $(B' - B'')J''^2$ factor may dominate if B' and B'' are significantly different. In the case of either branch, the spacing between adjacent line is no longer than $2B'$.

Infrared spectroscopic sensing can be implemented using either the vibrational or rotational absorptions. In cases where a spectroscopic source cannot be obtained to interrogate a particular vibration, rotational absorptions may suffice

to allow spectroscopic analysis of a molecule. Figure 2.1 shows a MIR spectrum of formaldehyde, where the R ($J' = J'' + 1$) and P ($J' = J'' - 1$) branches of rotational transitions are clearly visible either side of the main C=O vibrational transition.

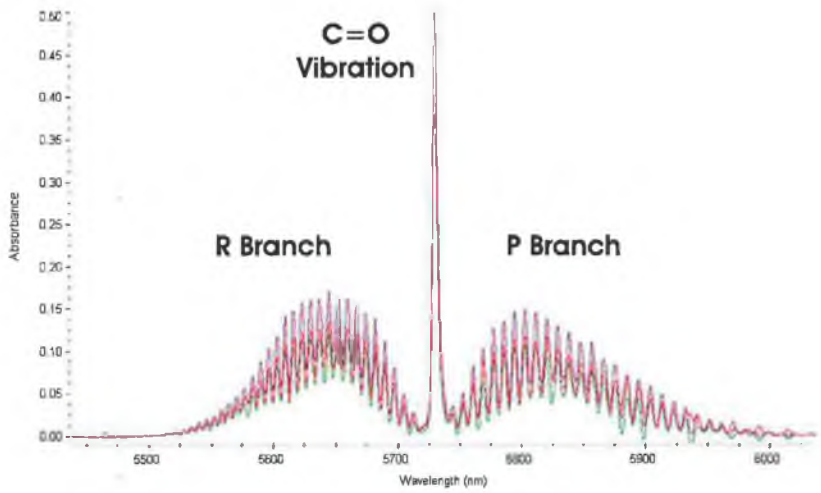

Figure 2.1: IR absorption spectrum of formaldehyde's C=O stretching vibration

While this section has detailed the spectral absorptions caused by vibrational and rotational transitions in a diatomic molecule, more complex polyatomic molecules still follow the above trend. The practical considerations for experimental spectroscopy in the two relevant optical regions are summarised in the following two sections.

2.1.2 Near Infrared Spectroscopy

Through both combination and overtone absorptions, the near infrared (NIR) spectral region can be used for spectroscopic sensing applications. Although the NIR absorptivity of chemicals is, generally speaking, weaker than in the mid infrared region, the combination of affordable sources and optics makes NIR spectroscopy an attractive option for remote sensing applications. NIR spectroscopy is not as molecularly selective as MIR owing to the superposition of combination and overtone absorptions.

In the case of water however, the absorption centered around 1.95μm can be readily used to monitor water concentrations in mixtures owing to the strength of that absorption relative to other chemicals. This particular absorption is the $\nu_2 + \nu_3$ combination band, comprising the ν_2 asymmetric stretch and the ν_3 bending vibration.

2.1.3 Mid Infrared Spectroscopy

The mid infrared (MIR) spectral region is associated with molecular vibrations, the resonance of which at particular frequencies gives rise to absorption of light. Although the optical absorption in this region is mainly due to vibrational resonances, the splitting of the vibrational energy levels into quantised rotational levels also contributes to optical absorption, as detailed in Section 2.1.1.

The importance of the MIR spectral region to sensor development can be attributed to what is termed the *fingerprint region* i.e. the range 6–20μm where water does not absorb and most basic molecules exhibit their fundamental vibrational absorptions. By using a broadband method like Fourier Transform IR spectroscopy (see Section 2.2.1), numerous components in a solution can be recognised by comparing the solution's spectrum with a library of reference spectra. This flexibility is countered by the size, cost and complexity of FTIR spectrometers. Conversely, using a single wavelength radiation source such as a laser will generally only allow a particular family of molecular species to be detected, but at far lower concentrations than FTIR.

2.2 Experimental Spectroscopy in the Infrared

Broadly speaking, two types of spectroscopy exist: absorption and emission. Absorption spectroscopy is based on the absorption of electromagnetic radiation by a material, and the resulting reduction in optical power is related to the amount of absorbing material in the beam path. Emission spectroscopy concerns the optical energy emitted from material that is excited.

Absorption spectroscopy covering a wide range of the electromagnetic spectrum the more commonly used technique. An advantage of absorption spectroscopy is that a background reading is easily recorded by simply removing the sample to be analysed from the beam path; another is that the sample does not require excitation to produce a spectrum. Figure 2.2 illustrates one of the most basic realisations of absorption spectroscopy, whereby the emission from a source is absorbed by a gas: I_0 and I represent the optical irradiances before and after absorption, respectively. The drop in optical intensity is sensed with a suitable detector, and the measured drop is related to the quantity of absorbing species in the gas.

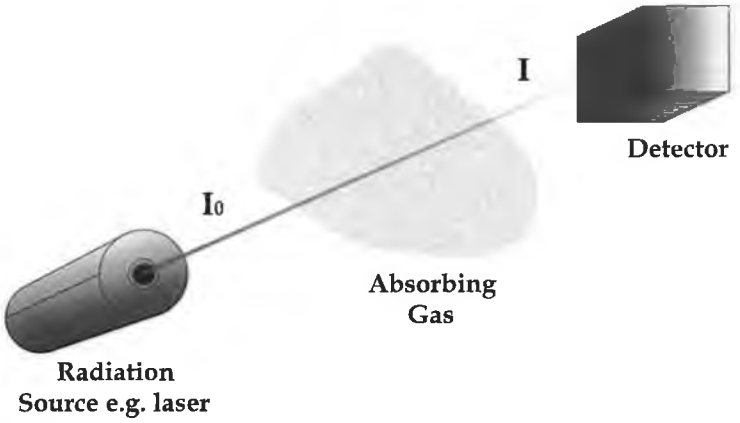

Figure 2.2: Schematic of absorption spectroscopy

This can be expressed mathematically if we consider an absorbing medium with a monochromatic beam passing through it. Assuming there is effectively only one allowed electron absorption, then the change in irradiance of the beam over a distance x can be expressed as

$$\Delta I(x) = I(x + \Delta x) - I(x) \tag{2.51}$$

$\Delta I(x)$ is proportional to the distance the beam passes through Δx and the original irradiance $I(x)$:

$$\Delta I(x) \propto I(x)\Delta x \tag{2.52}$$

Introducing the *absorption coefficient* α as a constant of proportionality, expressing Equation 2.52 as a differential equation, then integrating between the limits $[0, x]$ we get

$$\frac{dI(x)}{dx} = -\alpha I(x) \tag{2.53}$$

$$I(x) = I_0\, e^{-\alpha x} \tag{2.54}$$

where I_0 is the more widely-used term for $I(0)$ or the *incident irradiance.*

The absorption coefficient α is normally related to the concentration of a particular absorbing component through the *molar absorption coefficient* ϵ, a constant for a given molecule at a given wavelength. As such, Equation 2.53 is normally rewritten as

$$dI = \left(\frac{\partial I}{\partial L}\right)_c dL + \left(\frac{\partial I}{\partial c}\right)_L dc \tag{2.55}$$

known also as the *Beer-Bernard Law*, which for a fixed absorber concentration c and over a fixed optical path length L has the solution of

$$I = I_0\, 10^{\epsilon c L} \tag{2.56}$$

where ϵ, c and L are expressed in Liter per mole per centimeter ($L\, mol^{-1} cm^{-1}$), mole per liter ($mol\, L^{-1}$), and centimeter (cm), respectively. The property A is defined as the *absorbance* of the absorber, and is given by

$$A = \log_{10} \frac{I_0}{I} = \epsilon c L \tag{2.57}$$

better known as the *Beer-Lambert Law.* This law is vital to spectroscopic analysis, as it states that the absorbance of a particular substance remains constant as long as its concentration and optical path length remain constant. Also, in a cell of fixed length, any change in the absorbance of a substance must be due to a change in concentration.

2.2.1 Broadband Spectroscopy

Broadband Spectroscopy is defined as spectroscopy where the emission of a continuous source over a spectral range is absorbed, producing an absorption spectrum. Typical broadband sources include tungsten halogen lamps, whereby an electric current excites electrons in the lamp bulb, inducing light emission.

While spectroscopy with a broadband source like a tungsten halogen lamp may be convenient by way of being low-cost and compact, it is very difficult to quantify the constituents of the absorbing material. As the broadband source is emitting

over a wide range of wavelengths, each wavelength is attenuated or transmitted depending on the absorbers. The total attenuation will be due to contributions from each absorbing species present, causing an intensity drop. One solution is to use Fourier Transform IR spectroscopy to generate useful absorbance versus frequency scans using a broadband source.

(a) Fourier Transform IR Spectroscopy

One of the most widely used analytical techniques used in absorption spectroscopy is Fourier Transform Infrared spectroscopy, more commonly known as *FTIR spectroscopy*. It is based on the two-beam interferometer developed by Michelson [5], shown schematically in Figure 2.3. The interferometer operates as follows: radia-

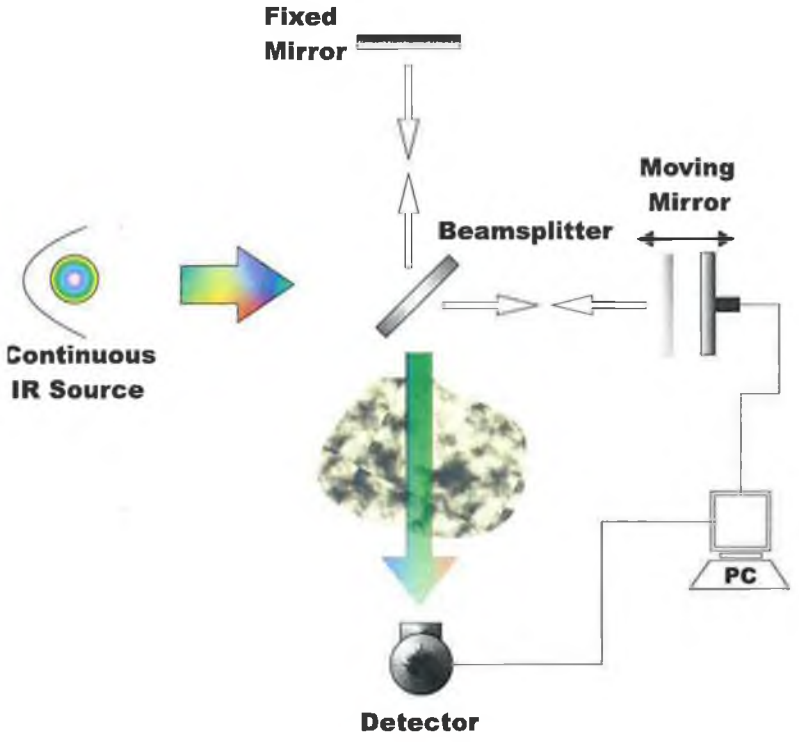

Figure 2.3: Schematic of FTIR spectrometer

tion from a continuous emitter is directed through a beamsplitter, one component directed towards a stationary mirror and the other towards a moving mirror. As the optical path length of the moving mirror arm is varying with respect to the stationary arm, constructive and destructive interference between the two reflected beams occurs at the beamsplitter. This results in a detector response of a series of wavelengths, and because the computer determines the rate at which the mirror oscillates, the wavelength at a given time can be calculated using

$$m\lambda = 2nd \tag{2.58}$$

where m is the number of interference fringes counted as the moving mirror scans through a distance d, λ is wavelength being determined, and n is the refractive index of the medium through which both beam paths travel (usually air; $n \approx 1$). The time-domain interferogram is stored and undergoes a Discrete Fourier Transformation (DFT) into a frequency-amplitude spectrum.

FTIR spectroscopy has the advantage of being able to probe a sample over the entirety of the MIR spectral region. By comparing the spectrum of a sample to a *background* scan, absorbing species in the parts-per-million (ppm) can be resolved. By using enhancement methods such as polymer enrichment layers, parts-per-billion (ppb) levels of detection can be attained [6]. However, the complexity of the system leads to significant costs and unsuitability for field deployment for remote sensing.

2.2.2 Coherent Source Spectroscopy

(a) Laser Absorption Spectroscopy

As an alternative to analysing the entire spectrum of a sample to determine its constituents, coherent source spectroscopy can be used if a particular constituent is under investigation. The infrared absorption of a given molecule is characteristic of that molecule and its vibrational states. If the molecule in question is part of a larger molecule, then the vibrational states are usually perturbed by a small amount. In this way, by knowing the absorbtion spectrum of a material and tailoring a single-frequency source to a particular and unique absorption, the concentration of that material can be measured spectroscopically. Lasers are particularly well suited to this branch of spectroscopy, having a very narrow band of frequencies. However, sourcing a laser with a spectral emission overlap for a particular molecular vibration is complicated by the fact that most of these vibrations absorb in the MIR, traditionally a spectral region with few available or convenient sources. Some of the best current solutions are described in Section 2.3.2 (a–d).

(b) Fibre-optic Evanescent Wave Spectroscopy

One aspect of absorption spectroscopy that is relevant to this work is Fibre-optic Evanescent Wave Spectroscopy (FEWS). An offshoot of attenuated total reflection (ATR) spectroscopy, interrogation of a sample outside a waveguide is accomplished through an effect of total internal reflection known as the *evanescent field.*

When electromagnetic radiation impinges on the boundary between two media of refractive indices n_1 and n_2 at an angle of incidence θ_i, a proportion of the radiation's energy is reflected back at θ_r while the remainder is transmitted into the second medium at θ_t (Fig. 2.4). These three beams are termed the *incident, reflected* and *transmitted rays*, respectively. A relationship between the angles

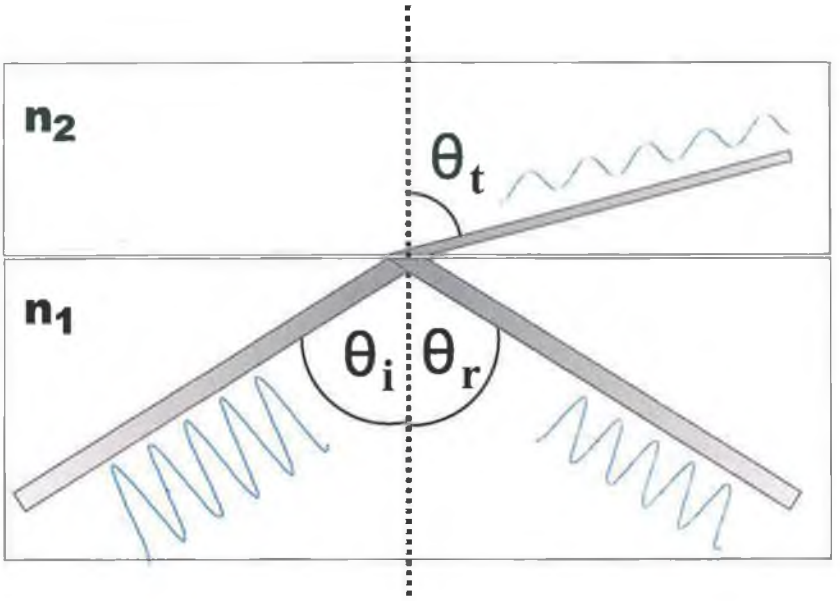

Figure 2.4: The splitting of light at the interface between two media

can be defined using The Law of Reflection (2.59) and Snell's Law (2.60):

$$\theta_i = \theta_r \tag{2.59}$$

$$n_1 \sin\theta_i = n_2 \sin\theta_t \tag{2.60}$$

The relationship between the incident radiation and its transmitted and reflected component are given by the Fresnel equations, which express the reflected and transmitted electric fields in terms of the incident electric field and account for field magnitudes parallel and perpendicular to the plane of incidence. Letting $\mathcal{E}_\parallel$ and $\mathcal{E}_\perp$ represent these magnitudes, and adhering to Maxwell's stipulation that they are continuous across the boundary, then the Fresnel equations can be written as [7]

$$\frac{\mathcal{E}_{\parallel,r}}{\mathcal{E}_{\parallel,i}} = \frac{n_1\cos\theta_t - n_2\cos\theta_i}{n_1\cos\theta_t + n_2\cos\theta_i} \tag{2.61}$$

$$\frac{\mathcal{E}_{\perp,r}}{\mathcal{E}_{\perp,i}} = \frac{n_1\cos\theta_i - n_2\cos\theta_t}{n_1\cos\theta_i + n_2\cos\theta_t} \tag{2.62}$$

$$\frac{\mathcal{E}_{\parallel,t}}{\mathcal{E}_{\parallel,i}} = \frac{2n_1\cos\theta_i}{n_1\cos\theta_t + n_2\cos\theta_i} \tag{2.63}$$

$$\frac{\mathcal{E}_{\perp,t}}{\mathcal{E}_{\perp,i}} = \frac{2n_1\cos\theta_i}{n_1\cos\theta_i + n_2\cos\theta_t} \tag{2.64}$$

For the case $n_1 > n_2$, there exists an angle of incidence known as the *critical angle* θ_c at which the refracted (transmitted) beam will travel along the plane of incidence ($\theta_t = 90°$). At angles of incidence greater than θ_c no component of the incident angle is transmitted into the second medium and *total internal reflection* occurs whereby almost all of the incident beam is reflected back at θ_r. Fundamental trigonometry gives

$$\cos\theta = \sqrt{1 - \sin^2\theta} \tag{2.65}$$

and as such Equation 2.60 can be rewritten as

$$\cos\theta_t = \sqrt{1 - \left(\frac{n_1}{n_2}\right)^2 \sin^2\theta_i} \tag{2.66}$$

an imaginary quantity when θ_i exceeds θ_c and $\sin\theta_i > n_2/n_1$. Equation 2.61 then becomes

$$\frac{\mathcal{E}_{\parallel,r}}{\mathcal{E}_{\parallel,i}} = \frac{n_1\left(\pm\imath\sqrt{\left(\frac{n_1}{n_2}\right)^2 \sin^2\theta_i - 1}\right) - n_2\cos\theta_i}{n_1\left(\pm\imath\sqrt{\left(\frac{n_1}{n_2}\right)^2 \sin^2\theta_i - 1}\right) + n_1\cos\theta_i} \tag{2.67}$$

Equation 2.62 ($\mathcal{E}_{\perp,r}/\mathcal{E}_{\perp,i}$) turns out similarly. As such, the real parts of both complex quantities are equal, implying that the reflected and incident beams have the same irradiance, resulting in a non-existent transmitted beam i.e. total internal reflection.

Although no average optical power is imparted to the second medium during total internal reflection, in order to satisfy the continuous boundary condition, some transient perturbation of the second medium must exist. This is indeed the case, as an *evanescent wave* is found travelling along from the media boundary with exponentially decaying amplitude. The amplitude decay with distance y into the second medium is given as [8]

$$F(y) = \exp\left[-y\,\frac{2\pi}{\lambda_0}\sqrt{n_1^2\sin^2\theta_i - n_2^2}\right] \tag{2.68}$$

Consequently, d_p can be defined as the *penetration depth* that the evanescent wave penetrates into the second medium i.e. the distance at which $F(d_p) = F(0)\,e^{-1} = 0.37\,F(0)$, as

$$d_p = \frac{\lambda_0}{2\pi\sqrt{n_1^2\sin^2\theta_i - n_2^2}} \tag{2.69}$$

The significance of the evanescent wave is that through interacting with the second medium, information about the second medium can be coupled back into the first.

As light propagates down optical fibres via total internal reflection, an optical fibre can be adapted for sensing applications. Radiation propagating through the fiber may be attenuated by the interaction of the evanescent wave with an absorbing species external to the waveguide. This is known as fibre-optic evanescent wave sensing.

2.3 Infrared Sources

2.3.1 Doped Glass Fluorescence

(a) Introduction to Rare-Earth Ion NIR Fluorescence

Ideally, infrared emission should be spectrally confined to a narrow wavelength band to limit interference from other absorbing substances in a sample. A modulatable IR source is also desirable as this would facilitate signal enhancement techniques such as lock-in amplification (cf. Section 3.4.3). Although NIR lasers and LEDs fulfil these requirements, they do so only at discrete wavelengths dictated by their material bandgap energy, which may be tuned to some degree by doping with silicon, nitrogen, oxygen or zinc e.g. silicon-doped $Ga_xAl_{1-x}As$ LEDs emit in the 879–890nm range.

To provide a more substantial coverage of the NIR region, rare-earth ion fluorescence has been investigated as a NIR spectroscopic source. The rare-earth element are divided between the lanthanides and the actinides, the classifying distinction being the level of population of the $4f$ and $5f$ electron shells. Research into their optical properties has exploded in recent times due to the proliferation of optical communications, especially in erbium NIR fibre amplifiers. Of particular interest are the lanthanide isotopes, as their trivalent ionic states exhibit many useful properties, not least of which is their long-term stability compared to other ionic isotopes.

(i) Absorption

It was found that the trivalent rare-earth ions absorb and emit over narrow visible and NIR ranges. Of the fourteen rare-earth ions, only promethium (Pm^{3+}; radioactively unstable), gadolinium (Gd^{3+}; spin-forbidden transitions) and lutetium (Lu^{3+}; full $4f$ shell) are unsuitable for spectroscopic purposes. In the case of thulium, its trivalent ionic state (Tm^{3+}) exhibits visible absorption at wavelengths accessible with readily available diode lasers such as 670 and 685nm, enabling precisely modulated fluorescence excitation.

(ii) Fluorescence

Photoluminescence occurs when a primary light source induces secondary radiative emission from an irradiated material [8]. The luminescent emission at wavelength λ_0 occurs when electrons, initially excited by absorption of the primary light source to higher energy levels, relax to lower energy levels. Non-radiative relaxation can occur via lattice phonons, but radiative relaxation between two levels E_1 and E_2 ($E_2 > E_1$) generates photons of energy

$$E_2 - E_1 = \frac{hc}{\lambda_0} \tag{2.70}$$

where h is Planck's constant (6.63×10^{-34} Js) and c is the speed of light in a vacuum (2.99×10^8 ms^{-1}).

Fluorescence occurs as a special case of luminescence whereby deactivation of the excitation source also halts the luminescence, which persists for a time equal to the lifetime of the $E_2 \rightarrow E_2$ electron transition. The lifetime τ_{21} can be as low as 10^{-8}s. For the radiative electron transition between the excited energy level $^3F_4$ and the ground level $^3H_6$ of Tm^{3+}, lifetimes of 12ms [9] and 11.51±0.05ms [10] have been reported.

A selection of rare-earth fluorescence from a doped fluorozirconate glass excited by an argon-ion laser is given in Table 2.1 [11].

Element	Wavelength (μm)
Praseodymium	0.908, 1.014, 1.326, 2.300
Neodymium	0.867, 1.048, 1.318, 1.945
Samarium	0.896, 0.936, 1.022, 1.162, 1.376
Dysprosium	0.834, 0.924, 1.000, 1.170, 1.294, 1.384
Holmium	1.015, 1.154, 1.191, 1.381, 1.953, 2.039, 2.848
Erbium	0.847, 0.977, 1.219, 1.538, 2.719
Thulium	1.184, 1.464, 1.847, 2.307

Table 2.1: NIR fluorescence of some trivalent rare-earth ions

(b) Optical Properties of ZBLAN Glass

In this work, Tm^{3+} was embedded in a zirconium fluoride glass host. ZBLAN (ZrF_4-BaF_2-LaF_3-AlF_3-NaF), constructed from the fluorides of zirconium, barium, lanthanum, aluminium and sodium, is one the of the most stable heavy metal fluoride glasses. Intensive research into fluorozirconate glasses has been carried out for fibre optic manufacturing. Although not especially chemically

durable (ZBLAN is susceptible to water) and generally possessing inferior physical attributes to oxide glasses like silica (SiO_2) e.g. thermal expansion (17.2×10^{-6} versus 0.55×10^{-6} for SiO_2) and Knoop hardness (225 kg/mm versus 600 kg/mm SiO_2), due to the multi-phonon absorption cut-off wavelength being shifted further into the IR than with the more commonly used silica hosts, ZBLAN exhibits excellent IR transmittance [12]. In addition, the IR cut-off wavelength can be shifted to longer wavelengths by substituting heavier ions such as Yb or Th for Zr, or by adding heavier halide ions like Br^- or I^-.

The minimum intrinsic optical losses for ZBLAN from Rayleigh scattering and multi-phonon absorption have been calculated as 0.024 dB/km at $\lambda = 2.55\mu$m, eight times less than silica [13]. However, extrinsic losses due to impurity absorption and scattering centres are the the dominant loss mechanisms of ZBLAN fibres. The hydroxyl ion (OH^-) is one of the main contaminants, due to its broad absorption peak at 2.9μm, and transition metal ions are also classed as contaminants; iron (Fe^{2+}) absorbs at 1.14 and 1.85μm, while cobalt (Co^{2+}) absorbs at 2.5μm. Scattering centres can arise during the fibre drawing process by the formation of crystallites. This is due to the drawing temperature being near the crystallization temperature.

The majority of these extrinsic defects can be avoided if a bulk glass sample is used instead of a fibre. As no drawing process is required, crystalline scattering is minimised. Impurity contamination can be avoided by bubbling a reactive gas such as NF_3 through the glass melt to remove impuities. It should be noted that rare-earth ions do not contribute significantly to the overall optical loss as they have relatively sharp absorption bands.

2.3.2 Lasers

The term *laser* is an acronym, representing "Light Amplification by Stimulated Emission of Radiation". Developed in 1960 [14], one of the benefits laser light offers is that only photons of a fixed frequency are generated by the laser, instead of the continuous spectrum provided by incandescent sources, for example. This has proved to be of major use to the spectroscopic community, which has embraced the laser as a spectroscopic source of previously unheard-of spectral purity for absorption spectroscopy. Another benefit is the collimated light output from the laser – instead of radiating in all directions, it confines photons in a tight parallel-sided beam. This allows high optical power densities to be realised with the laser as all the light is restricted to a point.

The process of stimulated emission had been postulated by Einstein as far

back as 1917. As discussed previously, photons of energy ΔE can be generated by the random transition of electrons from one energy level to another "lower" level, separated by ΔE. This process is known as *spontaneous emission*. It can also act in the opposite direction i.e. "upward" electron transitions over ΔE can be triggered by photons of the same energy: *stimulated absorption*. This is represented schematically in Figure 2.5. Figure 2.5(A) illustrates the stimulated

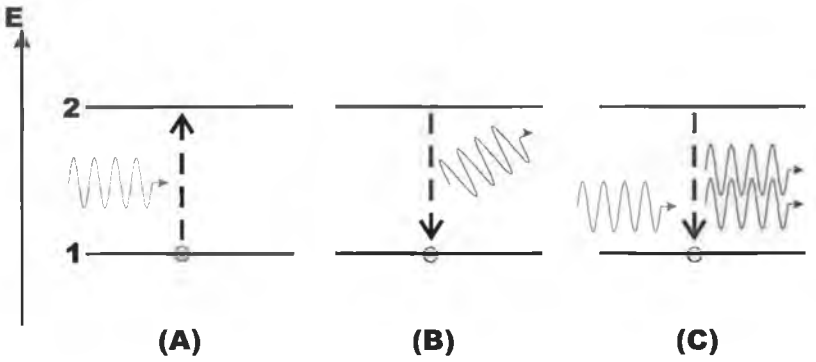

Figure 2.5: Schematic of electron transitions between energy levels *1* and *2* and attendant photon interactions

absorption case, where the energy of a photon is imparted to the electron, enabling a transition from *1* to *2*. In the case of spontaneous emission (Figure 2.5(B)) the electron leaves the upper level randomly, generating a photon. However, as envisaged by Einstein and displayed in Figure 2.5(C), a third situation occurs when an electron undergoes a downward transition triggered by the presence of photons of energy ΔE, releasing another photon of the same energy. This is known as *stimulated emission* and is the cornerstone of laser operation.

The photons generated by stimulated emission have identical properties to those that triggered the electron transition. This leads to a build-up of photons with the same frequency, phase, polarization and direction – an accumulation that can be exploited by passing them back and forth between excited atoms, leading to an overall amplification effect. This is achieved by reflecting the photons though the *gain medium* using mirrors and providing that the gain outweighs any optical losses e.g. non-radiative scattering, then laser action occurs.

A resulting condition for lasing is that the upper energy level must be sufficiently populated that appreciable stimulated emission can occur, a condition known as *population inversion*. The populations of the energy levels of a system in thermal equilibrium can be described by the Boltzmann distribution

$$N_j = \frac{g_j N_0 \exp\left(\frac{-E_j}{kT}\right)}{\sum g_i \exp\left(\frac{-E_i}{kT}\right)} \tag{2.71}$$

where N_j is the population density of energy level E_j, g_j is the degeneracy of the j^{th} level, and N_0 is the total population density. Thus determining the population ratio between two states is accomplished by using Equation (2.71):

$$\frac{N_1}{N_2} = \frac{g_1}{g_2} \exp\left(\frac{E_2 - E_1}{kT}\right) \tag{2.72}$$

or relating $E_2 - E_1$ to the photon energy $h\nu$

$$N_2 = N_1 \frac{g_2}{g_1} \exp\left(-\frac{h\nu}{kT}\right) \tag{2.73}$$

Assuming g_1 and g_2 are constant, it can be seen that for a constant temperature the population of the upper energy level is much less than the lower level. For an energy separation sufficient for visible laser transitions, of the order of an electron-volt ($1\text{eV} = 1.6 \times 10^{-19}$ Joules), the upper level population is negligible and stimulated emission will not occur. To counter this, the upper levels are populated by *pumping* them with enough energy to excite electrons into them, either thermally, electrically, optically or by electron bombardment. This may seem to achieve the population inversion necessary, but as the likelihood of random spontaneous emission is the same as for stimulated emission, the outcome is that both energy levels end up with the same population density.

To circumvent this problem, most lasers are *three-level* or *four-level* systems. They rely on pumping electrons, but not to the top energy level for photon generation: rather, electrons are excited into a level E_2 where they then decay non-radiatively and very rapidly into E_1, a so-called *metastable state* as the electrons reside there for times of the order of milliseconds. It is then from there that the radiative transition happens, either to the ground state E_G in the case of a three-level system, or to another lower energy level E_0 in the case of a four-level system. In the four-level system, an added requirement is that E_0 empties non-radiatively to the ground state faster than the radiative lifetime between E_2 and E_1. Although many lasers exist with different gain media, most can be approximated with the multi-level energy system.

The tightly collimated laser emission is a result of the stimulated emitted photons forming a *standing wave* in the gain medium. Classically, the modes of oscillation permitted in a cavity are given by

$$L = \frac{m\lambda}{2} = \frac{m}{2}\frac{v}{\nu_m} \tag{2.74}$$

where v is the velocity of light in the cavity and ν_m is the frequency of the m^{th} mode. Typically in laser cavities the only modes of oscillation that successfully

achieves gain are those that propagate parallel to the longitudinal axis, thus giving the emitted beam a very small angular divergence. In the case of semiconductor lasers however, their small size means that diffractive effects at the end facets result in large angular divergences, as seen with quantum cascades lasers.

(a) Doped Fibre Lasers

One of the extensions of doped glass fluorescence is the doped fibre laser. Instead of just allowing the NIR fluorescence from electron radiative relaxation to escape from the glass host, by doping an optical fiber and using both the fiber for optical confinement through total internal reflection, and mirrors at the fiber end for forming an optical cavity, enough gain can be attained to achieve lasing action.

(b) Lead Salt Lasers

Lead salt lasers have traditionally been the spectroscopic source of choice for MIR sensing applications due to their tunability and emission wavelengths over the entire MIR region. They are composed primarily of lead selenide (PbSe) but depending on the wavelength region in question, have other components: europium and sulfur for $\lambda < 4\mu$m (PbEuSSe); europium and sometimes tellurium for the $\lambda = 4$–8μm region (PbEuTeSe and PbEuSe); and finally for $\lambda > 8\mu$m, tin in conjunction with tellurium or selenium (PbSnTe and PbSnSe) [15].

Despite their wide coverage of the MIR however, they must be operated at cryogenic tempatures ($\sim 77\,\mathrm{K}$) and this, along with their relatively low power ($< 10^{-6}\,\mathrm{W}$) and frequency instability, results in devices ill-suited for remote sensing applications.

(c) Difference Frequency Generation (DFG) and Optical Parametric Oscillators (OPO)

A technology based on the interaction between two NIR lasers in crystals with quadratic ($\chi^{(2)}$) nonlinearities, OPO and DFG have given rise to broadly tuneable continuous wave (CW) sources for the MIR region.

DFG is based on the combining of two pump beams and provided efficient phase matching exists between the two beams, a third beam is generated which has the sum or difference of the pump frequencies. As we are only interested in MIR wavelengths i.e. low frequencies, it is the difference frequency generated aspect that is important. Conversely, UV lasing is possible with sum frequency generation.

Based on parametric amplification rather than stimulated emission, optical parametric oscillators were first demonstrated in 1965 [16]. An OPO consists of a nonlinear crystal inside an optical resonator, through which a pump beam propagates. The pump beam is converted to a signal beam and an idler beam, either of which can oscillate through the optical resonator and be amplified on passage through the nonlinear crystal, depending on the conditions of the phase matching. Above a threshold intensity, the amplified signal gain overcomes the roundtrip losses and lasing occurs. Both the signal and idler beams are widely tuneable, and provide excellent sources for spectroscopy. An example of this can be found in [17].

Different types of crystal are used and are suitable for for nonlinear frequency conversion in both DFG and OPO configurations. Two of the most commonly used crystals are periodically poled $KTiOPO_4$ (PPKTP) [18] and periodically poled $LiNbO_3$ (PPLN) crystals [19].

(d) Quantum Cascade Lasers

(i) Introduction to the QCL

The invention of the quantum cascade laser was a milestone in semiconductor technology. Perfected in 1994 after over three decades of theoretical refinement and advances in semiconductor processing, it has been hailed as a breakthrough for sensing applications. Unlike most other lasers, the QCL does not rely on electron-hole recombinations between a valence band and conduction band for photonic emissions. Rather, the QCL uses electron transitions within the conduction band: *intersubband transitions*. The device is *unipolar*. As an electron moves from a higher energy state (E_A) to a lower energy state (E_B), a photon is generated, of energy equal to the difference between the electron's two energy states, or

$$\Delta E = E_A - E_B = hf \tag{2.75}$$

where f is the frequency of the emitted photon in Hertz. As no recombination takes place between electrons, after an electron has generated a photon by moving between two energy levels, it is still available to move to another lower energy level (E_C). Through careful engineering of the energy levels, an electron can be recycled through any given number of transitions, thus generating a number of photons equal to the number of transitions. Clearly, this multiplication of the light generated by a single photon gives an enormous boost to the optical power

of the QCL. This was one of the principal reasons why a unipolar laser device was investigated.

The initial idea for the QCL was proposed by Kazarinov and Suris in 1971 [20], and came a decade after the invention of the first semiconductor laser. They proposed that an electron cascading effect could be induced by sequential stages, although early experimental work was hampered by the relative lack of knowledge about electron relaxation. As non-radiative scattering occurred faster than spontaneous emission, it appeared that upper energy levels would depopulate thus not allowing population inversion. In 1994, Jerome Faist, Frederico Ca-

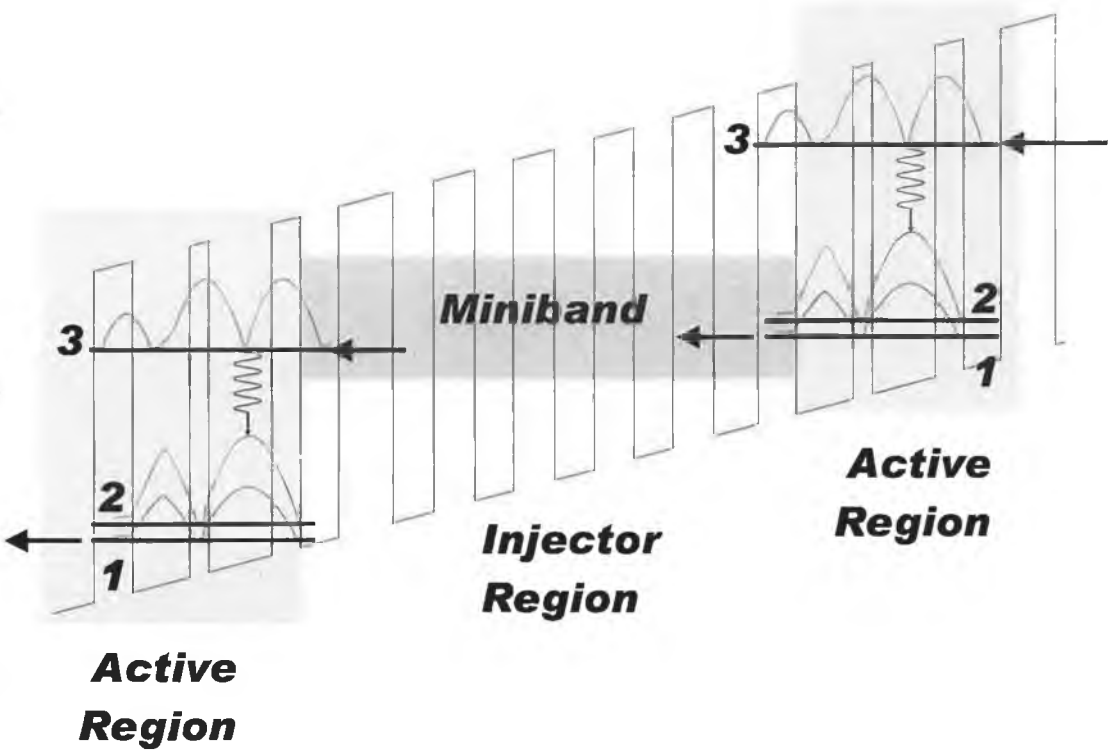

Figure 2.6: Energy level schematic of quantum cascade laser

passo [21] and their group at Lucent Technologies demonstrated the first "QC laser" by exploiting the different non-radiative phonon emission rates between energy levels to achieve population inversion and thus lasing. An explanation of their ground-breaking work is provided in the following section.

(ii) Lasing: Gain versus Loss

Figure 2.6 is a energy level schematic of a typical QCL. Two active regions that house the photon generations between states and a single injector region are shown. The alternating barriers and troughs in the schematic correspond energetically to quantum barriers and wells, that are enabled by engineering the

thicknesses of alternating layers of semiconductor materials e.g. InGaAs and AlInAs on an InP substrate. It has only been in recent years that such fine tuning of semiconductor layer thicknesses on the nanometer (10^{-9}m) scale has become possible, thanks to techniques such as molecular beam epitaxy (MBE). The application of an external electric field is visualised by the slope apparent on the peaks and bases of the barriers and wells. The horizontal bars and curves represent the three most prominent energy levels and modulii squared of the calculated wavefunctions involved in the laser transitions, labelled *1*, *2*, and *3*.

Fundamentally, laser action occurs as follows: electrons tunnel resonantly into the upper energy level *3* from the ground state in the injector region. An electron can then undergo a transition from *3* to *2*, generating a photon of energy equal to the energy difference between the two levels. The electron then non-radiatively transfers (scatters) from *2* to *1*, where ideally it enters the ground state of the following "downstream" injector region. The entire region over which this occurs is known as a *stage*, at it's most basic comprising one injector and one active region.

The hurdle of fast non-radiative transitions by longitudinal optical (LO) phonons was overcome by designing the energy separation of the two lower energy states *1* and *2* as close as possible to the LO phonon modes of the active region materials, while enabling laser action between *3* and *2*. This can be seen by analysing the scattering times for the three levels, defining τ_{32} and τ_{31} as the electron scattering times from *3* to *2* and *1* respectively, and τ_3 as the total upper state lifetime given as

$$\frac{1}{\tau_3} = \frac{1}{\tau_{31}} + \frac{1}{\tau_{32}} \tag{2.76}$$

typically of the order of a few picoseconds (10^{-12}s). As the scattering time between the two lower levels $\tau_{21} = \tau_2$ is usually much lower than the upper scattering time ($\tau_3 \gg \tau_2$), population inversion is achieved between *3* and *2* and laser action is possible. The wavelength of photons generated here is usually of the order of micrometers (μm, 10^{-6}m) i.e. in the infrared spectral region. However, actual lasing can only occur if electrons are delivered by tunnelling into *3* faster than scattering can occur. Conversely, population inversion can only happen if *2*'s electrons empty into *1* and from *1* be injected into the ground state of the downstream injector region faster than scattering from *3*. The external electric field then imparts energy to the electrons, readying them for the next active region.

Not only must a constant environment of population inversion be maintained, but a requirement for laser action is that optical gain must surpass total optical losses. The derivation for the gain coefficient of a structure like that shown in

Figure 2.6 can be calculated [22] as

$$g = \tau_3 \left(1 - \frac{\tau_2}{\tau_{32}}\right) \frac{4\pi e z_{32}^2}{\lambda_0 \varepsilon_0 n_{eff} L_p} \frac{1}{2\gamma_{32}} \tag{2.77}$$

where g is the gain coefficient, e electric charge ($1.6 \times 10^{-19} C$), z_{32} the optical dipole matrix element, λ_0 the wavelength, ε_0 the vacuum dielectric constant, n_{eff} the effective refractive index, L_p the length of one stage (one active and one injector region), and γ_{32} the measured full width at half maximum (FWHM) of the emitted spectrum.

Now the losses must be defined. There are three sources of optical losses [23], although one is entirely avoidable through careful design of the bandgaps. The primary source of losses is outcoupling loss at each end of the waveguide due to the often substantial differing refractive indices of the waveguide ($n_2 = n_{eff} \sim 3.35$) and the external environment (typically air: $n_1 = 1.0$). The oscillating cavity for the laser is simply the end facets of the waveguide, and although they do not form perfect mirrors, the reflectivity R of each end can be defined as

$$R = \left(\frac{n_2 - n_1}{n_2 + n_1}\right)^2 = \left(\frac{n_{eff} - 1}{n_{eff} + 1}\right)^2 \tag{2.78}$$

This results in an outcoupling loss given as

$$\alpha_m = \frac{1}{L} \ln(R) \tag{2.79}$$

where L is the length of the laser resonator cavity. Other losses related to the outcoupling loss include scattering at the facet ends due to surface roughness, but these can prove difficult to exactly define.

The second most serious loss is free-carrier absorption. The injector region is doped to provide the extrinsic electrons necessary for adequate injection into the upper energy level of the active region, and as such these losses α_w can be modelled [24] using a Drude model, giving the approximation $\alpha_w \propto \lambda^2$.

The third most serious source of losses is resonant intersubband transitions, as extrinsic electrons in the injector region can absorb photons if their energy levels are resonant with the optical transitions. However, as mentioned earlier, this can be avoided by careful miniband design.

The threshold current density can now be expressed ignoring any resonant intersubband transition losses as

$$J_{th} = \frac{\alpha_m + \alpha_w}{g\Gamma} \tag{2.80}$$

Γ representing the overlap of the guided mode with the active and injector regions, or the *confinement factor*, thus involving the number of stages present in the

laser. At higher temperatures, a number of changes have to be introduced to Equation 2.80: the electron scattering times of LO phonons are reduced; the gain spectrum is widened due to thermal collisions; and extrinsic electrons can be thermally back excited from the injector to the lower active region, hindering population inversion. Incorporating these temperature effects into the threshold current density offers [25]

$$J_{th} = \frac{1}{\tau_3(T)\left(1-\frac{\tau_2(T)}{\tau_{32}(T)}\right)}\left[\frac{\lambda_0\varepsilon_0 n_{eff} L_p 2\gamma_{32}}{4\pi e z_{32}^2}\cdot\frac{\alpha_m+\alpha_w}{\Gamma}+en_g\exp\left(-\frac{\Delta}{kT}\right)\right] \quad (2.81)$$

where

$$\tau_i(T) = \tau_{i0}\frac{1}{1+\frac{2}{\exp\left(\frac{E_{LO}}{kT}\right)-1}} \qquad i=1,2,3 \quad (2.82)$$

τ_{i0} is the electron scattering time at low temperature, E_{LO} the LO phonon energy, k the Boltzmann constant, T the temperature, n_g the carrier sheet density in the injector ground state, and Δ the energy separation between the injector ground state and the preceding energy level *2*.

The optical power per unit current (also known as the *slope efficiency*, a common rating for comparing semiconductor laser performance) is given as

$$\frac{\partial P}{\partial I} = \frac{1}{2}\frac{h\nu}{e}N_p\left(1-\frac{\tau_2}{\tau_{32}}\right) \quad (2.83)$$

where $h\nu$ is the energy of the photon, and N_p is the number of stages. As can be seen, the slope efficiency is directly proportional to the number of stages, implying that the greater N_p the larger optical power available. This has been verified experimentally as being the case.

(ii) Materials for Mid-Infrared Devices (Intersubband Engineering)

The wavelength of a QCL can be selected by careful design of the thicknesses of the quantum wells (QWs) and barriers. The most popular semiconductor materials used for QCL manufacture can be divided into two broad groups and are based on III-V compound semiconductors: those that use indium gallium arsenide (InGaAs) QWs and aluminium indium arsenide (AlInAs) barriers on a indium phosphide substrate (InP); and those based on gallium arsenide (GaAs) and aluminium gallium arsenide (AlGaAs) using a GaAs substrate. Although GaAs/AlGaAs processing is the more mature technology, difficulties in optical confinement meant that until recently, lasers based on it lagged behind InGaAs/AlInAs devices. Of note is the emergence of antimonide-based (Sb) devices such as InGaAs/AlInSb that can access shorter wavelength ranges ($\lambda \sim 3$–5μm)

by possessing a larger subband energy separation than the other two regimes, but with considerable difficulty in obtaining high quality interfaces between the two semiconductor materials [27] [28].

Most semiconductor lasers rely on the refractive index differences between their constituent materials to ensure optical confinement. This is known as *dielectric waveguiding* and is well suited to the majority of semiconductor devices. By having a large refractive index difference between the active region and the lower-index cladding regions, a situation not unlike total internal reflection confines the radiative emission. In InGaAs/AlInAs devices, the InP substrate ($n \sim 3.10$) and AlInAs ($n \sim 3.20$) are natural cladding layers, with the multilayer active region index calculated by volume fraction of InGaAs ($n \sim 3.49$) and AlInAs, typically giving $n_{active} \sim 3.35$ and thus ensuring optical confinement.

However, in the case of GaAs/AlGaAs devices, the GaAs substrate has a higher refractive index than the core and the AlGaAs cladding. In this case, *plasmon enhanced waveguiding* has been used to maintain optical confinement, and has also been applied to the InGaAs/AlInAs regime for reducing losses [26]. The plasmon enhanced waveguide operates by adapting the surface plasmon wave that normally propagates along the interface between doped regions and metal contacts necessary for current delivery. Normally, free carrier absorption and resonant coupling of the emitted light to the surface plasmon produce detrimental waveguide losses. However, by introducing a highly-doped ($7 \times 10^{18}\text{cm}^{-3}$) layer outside a lower doped ($\sim 10^{17}\text{cm}^{-3}$) cladding layer, the surface plasmon/guided mode resonant coupling is suppressed as the plasmon frequency is tuned to be less than the guided mode frequency. An additional benefit is that the highly-doped region has a much lower refractive index ($n \sim 1.26$), thus improving the confinement.

(iii) Fabry-Perot QCLs

The majority of early QCLs used as-cleaved end facets as reflectors to allow the guided optical emission undergo oscillations in the gain medium, thus forming a Fabry-Perot resonator. This gives rise to a number of guided frequencies as described by the allowed standing wave frequencies of oscillation inside a cavity:

$$p\frac{\lambda}{2} = L \qquad \text{or} \qquad \nu = \frac{pc}{2L} \tag{2.84}$$

where p is an integer and L is the optical path length of the Fabry-Perot cavity (between the two end facets). This gives rise to *axial modes* where discrete laser wavelengths are visible within the gain curve of frequency separation $\delta\nu = c/2L$

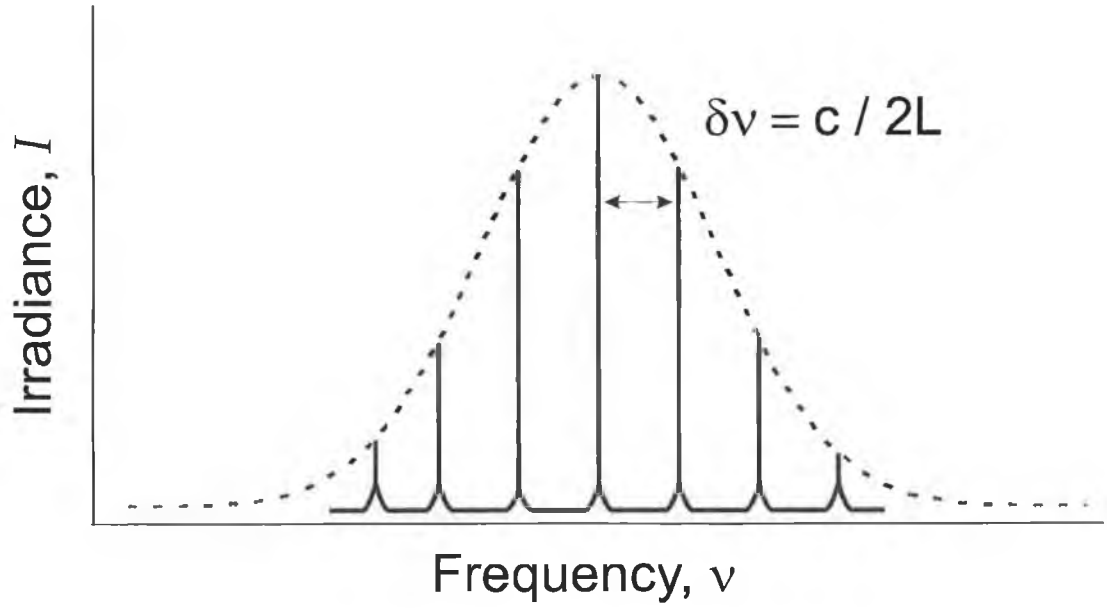

Figure 2.7: Allowed axial laser modes in a Fabry-Perot cavity. The broadened laser transition is overlaid as the dotted line

(Figure 2.7). Accordingly, a range of wavelengths are emitted from a Fabry-Perot QCL. For a typical QCL of 1–3mm long cavity, the spacing of the F-P modes ($\delta\nu \sim 1\text{cm}^{-1}$) is much narrower than the width of the gain spectrum ($> 50\text{cm}^{-1}$). While this leads to a greater than average output power, the ability of the laser to tune to a particular absorption feature in gases is limited.

(iv) Distributed Feedback QCLs

Ideally, a narrow linewidth laser is preferable for gas sensing, in recognition of this, efforts were made to develop a QCL with single mode operation and a good side-mode suppression ratio. The most widespread solution to this task is the *distributed feedback quantum cascade laser* (DFB-QCL), first demonstrated in 1996 [29] [30]. In DFB-QCLs, a Bragg grating is incorporated by wet chemical etching onto either the top surface of the laser, or grown between the active waveguide core and the cladding layer by temporarily removing it from the MBE process [31].

The Bragg grating provides single mode operation by incorporating scattering from the grating back into the waveguide. As the scattering favours one wavelength (the *Bragg wavelength* λ_B) while reflecting all others (Equation (2.85)), only a single mode corresponding to this wavelength is emitted, where $n_{eff}(T)$ is the effective refractive index and Λ is the period of the grating.

$$\lambda_B = 2\, n_{eff}(T)\, \Lambda \tag{2.85}$$

As the refractive index is expressed as a function of temperature T it follows that heating or cooling the laser would lead to a change of the grating period. This would then alter λ_B and also shift the guided laser mode. In this way, the wavelength of the laser can be shifted by *temperature tuning*.

Precisely how the Bragg grating effects the guided optical mode of the QCL is described, for both top-gratings and buried gratings [23]. By etching a metal Bragg grating onto the top surface of the semiconductor waveguide a number of modulations are brought about. Firstly, a loss modulation due to the different losses in the etched grooves and non-etched ridges occurs. The metal grooves pull the guided mode towards it, and the mode takes on some characteristics of a surface plasmon, resulting in a modulation of the effective refractive index and also a generally minor modulation of the modal gain via overlap of the guided mode with the active region (similar to a loss modulation).

The buried grating approach was attempted because only the exponential tail of the waveguide mode interacts with the grating, reducing its efficiency. By incorporating the grating within the laser, a much larger overlap of the guided mode with the grating is achieved, resulting in a larger effective refractive index modulation than seen with top-grating DFB devices [31]. To compare the "strength" of the Bragg gratings, the coupling coefficients for both types were calculated using Equation (2.86) [32] [33]

$$\kappa = \frac{\pi}{2}\frac{\Delta n_{eff}}{\lambda_0} + \frac{i}{4}\left(\Delta\alpha_w\,\omega + \Delta\Gamma\, g_{th}\right) \tag{2.86}$$

where λ_0 is the emission wavelength, g_{th} is the gain coefficient at laser threshold, and the differences in the effective refractive indices, waveguide attenuation coefficients and confinement factors between the grating grooves and ridges are accounted for with Δn_{eff}, $\Delta\alpha_w$, and $\Delta\Gamma$, respectively. For typical top grating DFB-QCLs, $|\kappa| \sim 2$–3cm^{-1} were found [29], and for an improved top-grating design whereby a thin highly doped waveguide layer is etched as the grating, $|\kappa| \geq 15\text{cm}^{-1}$ were calculated [32] [34]. Finally, it was seen that buried grating DFB-QCLs gave the best confinement at $|\kappa| \sim 30$–80cm^{-1} with a side-mode suppression ratio approaching 30dB.

For MIR spectroscopy, lasers using Bragg gratings are certainly adequate sources. Their compact structure, room temperature operation, high optical power of the order of mW per pulse, and the possibility of tuning the wavelength using temperature or a current ramp make them ideally suited to spectroscopic applications.

2.4 Summary

As industrial manufacturing becomes ever more automated, so to must the monitoring and quality control aspects of production become automated. With environmental awareness at an all-time high due to the threat of global warming, the desire for sensors capable of pollution warning and emissions monitoring is greater than ever. In a climate where terrorism is an accepted facet of everyday life, sensors able to detect concealed weapons and warfare agents are urgently required. And in the realms of hard vacuum, the push since the 1990s by NASA for less expensive space probes fitted with off-the-shelf instruments has led to renewed interest in sensor development.

Optical sensing can address each challenge provided by the demanding requirements of these examples. IR sensors can detect an entire array of different chemicals or be tuned to specifically detect a particular molecule or molecular family. Being a non-contact technology means that industrial process line monitoring can be achieved continuously, unlike wholly statistical methods such as batch testing. The vast majority of optical sensors have no moving parts, thus ensuring that maintenance visits to remote environmental sensors are minimised. Non-invasive and multi-analyte sensing capabilities can also be exploited for security applications, at airports for example. Finally, recent work in the field of exogeology, e.g. the Cassini probe orbiting Saturn's largest moon Titan, has been facilitated by IR spectrometers.

The NIR fluorescence of rare-earth doped glass and MIR quantum cascade lasers were selected as the foundation for developing optical sensors for a wide range of applications, from humidity sensing to detecting chemicals known to be present in human breath.

Bibliography

[1] Fraunhofer J. von, *Memoranda of the Royal Bavarian Academy of Sciences* (1817)

[2] Bohr N., *Philosophical Magazine* (1913)

[3] Herschel W., *Phil. Trans. Roy. Soc.(London)* 284 (1800)

[4] Hanna M.W., *Quantum Mechanics in Chemistry (Third Ed.)* (Benjamin/Cummings Publishing Company 1981)

[5] Michelson A.A., *Phil. Mag. (5)* **31** 256 (1891)
Michelson A.A., *Light Waves and Their Uses*, University Chicago Press (1902); reissued 1961

[6] Hvozdara L., Pennington N., Kraft M., Karlowatz M., Mizaikoff B., *Vib. Spec.* **30 (1)** 53–58 (2002)

[7] Hecht E., *Optics (Second Ed.)* (Addison Wesley 1989)

[8] Wilson J. and Hawkes J., *Optoelectronics (Third Ed.)* (Prentice Hall Europe 1998)

[9] Esterowitz L., Allen R., Kintz G., Aggarwal I. and Ginther R.J., *Tech. Dig. Conf. Lasers and Electro-Optics*, Opt. Soc. Amer., paper THH1 (1998)

[10] McAleavey F.J., O'Gorman J., Donegan J.F., MacCraith B.D., Hegarty J. and Mazé G., *IEEE J. Select Top. Quant. Electron.* **3 (4)** 1103–1110 (1997)

[11] McAleavey F., *Development of a Tm^{3+}-doped Fluoride Glass Optical Fibre Laser for Gas Sensing* (M.Sc. Thesis 1995)

[12] Harrington J.A., *Infrared Fibers and Their Applications* 57–82 (Ch. 4) (2004)

[13] Carter S.F., Moore M.W., Szebesta D., Ransom D. and France P.W., *Elect. Lett.* **26** 2115–2117 (1990)

[14] Maiman T.H., *Nature* **187** 493 (1960)

[15] Preier H., *Semicond. Sci. Technol.* **5** S12–S20 (1990)

[16] Giordmaine J.A., *Phys. Rev. Lett.* **14** 973 (1965)

[17] Popp A., *Appl. Phys. B* **75** 751–754 (2002)

[18] Quan W.Z., *Optics Comms.* **252** 179–187 (2005)

[19] Goldberg L., *Opt. Lett.* **20** 1280 (1995)

[20] Kazarinov R., *Fiz. Tekh. Poluprov.* **5** 797–800 (1971)

[21] Faist J., Capasso F., Sivco D.I., Sirtori C., Hutchinson A.L. and Cho A.Y., *Science* **264** 553–556 (1994)

[22] Faist J., *Appl. Phys. Lett.* **68** 3680–3682 (1996)

[23] Gmachl C., *Rep. Prog. Phys.* **64** 1533–1601 (2001)

[24] Yu P.Y. and Cardona M., *Fundamentals of Semiconductors: Physics and Materials Properties* (Springer New York 1999)

[25] Faist J., *IEEE Photon. Technol. Lett.* **10** 1100–1102 (1998)

[26] Sirtori C., *Appl. Phys. Lett.* **66** 3242–3244 (1995)

[27] Georgiew N., *J. Appl. Phys.* **89** 1064 (2001)

[28] Manz C., *J. Crystal Growth* **280** 75–80 (2005)

[29] Faist J., *Appl. Phys. Lett.* **70** 2670–2672 (1997)

[30] Gmachl C., *IEEE Photon. Technol. Lett.* **9** 1090–1092 (1997)

[31] Gmachl C., *Opt. Lett.* **25** 230–232 (2000)
Gmachl C., *Appl. Phys. Lett.* **72** 1430–1432 (1998)

[32] Köhler R., *Appl. Phys. Lett.* **76** 1092–1094 (2000)

[33] Finger N., *IEEE J. Quant. Elec.* **36** 1366–1368 (1998)

[34] Köhler R., *IEEE Photon. Technol. Lett.* **12** 474–476 (2000)

Chapter 3

Experimental System I

3.1 NIR Spectroscopic Humidity Sensor

Trace water sensing is very important in a number of applications. Monitoring of trace humidity levels in microelectronic, pharmaceutical and fibre optic production facilities is critical to prevent impurity contamination. Atmospheric chemistry research also requires reliable humidity sensors [1]. Trace liquid water is a quality control parameter in industries such as agricultural production [2, 3, 4] and paper manufacturing [5], as well as being critical to the clinical assessment of skin and tissue hydration [6].

Many sensors based on a range of sensing principles have been developed attempting to address the needs of industry and medicine. Most commercially available humidity sensors are based on capacitive or resistive changes of polymers or ceramics. Some examples of novel humidity sensing methods include humidity-induced swelling of thin polymeride layers in a piezoresistive device [7], sol-gel/indicator dye matrixes housed on planar waveguides [8], crystalline salts [9], and LED nanoscale interferometric cavities [10], to name but a few.

Near infrared (NIR) spectroscopy is an attractive methodology for detecting water due to its considerable absorption around 1.9μm relative to other chemicals. Although NIR absorptions at overtone and combination frequencies of molecular vibrations are generally weaker than the fundamental vibrational absorptions in the mid infrared (MIR), the absence of other significantly absorbing species in this spectral region makes it well suited for spectroscopic water detection. NIR sensing is also an inherently safe technology, with no contact with the sample required. Rather, the sample can be analysed *in situ* without disturbance provided there is a suitable optical path that the probing radiation can travel from the source, through the sample to the detector.

The availability of inexpensive optical components offers greater flexibility for NIR optical design than for other spectral regions like the MIR, where reflective optics such as mirrors or relatively expensive purpose-built refractive optics are required. Although lenses have been manufactured from materials like calcium fluoride (CaF_2) and sapphire (Al_2O_3), other materials exhibit hygroscopic properties (e.g. potassium bromide (KBr) and salt (NaCl)) and are unsuitable for field deployment.

Humidity sensors based on absorption spectroscopy using NIR tunable diode lasers have been developed. Examples of these include two-tone frequency modulation spectroscopy at $\lambda = 1393$nm [11] and wavelength modulation spectroscopy at $\lambda = 1392.5$nm [12].

NIR liquid water spectroscopy has also been undertaken. The moisture content of paper has been measured using reflectance and multicoloured LED sources [13], and the water content of solvents has been determined with Tm^{3+}:YAG fluorescence [14] and evanescent field sensing using unclad silica optical fibres [15]. Flow injection analysis of water in solvents has been accomplished using NIR [16], as has the *in vivo* analysis of blood flow by sensing the water in blood using liquid crystal tunable filter mounted on an IR-sensitive charged coupled device (CCD) camera [6].

A novel NIR humidity sensor is reported here. It is based on the spectral overlap of the fluorescence of a rare-earth doped IR glass with the NIR absorption spectrum of water. The modulated NIR source, detector and detector electronics are housed in a compact modular device capable of carrying out relative humidity sensing.

3.2 Thulium (Tm^{3+}) in a Fluorozirconate Host

The fluorescence of thulium-doped ZBLAN glass was used as the basis for a NIR water sensor. Although liquid water on surfaces or in solution could also be analysed, relative humidity sensing was chosen as the focus of the sensor development.

Tm^{3+}-doped fluorozirconate optical fibres have been successfully employed as NIR sources into optical sensors, for water spectrometry [17] and in a fibre laser for hydrocarbon gas sensing [18].

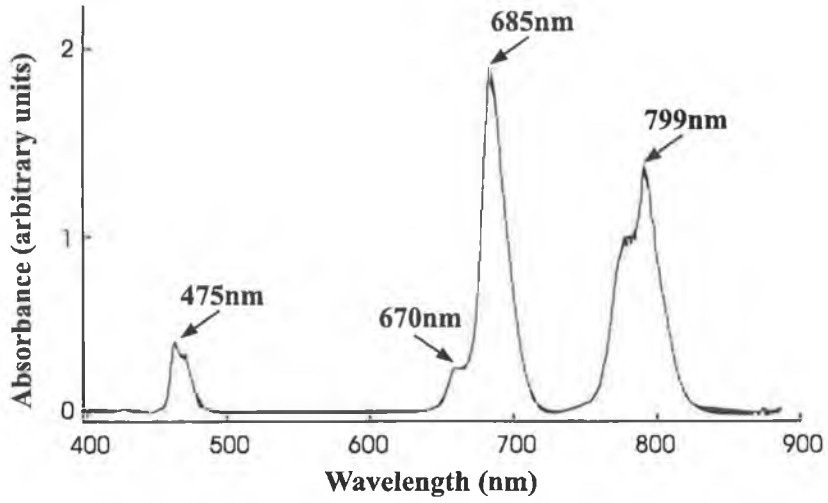

Figure 3.1: Absorption spectrum of Tm^{3+} in ZBLAN glass host, collected with an Ocean Optics spectrometer

3.2.1 Absorption

Figure 3.1 shows the absorption spectrum of ZBLAN glass doped with Tm^{3+} ions collected with an Ocean Optics microspectrometer. The wavelengths labelled correspond to the following electronic transitions, with Tm^{3+}'s ground state denoted as $^3H_6$

$$
\begin{aligned}
^1G_4 \rightarrow {}^3H_6 &\Rightarrow \lambda = 475\text{nm} \\
^3F_2 \rightarrow {}^3H_6 &\Rightarrow \lambda = 670\text{nm} \\
^3F_3 \rightarrow {}^3H_6 &\Rightarrow \lambda = 685\text{nm} \\
^3H_4 \rightarrow {}^3H_6 &\Rightarrow \lambda = 799\text{nm}
\end{aligned}
$$

In order to excite electrons to induce fluorescence, the thulium-glass can be pumped with radiation at the wavelengths mentioned. Although lasers are also commercially available at 670nm and 780nm (sufficient overlap with 799nm absorption), a 685nm laser was the selected pump source due to its relatively large absorbance.

3.2.2 Fluorescence

The fluorescence spectrum (Figure 3.2) of Tm^{3+} in a ZBLAN glass host, excited by a 60mW pulsed laser ($\lambda = 685$nm), was collected with a Control Developments cooled extended InGaAs microspectrometer. The fluorescence centered around 1.83μm is the $^3F_4 \rightarrow {}^3H_6$ electron relaxation of Tm^{3+}. Superimposed on the fluorescence graph is the NIR absorption spectrum of liquid water. Although

the spectral overlap of the fluorescence and absorption is not optimal, there is sufficient overlap that a water sensor could be developed by using the Tm^{3+} fluorescence as a source for absorption spectroscopy.

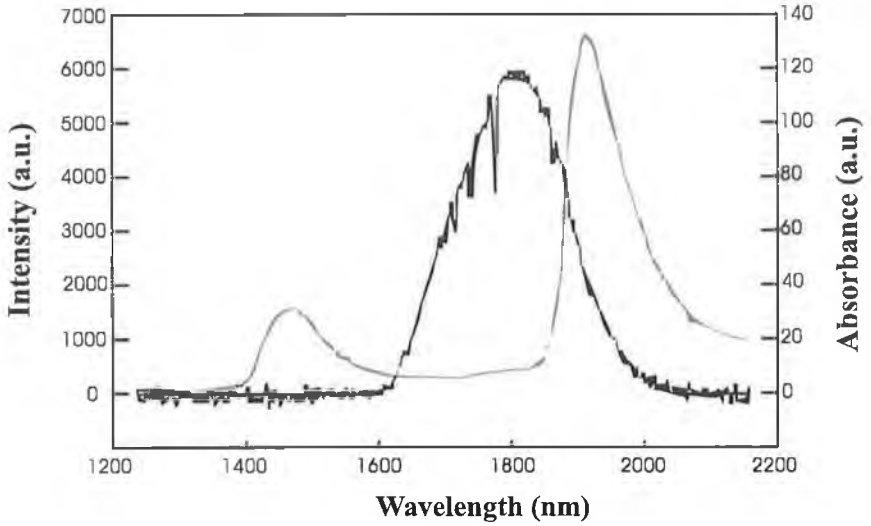

Figure 3.2: Fluorescence spectrum of ZBLAN:Tm^{3+} glass (black line), with the NIR absorption spectrum of water overlaid (grey line)

The dopant concentration of thulium in the ZBLAN glass used was 12%. The reason for this quite high doping level was to maximise the NIR fluorescence from the doped glass. An earlier investigation into how the fluorescence of a doped sample changed as the dopant concentration was varied was carried out with erbium-doped ZBLAN glass. It was found that the fluorescence intensity of the ZBLAN: Er^{3+} increased as the Er^{3+} concentration was increased, up to a certain limit. At this limit, the host glass is dopant-saturated. In order to maximise the ZBLAN:Tm^{3+} fluorescence at 1.83μm, the ZBLAN glass was doped with 12% thulium, at which concentration the host glass was saturated.

3.3 Established Work: Laboratory-Based Prototype

Prior to the work described in this thesis, earlier work had been carried out in the Optical Sensors Laboratory to develop a water sensor using rare-earth doped glass fluorescence. Based on the fluorescence spectra for various rare-earth ions in zirconium fluoride glasses, trivalently ionised thulium (Tm^{3+}) was selected as a source for NIR spectroscopic water detection as the ${}^3F_4 \rightarrow {}^3H_6$ transition spectrally overlaps with the absorption spectrum of water (cf. Figure 3.2). There

are few competing NIR sources that can access this absorption satisfactorily: NIR LEDs are generally cheap but exhibit unstable intensities and are not well matched spectrally to the relevant absorption bands of water. Thermal stabilisation can improve performance in terms of intensity stability, but the available wavelengths are constrained by material bandgap energies. As mentioned earlier, incandescent sources can be fitted with narrow bandpass filters to spectrally overlap with an absorption feature, but are limited by the temperature dependence of the filters and the lifetime of the sources, as well as the ignition risk in flammable environments.

The earlier system, known as the **Laboratory-Based Prototype** (LBP), used the pumping laser as a reference to remove or reduce the effects pump intensity fluctuations would have on the fluorescence. The pump beam and the NIR probe fluorescence were temporally switched such that only one beam was impinging on the detector at any time. This was accomplished using an electronically switchable ferroelectric liquid crystal (LC) waveplate to force the pump beam into a definable polarization. A polarizing beamsplitter (depending on the switching state of the LC waveplate) would then transmit the pump radiation onto the thulium-doped zirconium fluoride glass (ZBLAN:Tm^{3+}) inducing fluorescence, or reflect it off-axially and back to the detector as a reference beam (cf. Figure 3.3). In this way, baseline intensity drift could be referenced out without needing to use two separate detectors, which could potentially have different detection characteristics and thus require an extra level of signal processing to correctly reference intensity instability.

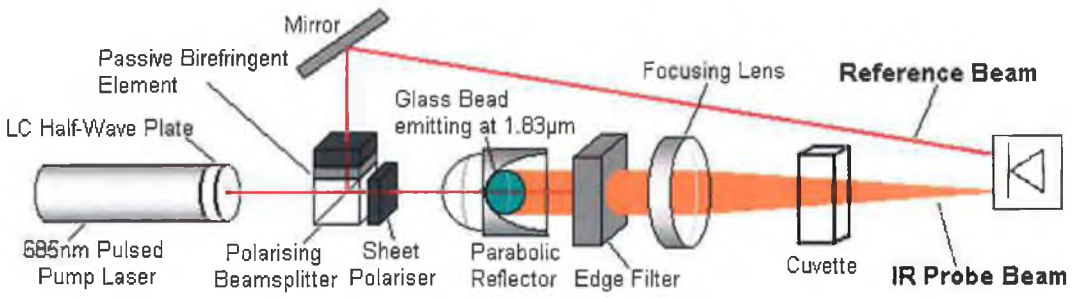

Figure 3.3: Laboratory-Based Prototype of ZBLAN:Tm^{3+} fluorescence-based water sensor

A pulsed diode laser emitting at 685nm was chosen as the pump source, and an irregularly shaped (non-optically optimised) segment of a ZBLAN:Tm^{3+} glass cube was used as the fluorescent source. The ZBLAN:Tm^{3+} glass cube was manufactured by Le Verre Fluoré in France.

The fluorescence was modulated at the same frequency as the pump laser

modulation. This allowed *lock-in amplification* to be used, a method whereby the signal from the detector is amplified only if it has the same frequency as a reference frequency. In this instance, if the pump laser frequency is used as the lock-in amplifier reference frequency, the detector signal (in response to the modulated NIR fluorescence radiation) will be amplified as it too will be modulated at the same frequency. As such, small signal changes caused by NIR absorption can be isolated from background thermal noise and amplified to a useful magnitude.

The Laboratory-Based Prototype sensor was demonstrated in a number of configurations, including liquid water sensing in a transmission cuvette, water vapour (relative humidity, RH) sensing in a 10cm-long gas cell, and surface drying in diffuse reflectance mode. Although flexible enough to be an effective water sensor in all of the above mentioned configurations, the stability of the sensor was not optimal even considering pump referencing. In addition, the switchable polarisation added a considerable element of complexity to the system, as well as directing the reference beam away from the optical interrogation path, such that any instability not due to absorption e.g. scattering could not be "referenced out". Finally, the irregular shape of the ZBLAN:Tm^{3+} resulted in a non-uniform fluorescence emission envelope, making collimation and focusing difficult.

3.4 The Industrial Prototype

The author's involvement with this work commenced with developing the next iteration of the LBP. It was decided that a full-scale refinement of the Laboratory-Based Prototype be instigated to remove the complex optical switching and simplify the optical configuration, to enclose the sensor in a modular housing with removable heads for sensing water in both fluidic phases and on surfaces, and to improve sensor stability. To this end, a suitable optical configuration was modelled using ray-tracing programs and this became the basis of the **Industrial Prototype**.

3.4.1 Optical Design

The first design decision taken was that while the reference beam generation using the switchable LC waveplate and polarising beamsplitter was novel and technologically impressive, it did not lend well to industrial or remote environments. In such embodiments, fundamental system simplicity is paramount to avoid production downtime in the case of an industrial process monitor, or over-regular maintenance visits for a remotely-sited environmental sensor, for example. To

this end, a more rugged optical design was implemented, whereby the sensor would not only house the pump and fluorescence optics, but would also feature sufficient electronic processing and detection capabilities that would minimise the number of external devices.

The Industrial Prototype retained the modulatable fluorescence from the previous iteration of the sensor, but the temporal switching was abandoned in favour of a configuration where the pumping laser would still be used as a reference beam, this time following the same optical path as the IR probe beam. The pumping laser used was a 685nm modulatable laser diode (Laser 2000 UK; **Appendix A**).

The fluorescence source was replaced with a 5mm diameter spherical ZBLAN glass bead, doped with 12% Tm^{3+} and placed within a 19mm-wide parabolic reflector (Carley Lamps; ref. 1936), quasi-collimating the fluorescent emission from the bead. The bead was deemed to be optically optimized compared to the irregularly shaped glass used in the LPB *viz.* a uniform fluorescence was produced. Not all of the pump radiation is absorbed for fluorescence excitation, and it was this unabsorbed component of the laser diode emission that would be used as the reference signal.

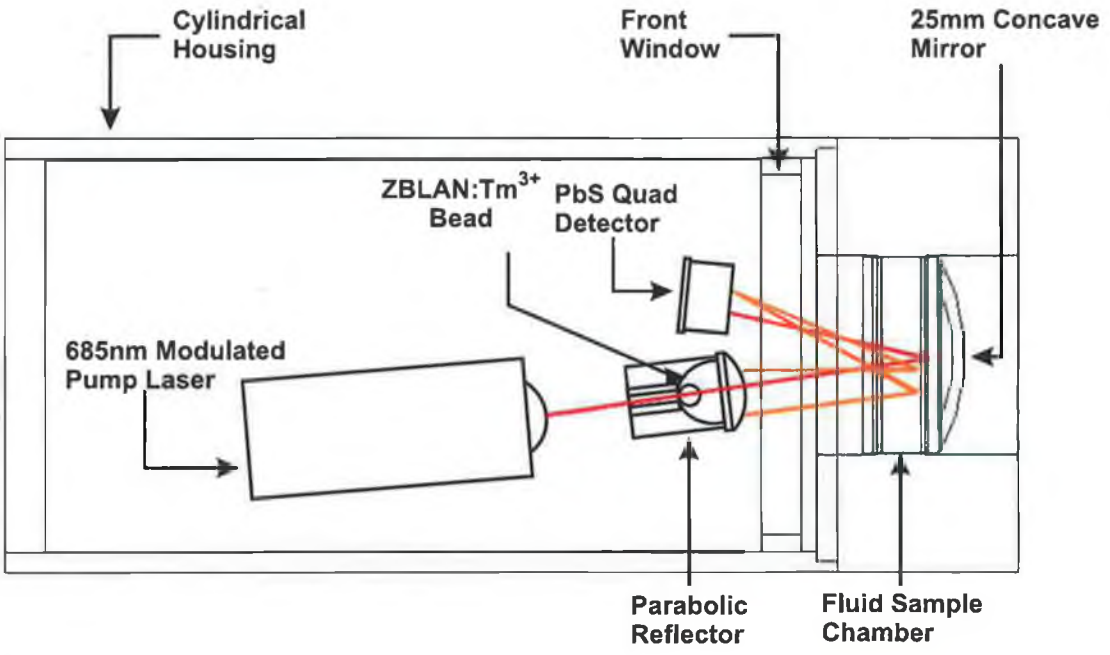

Figure 3.4: Optical configuration of the Industrial Prototype

Figures 3.4 and 3.5 are a schematic and CAD image of the optical configuration used to achieve co-axial fluorescence and referencing. The upper side of the platform served as an optical bench, where the pump laser diode, ZBLAN:Tm^{3+} bead and parabolic reflector, and a suitable NIR detector were arranged in a re-

flective configuration. The underside of the platform served as a mount for signal filter

Figure 3.5: 3D view of prototype with outer housing, optical platform and liquid head. The electronics are situated on the bottom of the platform

The pump diode laser was focused using a 10mm focal length plano-convex lens attached to the laser diode aperture, and optically coupled to the ZBLAN:Tm^{3+} bead through the rear of the parabolic reflector. The doped bead was epoxied onto a small aluminium cylindrical stub which fitted into the back of the reflector, through which pump radiation could impinge on the ZBLAN:Tm^{3+} bead via a 2mm diameter opening in the back of the stub. The fluorescence was quasi-collimated by the reflector and focused using a 20mm focal length plano-convex lens placed at the mouth of the parabolic reflector.

The stub-bead combination was situated within the parabolic reflector to position the bead at the focus of the reflector. The laser diode-lens combination was positioned at a precise distance from the reflector-stub-bead combination. This linear combination of the source optics was situated on the platform close to the front window of the housing, such that a parallel beam emitted from the reflector was incident at 5° to the central axis of the platform. The detector was situated at 5° from the central axis on the side opposite the source optics. The reference beam followed the same path as the probe beam.

Moisture bearing samples were interrogated by reflection through a fluid chamber: a 10mm gap in the case of liquids and a 50mm cavity in the case of gases. Two interchangeable heads were constructed to facilitate measurement in each of these cases. Behind the fluid chamber in each case a concave mirror was fitted to the back of the chamber to aid in refocusing the IR radiation back into the detector. The Liquid Cell employed a 25mm focal length mirror while the Gas Flow Cell employed a 50mm focal length mirror.

3.4.2 NIR Detectors

There are two general categories that IR detectors can be divided into: photoconductive devices and photodiodes. Photoconductive detectors, also known as photoresistors, rely on resistance change caused by incident radiation which is expressed as a change in the potential difference across the detector if it is part of a potential divider. Free electrons are created by photons which are absorbed by the active region material (e.g. silicon, metallic sulphide). If an electrical potential is applied across the detector, current can flow. As the availability of free electrons changes in direct proportion to the incident radiation intensity, the observed shift in detector resistance can be related to the intensity. Typically photoconductive detectors are inexpensive devices and are excellent choices for low-frequency applications.

By generating an electrical output from photon absorption, photodiode detectors do not require a bias voltage to operate. Instead of using resistance change to detect light, photodiodes are based on photon absorption in a semiconductor p-n junction. Operating in *photovoltaic* mode i.e. measuring the potential between the p and n regions, increased sensitivity is afforded by the absence of dark current [19].

(i) Project Requirements

The NIR fluorescence emission at 1.83μm was modulated at the same frequency as the 685nm pump diode laser; this frequency was provided by a benchtop pulse generator. At sub-kilohertz modulation frequencies, photoconductive detectors have sufficiently fast response to adequately capture the modulated NIR signal and were used for the humidity sensor.

Two types of photoconductive detectors were used with the project, both supplied by Cal Sensors (Santa Rosa, CA, USA). The most widely recognised "figure of merit" for detectors is the *specific detectivity*, D^* (pronounced "D-star"), and is defined as

$$D^* = \frac{\sqrt{A_d \cdot \Delta f}}{NEP} \tag{3.1}$$

where A_d is the active area of the detector's sensing element and Δf is the bandwidth. NEP, the Noise Equivalent Power, is the incident radiative power required to produce a signal-to-noise ratio (SNR) of 1. D^* has the units $\mathrm{cm}\sqrt{\mathrm{Hz}}\,\mathrm{W}^{-1}$.

One of the main sources of electronic signal instability in IR detectors is thermal noise. Background radiation can contribute to the overall IR signal, and as placing filter upon filter in the detector's field of view (FOV) to remove

the background components would be costly both in terms of time and expense, an alternative method must be used to eliminate thermal noise. By cooling the detectors and keeping them at a fixed low temperature, thermal noise can be minimised. Cooling is usually accomplished by cryogenic or electronic means: the former is commonplace for MIR detectors where liquid nitrogen (LN_2) is used to maintain temperatures around 77K (-196°C). Fortunately for NIR detectors, electronic cooling using Peltier coolers is often sufficient. These devices exploit the Peltier effect to provide cooling on one side of a plate and heating on the other side. With proper heat sinking to draw off excess heat, Peltier coolers can maintain the temperature of a detector down to -30°C in a compact T-08 package indefinitely.

(ii) Lead Selenide (PbSe) Detector

The first detector used in this work to sense NIR water absorption was a lead selenide (PbSe) detector. Although this detector is designed to give optimum responsivity at higher wavelengths (cf. Figure 3.6), its sensitivity was deemed suitable for the first iteration of the sensor i.e. the Laboratory-Based Prototype.

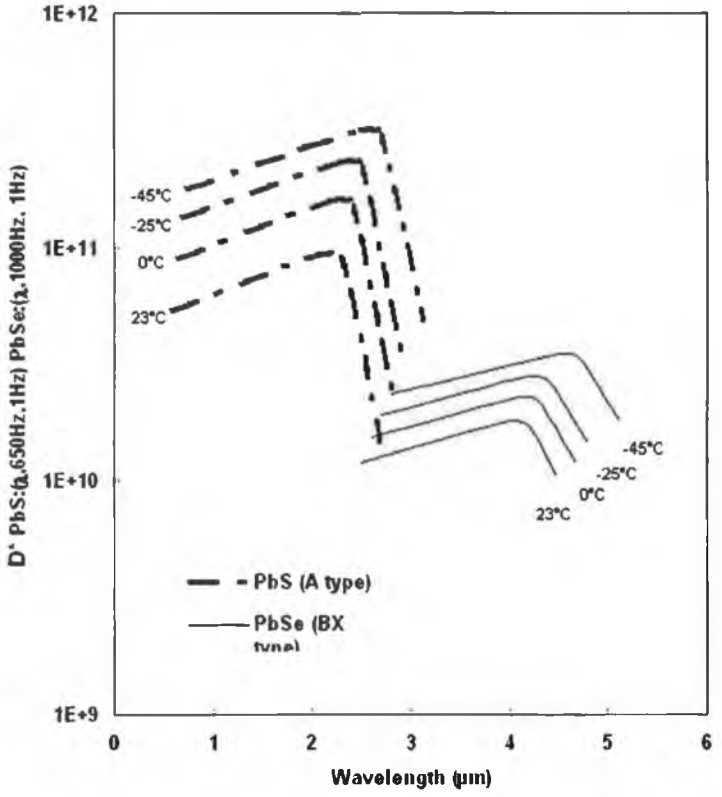

Figure 3.6: Graph displaying the typical spectral response of PbS and PbSe detectors

As both the NIR probe fluorescence ($\lambda = 1.83\mu$m) and the pump beam ($\lambda =$

685nm) were being temporally switched to allow referencing, as well as modulated at a kHz-level frequency to allow lock-in detection, only one detector was required to detect both pump and probe beams. This common detector approach avoided detector mismatch that using dual detectors could have posed due to sensing material inconsistencies.

(iii) Lead Sulphide (PbS) Quad Detector

For the Industrial Prototype, an improvement in the detection sensitivity was required to detect smaller relative humidity shifts. The original PbSe detector was replaced with a lead sulphide (PbS) quad detector (Cal Sensors; ref. AT1S-18T(M)-4; **Appendix B**). It not only exhibited better D* than the PbSe (an entire order of magnitude), but had four sensing elements, each with an independent output channel. Each element could accommodate optical filters within the detector package: IR-transparent anti-reflection coated silicon (LWP-1000, percentage transmittance $> 90\%$ in the range 1.80–2.60μm, zero transmittance at wavelengths below 1.0μm) was installed over two detecting elements, while IR-opaque KG-3 glass (percentage transmittance of 60% at 685nm, $< 1\%$ at 1.85μm) was installed over the other two elements. The filters ensured that the NIR probe beam could be sensed without interference from the visible reference beam, and vice versa, using the single detector package. Although all four elements were provided with filters, two elements were sufficient for probe and reference beam detection. As the PbS quad detector elements were manufactured from the same die, the effect of detector drift was minimised. D* for the two detector facets was specified for a facet active area of 0.01cm^2 and a noise bandpass of 7.85Hz as 3.16×10^{11} and 3.09×10^{11} cm$\sqrt{\text{Hz}}\,\text{W}^{-1}$for the IR and visible detecting element, respectively.

3.4.3 Detection Electronics

It was necessary to replace the circuitry that had been used previously with the Laboratory-Based Prototype. This is because instead of both signals (probe and reference) being carried from the detector on a single channel, there were now two channels being used. A two-channel detector circuit was built incorporating a multiplexer (National Semiconductor; ref. CD4053BC) that enabled switching between both detector channels (Figure 3.7). The single output from the multiplexer was amplified using an OP77 operational amplifier and fed to a benchtop lock-in amplifier (EG&G Princeton Applied Research Model 5101). The amplified

signal was then sampled by a data acquisition PC card (National Instruments; ref. PCI-6024-E) and analysed using LabVIEW Virtual Instrument software.

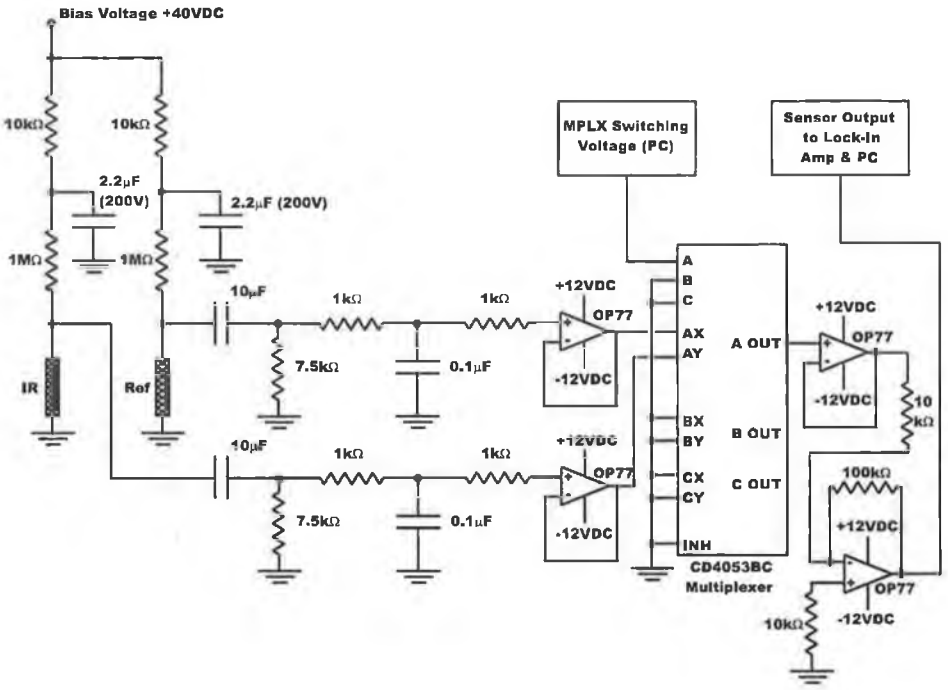

Figure 3.7: Circuit diagram for detecting photoresistive changes using multiplexed signal switching

A number of power supplies were required for operating the various electronic components of the Industrial Prototype. Integration of these device inputs was carried out on the same circuit board as the detector bias circuitry. Although the 685nm pump diode laser was operated in pulsed mode, a DC voltage was also required for operation. The laser had two independent inputs, one of which was connected to a Bang & Olufson SN16A DC supply, the other to a pulse generator (Levell Function Generator; ref. Type TG303) for TTL pulses (0–5V). Another B&O DC supply was required for operating the Peltier cooler in the PbS quad detector, while an additional supply was used to provide bias voltage for the two quad detector photoconductive elements. Finally, the multiplexer required a external modulated power supply to facilitate switching between the probe and reference signals. While a pulse generator was initially used, a LabVIEW virtual instrument (VI) was implemented that provided the necessary modulated signal (cf. Section 3.4.4).

(i) Lock-In Amplification

Lock-in amplification is an invaluable tool for signal analysis. Based on the principle of frequency-selective amplification, useful data embedded in noisy signals

can be successfully retrieved. Although improvements to SNRs can be accomplished by lengthening the sampling time to average out random noise, this may not be feasible if signal shifts occur over timescales shorter than the increased sampling time.

Lock-in amplifiers work around this by sampling a modulated signal of known modulation frequency and only amplifying that signal, thus reducing noise. Initially, a detector signal (S_0) in response to a modulated optical signal is amplified and passed through a filter tuned to the reference frequency i.e. the known modulation frequency ω. The signal after amplification S is

$$S = S_0 A \cos(\omega t) \tag{3.2}$$

where A is the amplification factor. The reference signal undergoes a phase shift and is recombined with the amplified signal, resulting in

$$S' = S_0 A \cos(\omega t) \cos(\omega t + \gamma) \tag{3.3}$$

As $2 \cos A \cos B = \cos(A + B) + \cos(A - B)$, this becomes

$$S' = \frac{S_0 A}{2} [\cos(2\omega t + \gamma) + \cos \gamma] \tag{3.4}$$

and so a value is reached that represents the amplitude of the detector signal ($\frac{S_0 A}{2} \cos \gamma$) and has an additional high frequency component ($\frac{S_0 A}{2} \cos(2\omega t \gamma)$). By simply passing S' through a low-pass filter, the DC amplified signal can be retrieved while the time-varying component is suppressed.

3.4.4 Data Acquisition

In order to read in, store and display the NIR spectroscopic absorption data, a personal computer was fitted with a data acquisition (DAQ) card (National Instruments; ref. PCI-6024-E). The DAQ card allowed the PC to sample and process analog signals via a desktop input/output (I/O) connector board.

The LabVIEW software suite was used to process and display data. Based on Virtual Instruments (VIs), programs can be written to acquire and analyse data while offering numerous visualisation options. A graphical user interface (the Front Panel) was designed to facilitate more user-friendly operation of the completed program.

A VI was created to sample the DC output from the lock-in amplifier, while another was written to collate the samples and average them over a set time period. By sampling the multiplexer switching control and comparing it to a

set voltage value, LabVIEW was capable of determining whether the amplified detector signal being read at a particular moment was due to the NIR probe beam or the visible reference beam. This was circumvented by writing a VI that provided the multiplexer with a modulated signal, thus determining absolutely the switching times between both probe and reference signals.

3.4.5 Optimisation of Industrial Prototype

(i) Electronic optimisation

The beam switching requirement led to issues with the electronic circuitry designed to process the detector output. Very long rise-times, of the order of 1s, were observed from the lock-in amplifier for multiplexing switching frequencies of 0.4Hz. This led to inordinately slow sensor response times to water content in samples, a feature that a NIR optical sensor should not exhibit.

It was found that this extremely lengthy rise-time was due to the lock-in amplifier's Pre-Filter time-constant setting. An additional lock-in amplifier was procured to process the reference signal, bypassing the multiplexer (Figure 3.8). By maintaining uniform settings on both lock-in amplifiers (amplification, time constant, and phase shift control), any inconsistencies in mutual drift were minimised.

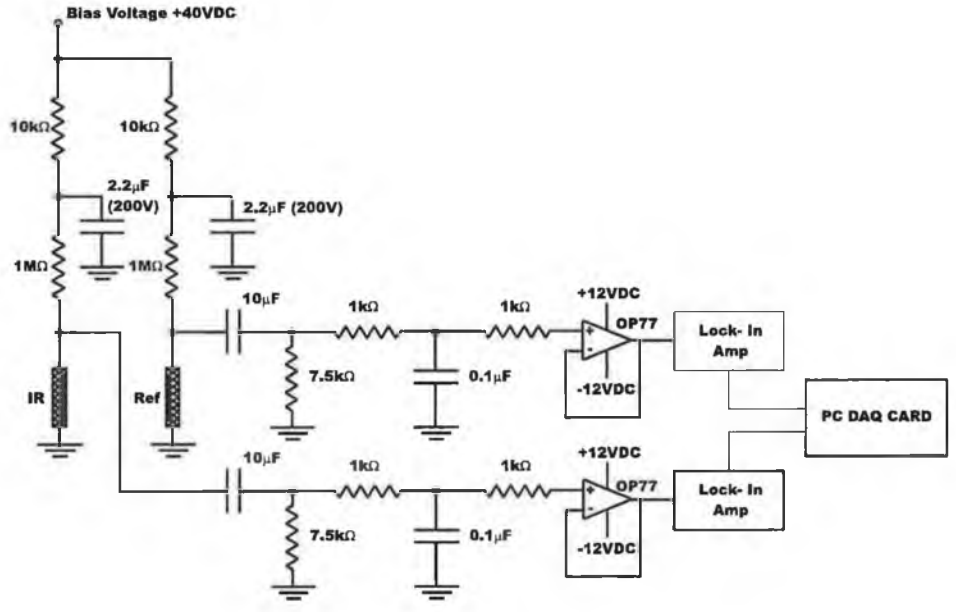

Figure 3.8: Circuit diagram for detecting photoresistive changes using dual lock-in amplification

(ii) Optical optimisation

The provision of a moveable stub onto which the ZBLAN:Tm^{3+} bead was attached allowed for optimal positioning of the bead within the parabolic reflector. In this way, and together with the focusing lens on the pump laser diode, the maximum amount of pump radiation could be directed onto the ZBLAN:Tm^{3+} bead, while optimising the collimated output from the reflector.

(iii) Detector temperature monitoring

The PbS quad detector is equipped with an integrated thermistor that was used to monitor the detector temperature. The resistance of the sensing elements is inversely proportional to temperature (1.31MΩ for $T = 25°C$; 3.95MΩ for $T = -20°C$ for one sensing element). As the optical signal was detected by placing the quad detector in a potential divider arrangement, any temperature shift of the detector affected signal repeatability. Therefore, the ability to sense any temperature fluctuations was critical for determining true detector response to IR absorption. A resistance R_{TH} versus temperature T_{TH} profile was supplied by Cal Sensors for the in-built thermsitor, and a best-fit curve was fitted. A first order exponential curve was found to be the best approximation to the curve:

$$R_{TH} = ae^{-b(T_{TH})} \tag{3.5}$$

Thus, any change in temperature-induced resistance shift can be accounted for and monitored. Using the best fit coefficients ($a = 3.0861$, $b = 0.0049$) and using a potential divider circuit to detect resistance change, a VI was written and integrated into the LabVIEW data processing program that concurrently monitored the detector temperature and displayed the temperature graphically. This allowed thermal sensor drift to be accounted for.

The feasibility of using the pump beam

(iv) Relative humidity generation

A system was built that generated repeatable relative humidity (RH) levels over lengthy periods of time. The apparatus and experimental set-up used to characterise the response of the sensor when measuring the presence of water vapour in nitrogen is shown in Figure 3.9.

The presence of water vapour in gas was measured through the use of a flow cell, to which nitrogen with a known moisture content and at room temperature was introduced and referenced against dry nitrogen. A mass flow controller (MFC

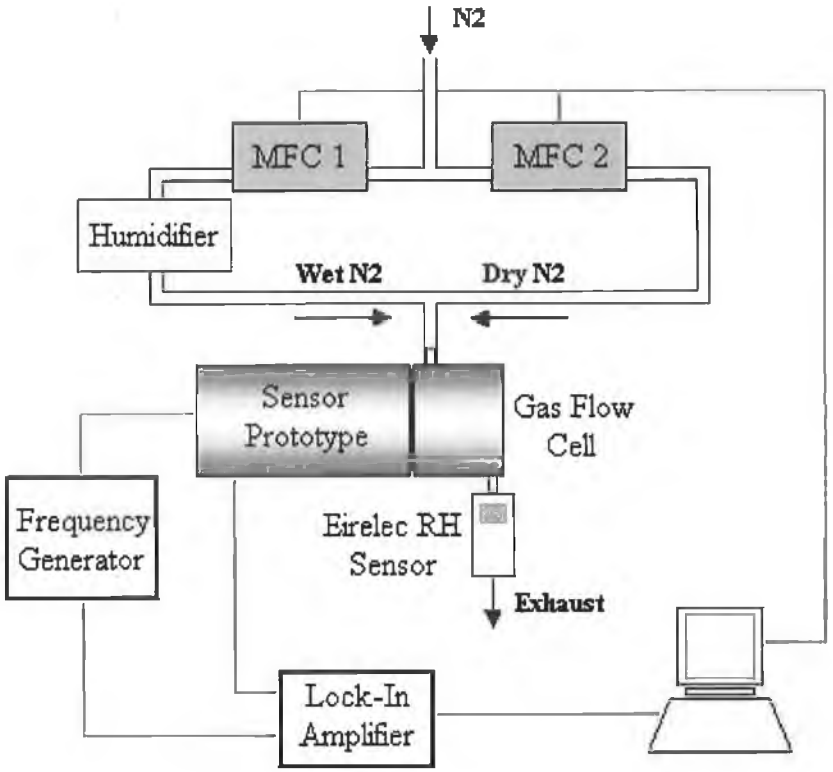

Figure 3.9: Experimental setup used to generate fixed RH levels for calibration of the industrial prototype

1) allowed nitrogen (water content <5ppm) to be fed into a humidifer, while another mass flow controller (MFC 2) facilitated mixing of fixed amounts of the humidified nitrogen (Wet N_2) and the dry nitrogen (Dry N_2). The moisture content inside the Gas Flow Cell was therefore strictly controlled.

The MFCs were controlled using a benchtop controller. To accurately calibrate the RH levels within the Gas Flow Cell, an Eirelec TH21 capacitive RH sensor was connected to the exhaust outlet of the cell. It was found that the mixing system required approximately two minutes to purge the cell of its previous contents and fill it with a N_2 mixture of fixed RH.

3.5 Summary

The development of a humidity sensor based on rare-earth doped glass fluorescence has been detailed here, along with descriptions of detection electronics and signal processing techniques.

The primary aim was to develop a rugged modulatable sensor that could detect humidity changes. Such a device would be well suited to applications such as leak monitoring within gas pipelines, and the flexibility afforded by the

reflective source/detector configuration meant that other applications could be investigated e.g. liquid water sensing in solvent manufacture using the Liquid Cell, or water content in paper manufacture via diffuse surface reflectance of the probe and reference beams.

Optimisation of various characteristics of the sensor was carried out in parallel with ongoing stability and calibration studies (cf. Chapter 5)

A photograph of the finalised version of the sensor can be seen in Figure 3.10.

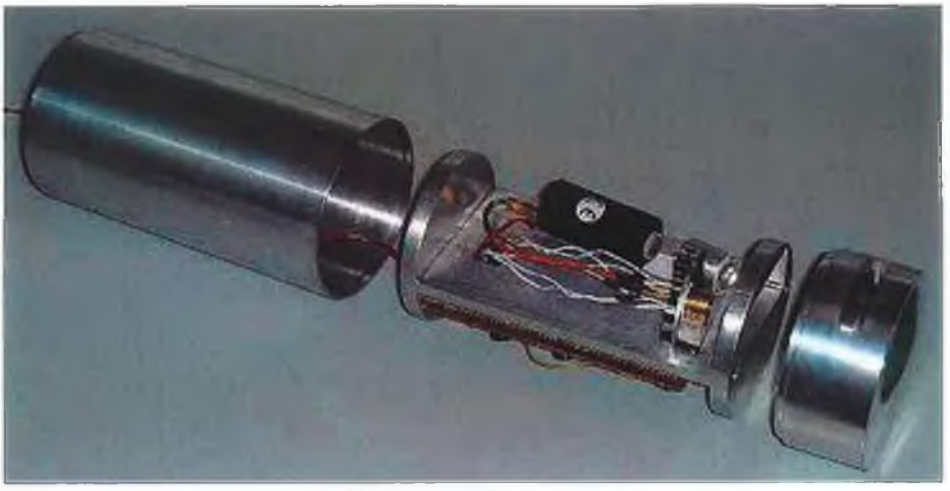

Figure 3.10: Photograph of the Industrial Prototype, showing the cover, the optical platform and electronics, and the liquid sensing head

Bibliography

[1] Sempreviva A.M. and Gryning S.E., *Boundary-Layer Met.* **77 (3–4)** 331–352 (1996)

[2] Delwiche S.R., Pitt R.E. and Norris K.H., *Cereal Chem.* **69 (1)** 107–109 (1992)

[3] Delwiche S.R. and Hareland G.A., *Cereal Chem.* **81 (5)** 643–649 (2004)

[4] Hop E., Luinge H.J. and Van Hemert H., *Appl. Spec.* **47 (8)** 1180–1182 (1993)

[5] Balls B.W. and Boersma J., *Paper Technol. and Indust.* **14 (6)** 331–338 (1973)

[6] Attas M., Hewko M., Payette J., Posthumus T., Sowa M. and Mantsch, H., *Skin Res. and Technol.* **7 (4)** 238–245 (2001)

[7] Buchhold R., Nakladal A., Gerlach G. and Neumann P., *Sensors and Actuators B* **53 (1–2)** 1–7 (1998)

[8] Skrdla P.J., Saavedra S.S., Armstrong N.R., Mendes S.B. and Peyghambarian N., *Anal. Chem.* **71 (7)** 1332–1337 (1999)

[9] Evju J.K. and Mann, K.R., *Chem. Mat.* **11 (6)** 1425–1433 (1999)

[10] Arregui F.J., Liu Y.J., Matias I.R. and Claus R.O., *Sensors and Actuators B* **59 (1)** 54–59 (1999)

[11] Edwards C.E., Barwood G.P., Gill P., Schirmer B., Venzke H. and Melling A., *Appl. Opt.* **38 (21)** 4699–4704 (1999)

[12] Hovde D.C., Hodges J.T., Scace G.E. and Silver J.A., *Appl. Opt.* **40 (6)** 829–839 (2001)

[13] McClure W.F., Moody D., Stanfield D.L. and Kinoshita O., *Appl. Spec.* **56 (6)** 720–724 (2002)

[14] Yokota M. and Yoshino T., *Meas. Sci. Technol.* 11 152–156 (2000)

[15] Lennie A.R. and Kvasnik F., *Anal. Chim. Acta* **281** 265–270 (1993)

[16] Garrigues S., Gallignani M. and de la Guardia, M., *Anal. Chim. Acta* **281** 259–264 (1993)

[17] McAleavey F.J. and MacCraith B.D., *Elec. Lett.* **31 (16)** 1379–1380 (1995)

[18] McAleavey F.J., O'Gorman J., Donegan J.F., MacCraith B.D., Hegarty J. and Mazé G., *IEEE J. Select Top. Quant. Electron.* **3 (4)** 1103–1110 (1997)

[19] Wilson J. and Hawkes J., *Optoelectronics (Third Ed.)* (Prentice Hall Europe 1998), Chapter 7 332–334

Chapter 4

Experimental System II

4.1 MIR Spectroscopy using Quantum Cascade Lasers

Quantum cascade lasers provide unprecedented access to the MIR spectral region. Being unipolar solid state devices, they offer high optical power in a compact package. Only invented in the early 1990s, early research focused on improving the room-temperature pulsed wave (PW) lasers currently available. Although room temperature continuous wave (CW) QCLs are not yet commercially available, research is continuing into raising their operating temperatures from the cryogenic range by changing the laser semiconductor material or improving heat dissipation via buried heterostructure gain regions [1, 2].

QCLs have had a tremendous impact on infrared sensing and telecommunication applications are also being pursued. QCLs can be modulated at terahertz frequencies due to their picosecond-scale electron lifetimes [3], allowing high speed optical communications [4]. The MIR emission can be tuned to avoid atmospheric absorptions (such as water and CO_2), enabling free-space signal transmission [5]. However, it is as MIR spectroscopic sources that QCLs have been most successful.

The potential of QCLs as MIR spectroscopic sources has been widely recognised early in their development [6, 7, 8, 9, 10]. Most molecules exhibit strong absorptions due to fundamental vibrations in the mid infrared. MIR absorption spectroscopy has become a powerful analytical tool by exploiting these fundamental absorptions. FTIR spectroscopy is widely used to analyse samples over a large spectrum e.g. 2–16μm (625–5000cm^{-1}) but it is not generally suited to field deployment due to size and system complexity.

A spectroscopic method that has become popular and more applicable to compact optical sensing is laser absorption spectroscopy (cf. Section 2.2.2). Lead

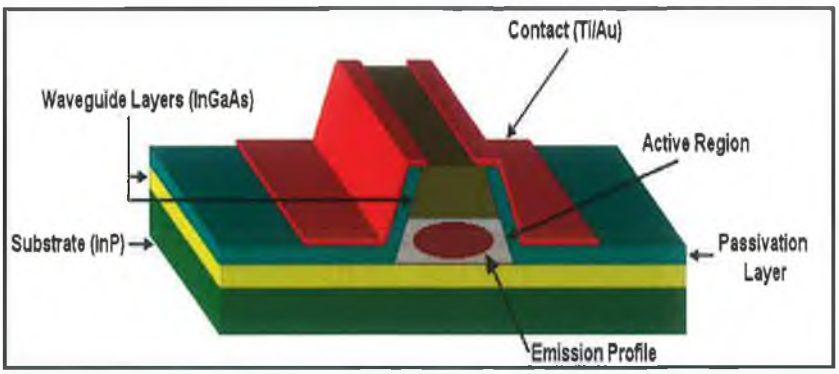

Figure 4.1: Schematic of a typical Fabry-Perot QCL

salt tunable diode lasers (TDLs) are a standard method of accessing the MIR but suffer from the requirement of cryogenic cooling. QCLs can operate at room temperature or with thermoelectric cooling, and can exhibit stable single mode operation.

QCLs have been used in a broad range of spectroscopic sensing configurations. A considerable number of sensors employing QCLs as spectroscopic sources have been demonstrated recently in fields as diverse as the motor and medical device manufacturing industries.

In terms of emission analysis, QCL based spectrometers have been used for vehicle emission certification [11], industrial exhaust system [12] and biomass steam gasification monitoring [13], microgravity droplet ignition analysis [14], and even cigarette smoke analysis [15].

Atmospheric gas sensing has also been accomplished with QCLs. Atmospheric gases that have been detected include atmospheric nitric oxide (NO) [16], carbon monoxide (CO) [17], nitrous oxide (N_2O) and methane (NH_3) [18], and ozone [19, 20]. The CO_2 content of the Martian atmosphere has also been analysed with a QCL spectrometer [21].

Aqueous sensing poses particular difficulties for MIR spectroscopic analysis due to the strong spectral interference of matrix components in aqueous mixtures. In the case of FTIR spectroscopy, optical path lengths are typically 10–50μm long, which leads to reduced sensitivity and a danger of cell clogging in the case of particle-containing samples [22]. However, analysing aqueous samples with QCLs allows for longer optical path lengths of around the order of 125μm [23] due to their considerable optical power, which in turn increases sensitivity. Chemicals detected in aqueous solutions interrogated by QCLs include phosphate (PO_4^{3-}) in Diet Coke samples [22]; glucose and fructose in red wine [23]; adenine and xanthosine [24]; dissolved CO_2 [25]; and adenosine, guanosine, xanthosine and

adenosine-5'-monophosphate (AMP) using capillary electrophoresis to separate the sample [26].

Portable breath analysis is a technology that has benefitted from the proliferation of the QCL as a discrete MIR source. Healthy human breath can contain several hundred components at picomolar concentrations (10^{-12}M) [27] besides the bulk matrix of N_2, O_2, CO_2, water and inert gases. These trace gases include inorganic gases like NO and CO, and volatile organic compounds (VOC). Deviations from normal endogenous concentration levels can be linked with particular physiological processes. It was found that a number of chemicals correlate with particular metabolic and pathologic processes; such chemicals are known as *biomarkers* [28, 29, 30, 31].

Some examples of biomarkers are given in Table 4.1 ([29, 31] and references therein). Where two biomarkers are given for a particular process (like ethane and pentane), they both contribute to the endogenous breath concentration.

As can be seen from Table 4.1, biomarkers have great potential for non-invasive medical diagnosis compared to current diagnostic methods like biopsies. However, no clinical uptake of breath analysis has occurred due to a lack of accepted standards for breath sampling procedures and data interpretation, a shortfall in mapping exhalation kinetics, and no standardised and definitive understanding of the physiological meaning of all biomarkers [31].

Therefore, the qualification and quantification of endogenous biomarkers and potential interferences is vitally important. Examples of interferences include exogenous contaminants e.g. increased hydrocarbon breath content in smokers, breath acetone changes caused by dieting or fasting, changes in exhaled ammonia during graded exercise [32], or the circadian rhythm and age dependency of breath isoprene concentrations.

Attempts to establish correlations between biomarker concentration in breath and blood have been undertaken, using a variety of detection methods. Breath ammonia concentrations of end-stage renal failure patients have been found to vary with blood urea N_2 and creatine concentrations during haemodialysis procedures [33]. Volatile fatty acids, including acetic acid, in the breath of patients with liver cirrhosis has been observed [34]. Gas chromatography (GC) has been employed in determining volatile carbonyl compounds such as formaldehyde in tumour-infected patients [35], while gas chromatography-mass spectrometry (GCMS) has afforded a substantial investigation into lung cancer-related biomarkers, including alkanes and alkane and benzene derivatives [36]. Two critically important biomarkers are acetone (C_3H_6O) and formaldehyde (CH_2O).

Chemical Group	Biomarker(s)	Phys. Process / Condition
Saturated Hydrocarbons	Pentane	Acute cardiac allograft rejection, breast cancer, alcoholic liver disease
	Ethane and pentane	Lipid peroxidation, oxidative damage, mental or physical stress, asthma, apnea, ARDS
	Butane and propane	Protein oxidation, fecal flora
Unsaturated Hydrocarbons	Isoprene	Oxidative damage, cholesterol synthesis, bacterial origin
O_2-containing Compounds	Acetone	Uncontrolled diabetes mellitus, fasting, dextrose metabolism, lipolysis
	2-propanol	Acetone reduction byproduct
	Ethanol	Intestinal bacterial flora
	Acetaldehyde	Endogenous ethanol oxidation
	Methanol	Intestinal bacterial flora
Sulphuric Compounds	Carbon disulfide	Methionine metabolism, lung transplant rejection, schizophrenia
	Ethyl mercaptane, dimethyl sulfide, dimethyldisulfide,	Liver cirrhosis, liver transplants
N_2-containing Compounds	Nitric oxide	Asthma
	Ammonia	Impaired liver function, uremia
	Di- and trimethylamine	Uremia
C-containing Compounds	Carbon monoxide	Haemolysis
	$^{13}CO_2$ or $^{14}CO_2$	*H. pylori* infection

Table 4.1: Endogenous biomarkers and associated physiological processes

Breath acetone has been intensively investigated due to its potential as an early warning for diabetes onset. World Health Organisation figures estimate that 1 in 20 deaths worldwide are attributable to diabetes, emphasising the need for a straightforward and reliable breath acetone analyser. Formaldehyde is another physiologically important chemical. Well established as a urine or *in vitro*

biomarker for bladder, prostate and breast cancer [37, 38, 39, 40], elevated levels have been observed in the breath of nasal tumour-bearing mice and humans [35].

4.1.1 QCL Biosensing

QCLs have been successfully demonstrated in medical applications e.g. sensing glucose in *in vivo* skin samples [41] and in serum [42]. QCL based breath sensors have much to offer breath analysis. The narrow linewidth and high optical power of QCLs facilitate excellent molecular selectivity for distinguishing similar biomarkers, while bypassing technical hurdles such as substance separation.

Several biomarkers have been sensed using QCLs e.g. CO in vascular cell structures [43]; carbonyl sulfide (COS) [44]; nitric oxide (NO) [45, 46]; ethylene (C_2H_4) [47, 48]; and ammonia (NH_3) [49, 50, 51]. A CW QCL has been used to detect methane (CH_4) and nitrous oxide (N_2O) [52]. Other MIR sensors that have been used to analyse biomarkers include DFG spectroscopy of endogenous CO [53] and antimonide CW diode laser spectroscopy of methane [54].

Due to the very small biomarker concentrations found in breath, sometimes preconcentration steps are taken to increase analyte concentration and enhance sensitivity. Methods such as polymer coatings on optical fibres and ATR crystals for aqueous VOC sensing [55, 56], hydrophobic porous sol-gel films [57], silica gels for aldehydes [58], and plasma polymerised adsorbent films for airborne chemicals [59] are examples of preconcentration treatments that have increased the sample concentration.

4.2 Driver Electronics for Laser Operation

A QCL development system was purchased from Alpes Lasers to develop a platform for MIR sensing. This comprised the following components to generate and supply conditioned current pulses to the QCL, as well as provide temperature control for wavelength stability:

- TPG128 pulse generator for generating voltage pulse trains with independently variable period (0.2–105μs) and pulse width (1–200ns)
- LDD100 current switcher for combining the nanosecond pulses with a constant DC voltage supply
- LLH Laboratory Laser Housing for mounting the QCL, fitted with a Peltier cooler for temperature control

- TC-51 temperature controller for controlling the temperature of the laser via the Peltier cooler, critical for maintaining wavelength stability
- LDD supply cable for connecting the TPG128 pulse generator, a DC power supply, and the LDD100 current switcher
- Low impedance stripeline for supply current pulses to the laser housing
- Cable for connecting TC-51 temperature controller to laser housing

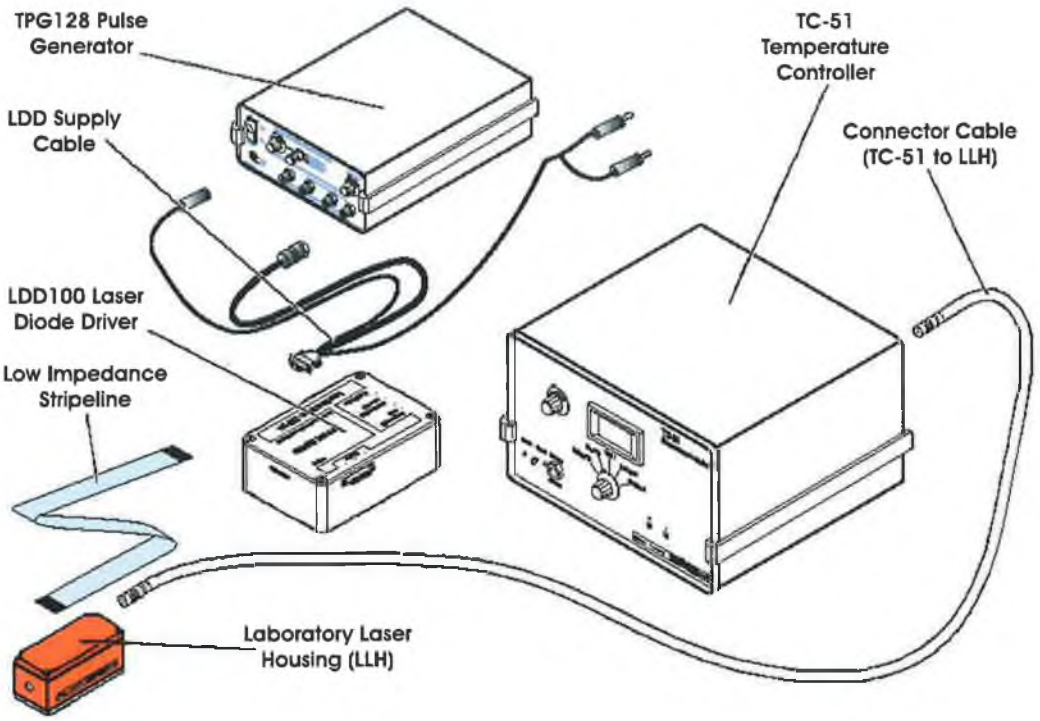

Figure 4.2: The QCL driver electronics (*image courtesy Alpes Lasers*)

4.3 Optical Configuration for Multiple Analyte Sensing

A number of different optical configurations were tested with the quantum cascade laser. The objective was to develop a generic sensing platform with which a number of chemicals could be analysed, depending on their MIR absorbance.

Two QCLs were used in the research. The first was a distributed feedback device (DFB-QCL) emitting at 6.0μm (1667cm^{-1}) with an average optical power of 7mW. At this wavelength, water and propylene exhibit significant absorption.

A Fabry-Perot laser (FP-QCL), emitting at 5.625μm (1778cm^{-1}) with an average optical power of 20mW, was used for interrogating the absorption bands of gaseous acetone, formaldehyde and liquid acetic acid. The QCLs and the chemicals that they analysed, along with the relevant fundamental molecular vibration and centre frequency are summarised in Table 4.2.

Laser	Chemical	Vibration	Frequency (cm^{-1})
QCL 1	Water (H_2O)	ν_2 bend	1595
(DFB)	Propylene (C_3H_6)	ν_6 C=C stretch	1653
QCL 2	Acetone (C_3H_6O)	ν_3 C=O stretch	1731
(FP)	Acetic acid ($C_2H_4O_2$)	ν_4 C=O stretch	1788
	Formaldehyde (CH_2O)	ν_2 C=O stretch	1746

Table 4.2: List of chemicals analysed with available QCLs

4.4 Collimating and Focusing Optics

Although optical materials and components are routinely available for the NIR spectral region, this is not the case for the MIR region. Production costs for optics like lenses are currently far greater than for NIR optics, due to a historical lack of demand from industry and research. Although high power optics around 10.6μm are available for CO_2 lasers due to their use in industry, other parts of the MIR region have not been as well serviced. Another perceived obstacle was the significant water absorption band between 3 and 5μm, which stifled the production of MIR optics as many manufacturers believed the effort to be redundant in the face of zero demand.

With the arrival of the QCL, and other advances in MIR source engineering, the dearth of MIR materials is slowly being turned around. However, still-significant production costs and a view that MIR optics are still specialist items has kept their cost high.

What follows is a summary of available options for collecting and guiding the highly divergent QCL emission, as well as comments pertaining to certain difficulties integrating each option into the sensing system. One of the most serious issues was the divergent profile of the laser emission, characteristic of diode lasers due to their small facet sizes. Divergence values for a 10.6μm DFB-QCL have been reported as 18° horizontally and 61° vertically [48]. The non-uniform spatial distribution is due to the rectangular cross-section of the laser facet. For

Alpes Lasers QCLs, the far field elliptical profiles were quoted as being $60° \times 20°$ from a facet 5 to 30μm wide and 4μm high. As a consequence, optics with low focal lengths (so-called "fast optics") were required so as to capture most of the diverging beam.

- **Calcium Fluoride (CaF_2) Double Convex Lenses**
  Supplied by Edmund Optics, these optics have the advantage of being simple to set up and high MIR transmittance (96%), but suffer a number of disadvantages: expensive (€685/unit), a clear aperture of only 80% of lens diameter, surface reflectance losses, and depending on the focal length, either fail to gather the wide angle divergence or produce an elliptical beam.

- **Off-Axis Parabolic Mirrors (OAPMs)**
  Both Edmund Optics and Janos Technology supply parabolic aluminium-coated or gold-coated mirrors in a range of off-axis angles (30°, 60°, and 90°) and mirror diameters. Being less expensive and more robust than lenses, and exhibiting excellent reflectance with either coating ($\sim$ 98%), they offer an excellent alternative to convex lenses. However like lenses, some of the vertically divergent part of the QCL beam is lost due to the OAPM's having a minimum *effective focal length* (*EFL*) of 25.4mm or more.

- **Calcium Fluoride (CaF_2) Ball Lenses**
  Ball lenses are most commonly used to focus narrow collimated beams into optical fibers. The effective focal length and *numerical aperture* (*NA*) of a ball lens are dependent on the lens' refractive index n and its diameter D (Equations 4.1, 4.2).

$$EFL = \frac{nD}{4(n-1)} \tag{4.1}$$

$$NA = \frac{2d(n-1)}{nD} \tag{4.2}$$

  where d is the collimated emerging beam diameter. Assuming the widest aspect of the QCL spatial distribution (the major axis of the elliptical divergence: 60°) corresponds to a numerical aperture, then the NA of a suitable ball lens is required to be at least $\sin 30° = 0.5$. The maximum collimated emerging beam width d is limited by the diameter of the ball lens D i.e. $d \leq D$. As $NA = d/(2EFL)$, for an NA of 0.5 the effective focal length equals the beam diameter e.g. for a CaF_2 ball lens of diameter $D = 8$mm, one would get an *EFL* of 7mm, a beam diameter of only 7mm and a beam

cross-sectional area of 38.5mm^2 (compare with the area of a 1 inch diameter window of 506.7mm^2).

Medway Optics supply CaF_2 ball lenses, but required custom manufacture. In addition, the extremely small *back focal length* (*BFL*; $\sim$ 3mm) of the lens makes coupling to the laser practically impossible, as the edge of the QCL facet was 7mm inside the Laboratory Laser Housing supplied by Alpes Lasers.

- **Calcium Fluoride (CaF_2) Cylindrical Lenses**
  Cylindrical lenses focus along one optical axis only, so theoretically two such lenses in series would perfectly collimate the elliptical QCL beam. However, getting two lenses manufactured in a MIR-transmitting material, and the requirement for generating a collimated beam from two cylindrical lenses

$$\frac{z_2}{z_1} = \frac{\tan\phi_1}{\tan\phi_2} \tag{4.3}$$

  where $z_{1,2}$ are the individual back focal lengths of the two cylindrical lenses and $\phi_{1,2}$ are the half-angles of the divergence, made using cylindrical lenses too costly a proposition.

In the end, it was decided that the off-axis parabolic mirrors (OAPMs) supplied by Janos Technology offered the best performance-to-cost ratio of the available options. Assuming a Lorentzian divergence [48] of $60° \times 20°$ and rotating the mirror such that its longitudinal axis was perpendicular to the wider divergence, all of the narrower divergent beam aspect was collected and only 3.92mm of the wider aspect "spilled" over the mirror edge. Therefore only a small fraction of the vertical divergence was not collected.

4.5 Open Path Cell and Waveguide Configurations

A number of optical configurations for absorption spectroscopy were built. The $\lambda = 6.0\mu$m DFB-QCL was integrated into an optical configuration shown schematically in Figure 4.3.

Initially, a fibre optic evanescent wave spectroscopic (FEWS) experiment was constructed to detect water concentrations in water-methanol solutions. Silver halide fibres were used to evanescently probe the aqueous solutions. A similar configuration was used for sensing gaseous propylene in air using a silica hollow waveguide (HWG).

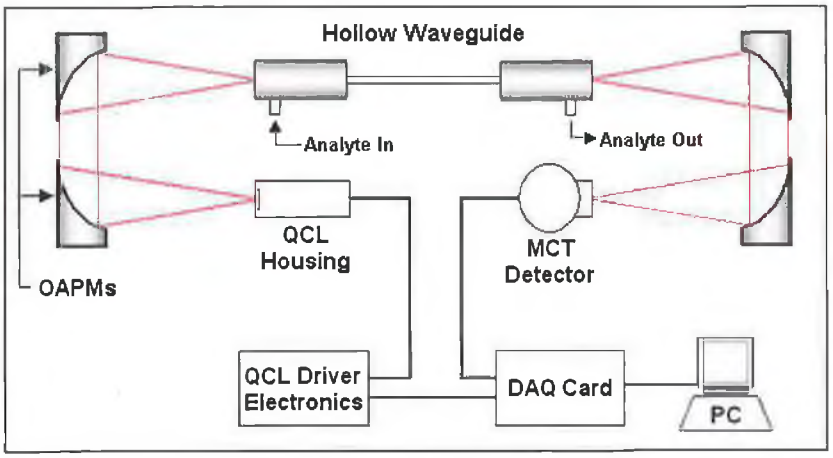

Figure 4.3: Optical configuration for coupling QCL to waveguides such as optical fibres or hollow waveguides; OAPM: off-axis parabolic mirror

The $\lambda = 5.625\mu$m FP-QCL was implemented in an open path optical architecture (Figure 4.4) but was also coupled into a hollow waveguide for improved optical path length. Aqueous solutions of acetic acid and ethanol, mixtures of gaseous acetone and nitrogen, and formaldehyde in nitrogen, were analysed using open paths cells (further described in Section 4.5.2). A hollow waveguide was used to increase the sensitivity of the gaseous acetone sensing by increasing the optical path length over which the gas mixture was probed.

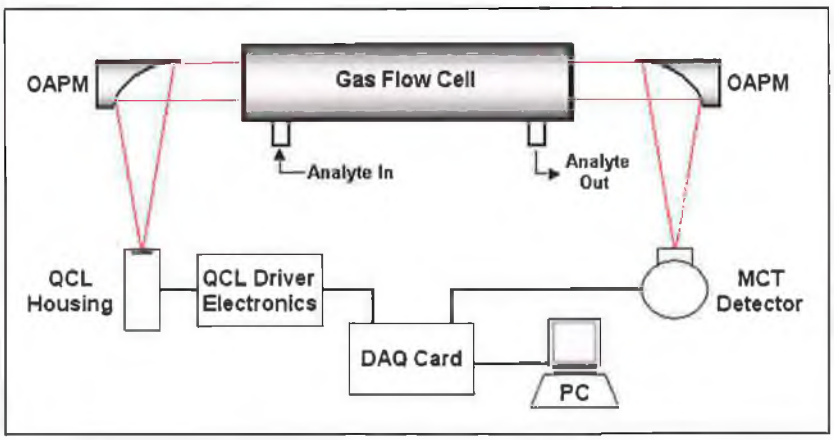

Figure 4.4: Optical configuration for open path gas interrogation. A similar configuration was used for open path liquid analysis

The experimental setup shown schematically in Figure 4.4 was used for development of a pulse amplitude referencing system (Section 4.7.1).

4.5.1 Silver Halide (AgX) Optical Fibres

Polycrystalline optical fibres are commonly used for MIR waveguiding, either for sensing applications or CO_2 laser beam delivery for industrial and medical purposes [60]. The most common polycrystalline formulations include silver halide ($AgCl_xBr_{1-x}$ or simply AgX) and KRS-5 (TlBrI). Although most metal-halide crystals have excellent IR transmission, only the silver, thalium and a few alkali halides have the necessary physical properties to be successfully produced as optical fibres [61].

Other fibre materials suitable for MIR transmission include single crystals like sapphire (Al_2O_3) and chalcogenide glasses such as As_2S_3 and AsGeTeSe. However, AgX fibres have a number of properties that make them best suited for MIR sensing applications.

Transmission losses for the best reported AgX fibres range from $3.4 dBm^{-1}$ at $4\mu m$ down to $0.3 dBm^{-1}$ at $10\mu m$ [62]. KRS-5 fibres exhibit similar transmission behaviour, but research has been discontinued due to the toxicity of thallium salts [63, 64].

Even without fibre cladding, AgX fibres have excellent optical confinement due to their high refractive indices, which depends on the ratio of AgCl to AgBr comprising the fibre and can vary between 1.98 (pure AgCl) and 2.25 (pure AgBr) [65].

Bare AgX fibre was chosen for carrying out FEWS experiments on water and methanol mixtures. Silver halide fibres are non-toxic and unlike KRS-5 or alkali halides are insoluble in water. A length of unclad $AgCl_{0.40}Br_{0.60}$ fibre ($n_{MIR} = 2.08$–2.12; bulk absorption 0.9–$1.2 \times 10^{-4}\,cm^{-1}$ [66]) of diameter $700\mu m$ was placed within a 15.12cm liquid flow cell with a Teflon septum and screw-on plastic cap at each end to ensure sealing (Figure 4.5). The fibre and flow cell were placed between the laser focusing optics and the detector collection optics as shown in Figure 4.3. QCL radiation was coupled into the ends of the fibre via fibre micropositioners and two off-axis parabolic mirrors (OAPMs), and an identical optical arrangement was used to gather and focus light exiting the fibre. Water and methanol mixtures were sequentially injected into the flow cell and the water content was interrogated by the evanescent field penetrating from the fibre into the mixture. The IR attenuation was monitored using a suitable detector (cf. Section 4.6).

(i) AgX Fibre Handling Issues

One of the primary disadvantages of AgX fibres is their ductility which can lead to plastic deformation if mishandled. It was found that a 50/50 mix of AgBr

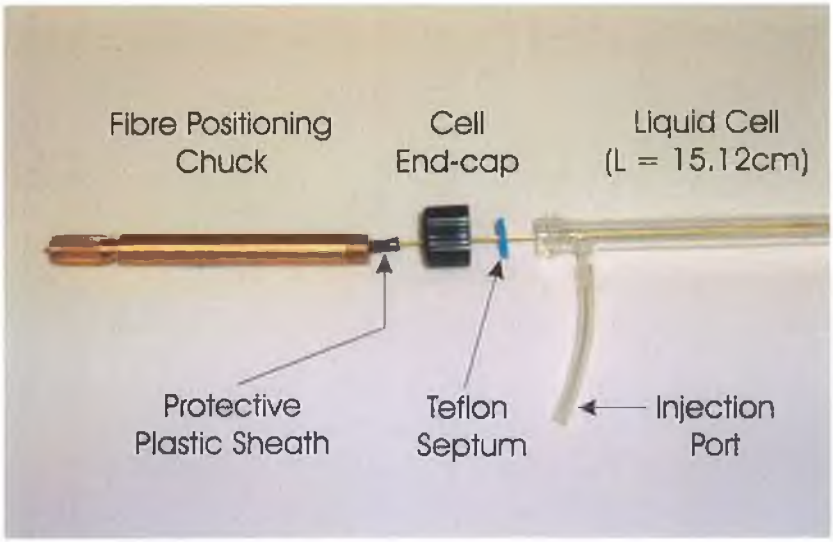

Figure 4.5: Close-up view of a fibre end and mounting

and AgCl gave the best tensile strength (before breaking) of around 90MPa and maximum elastic strain limit before material degradation [67]. In contrast to glass fibers, the optical attenuation of AgX fibres can be drastically affected by bending or cyclic flexure, potentially leading to a greater than 20% drop in transmittance [68].

Another concern when dealing with AgX fibres is aging, whereby the fibre optical loss increases over a period of months, even in storage [69]. An increase in attenuation has been reported for $AgCl_{0.25}Br_{0.75}$ in the spectral range 3–13μm over twelve months e.g. from 1.7 to 6.0dBm^{-1} at 4.0μm [70]. The attenuation change is attributed to increased scattering losses caused by microvoid buildup at grain boundaries, increasing grain size and the formation of large impurity centres [61]. Changing the fibre composition to $AgCl_{0.5}Br_{0.5}$ or $AgCl_{0.75}Br_{0.25}$ has been shown to reduce aging, thereby increasing the useful lifetime of the fibre [70].

Photosensitivity and contact with metals are also issues with AgX fibres. Visible or UV exposure can lead to the forming of colloidal silver, resulting in a visible darkening of the fibre and increased IR losses. Metal contact is not advisable for silver halides, as AgClBr can corrode metals such as stainless steel and copper. Titanium, gold and ceramics are safe however.

4.5.2 Open Path Cells

Open path cells (OPC) are attractive for liquid and gas sensing because of their relative ease of incorporation into collimated beam systems like FTIR spectrometers. Only two OAPMs were required: one to collimate the QCL emission and

steer the beam through the cell, and another to focus the collimated beam from the cell onto the MIR detector (Figure 4.4).

Two OPCs were used to investigate liquid and gas sensing with the Fabry-Perot laser. Liquid sensing was accomplished using a 150μm NaCl-windowed cell (Figure 4.6) - the high optical power of the QCL allowed for liquid samples to be sampled in this otherwise long optical path length. Samples in water solutions could not be probed due to the high solubility of NaCl (37.7g per 100g of water), therefore ethanol and methanol (0.79g NaCl per 100g methanol) were used as the bulk solution. Acetic acid samples (0.33g NaCl per 100g acetic acid) were interrogated using a desktop peristaltic pump (Gilson Minipuls 3) to deliver samples to the OPC.

Figure 4.6: NaCl windowed cell for aqueous acetic acid sensing

Gaseous acetone in nitrogen and sublimated formaldehyde in nitrogen were analysed using a 10cm long CaF_2 windowed glass cell (Figure 4.7). Using a gas saturating apparatus similar to that used previously for generating relative humidity mixtures (cf. Figure 3.9), a mass flow controller (MFC) passed dry N_2 through three liquid acetone filled gas wash-bottles in series, producing a acetone/N_2 mixture with an acetone concentration of 34% (the acetone saturation limit in nitrogen). This was then diluted with another N_2 stream, producing acetone mixtures with concentrations as low as 6.8 parts per thousand by mole (pptm) and was limited by the lower flow limit of the MFCs. A similar acetone/N_2 mixing apparatus was reported [71].

Paraformaldehyde prills ($[CH_2O]_n$; Aldrich) were heated to produce gaseous

formaldehyde in nitrogen. Sublimating at 150°C, samples were initially tested with the gas OPC using a FTIR spectrometer (Thermo Nicolet; Nexus 470 FTIR). A measured mass of $[CH_2O]_n$ prills were heated in a flask connected to the gas open path cell by Tygon 1/4" tubing. By calculating the volume of N_2 in the (N_2-purged) flask and cell, and careful weighing of the paraformaldehyde pre-heating, percentage molar concentrations of formaldehyde gas were generated.

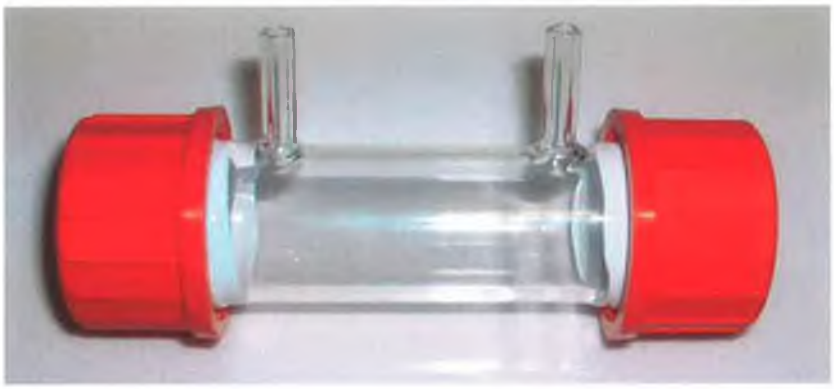

Figure 4.7: 10cm CaF_2 windowed cell for gas sensing

4.5.3 Hollow Waveguides

Hollow waveguides (HWG) are air-cored fibres ideally suited for IR spectroscopic sensing. Available as "leaky" (inner core refractive index $n > 1$) or ATR ($n < 1$) guides, HWGs have very low infrared absorption losses due to the air core [72]. Of interest are the so-called leaky ($n > 1$) waveguides - low cost devices, they consist of metallic and dielectric layers coated on the inside of metallic, plastic or glass tubes.

First put forward in 1964 [73] and demonstrated as an alternative to IR fibres for delivering high power CO_2 laser energy in 1980 [74], HWGs losses have been well documented. For circular cross section HWGs, optical loss depends on the wavelength of transmitted light λ and the bore diameter a; in general [73, 75], the loss or absorption coefficient α for HWGs is given by

$$\alpha \propto \frac{\lambda^2}{a^3} \tag{4.4}$$

Therefore optical losses can be minimised by increasing bore size, a useful property for IR spectroscopy where signal throughput is a concern. Bending losses also contribute to overall optical loss: below a critical bending radius R_c, bending losses vary as $1/R$ but above R_c show a $1/R^2$ dependence [76].

Coating the inside of a flexible tube with a single metallic coating will increase its optical transmission properties considerably; adding a dielectric coating similar

to that found on highly reflective mirrors would reduce the optical losses even further. Although coating alternating layers of high (n_H) and low (n_L) refractive index materials of thicknesses $\lambda/4n_H$ and $\lambda/4n_L$ should maximise reflectivity of the inner tube [77], difficulties in constructing alternating layer stacks have meant that a single dielectric layer coated on a highly reflective metal is most commonly used. The thickness of this single layer d can be tailored to maximise transmission at a particular wavelengh λ_{opt} by

$$d = \frac{\lambda_{opt}}{2\pi\sqrt{n_d^2 - 1}} \arctan\left[\frac{n_d}{\sqrt{n_d^2 - 1}}\right] \tag{4.5}$$

where n_d is the dielectric layer refractive index [75].

Not only do HWGs have very high transmission, but the hollow core can be used to confine and spectroscopically interrogate a gaseous sample. QCL based sensors using HWGs as the optical cell have already been demonstrated, for ethylene [78] and ethyl chloride [79].

Two silica HWGs, manufactured by Natan Croitoriu at Tel Aviv University, were used for spectroscopic analysis with the DFB and FP-QCLs. The inner walls of both were coated firstly with silver (Ag) and then a dielectric layer of silver iodide (AgI) (further details can be found with the US Patent Office [80]). A 2mm inner diameter (i.d.) HWG of length 55.6cm was used to sense propylene in air and a 0.7mm i.d. HWG of length 89.9cm, coated on the outside with a polymer for mechanical stability, was used to sense gaseous acetone in nitrogen.

Gas injection cells were used to allow injection and removal of sample gases to the HWGs and purging. As the diameters of the HWGs were different, two separate models had to be used. With an IR transmitting window at one end, screw-down Teflon sealing at the other and a side-facing inlet/outlet, a gas injection cell fitted over each end of the HWG allowed laser light into the hollow core while ensuring tight and consistent sealing for sample confinement.

The optical configuration used was similar to the configuration used for FEWS experiments with silver halide fibres (Figure 4.3), where laser emission was focused into the waveguide through the windows (ZnSe for 2mm HWG; Sapphire for 0.7mm HWG) and onto a MIR detector using off axis parabolic mirrors (Figures 4.8 and 4.9).

The DFB-QCL ($\lambda = 6.0\mu$m) was used to sense gaseous propylene with the 2mm i.d., 55.6cm long HWG. Commercial propylene gas (C_3H_6; Aldrich,; $\geq$ 99%) was piped directly into Tedlar bags, sampled with a microlitre gas syringe (Agilent; 10μl), and mixed with ambient air in sealed 100ml volumetric flasks.

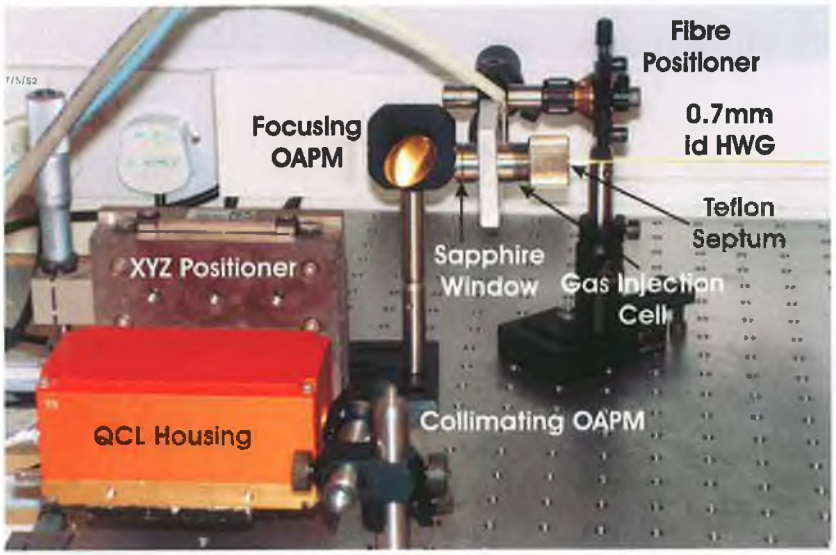

Figure 4.8: QCL coupling optics for 0.7mm i.d. HWG

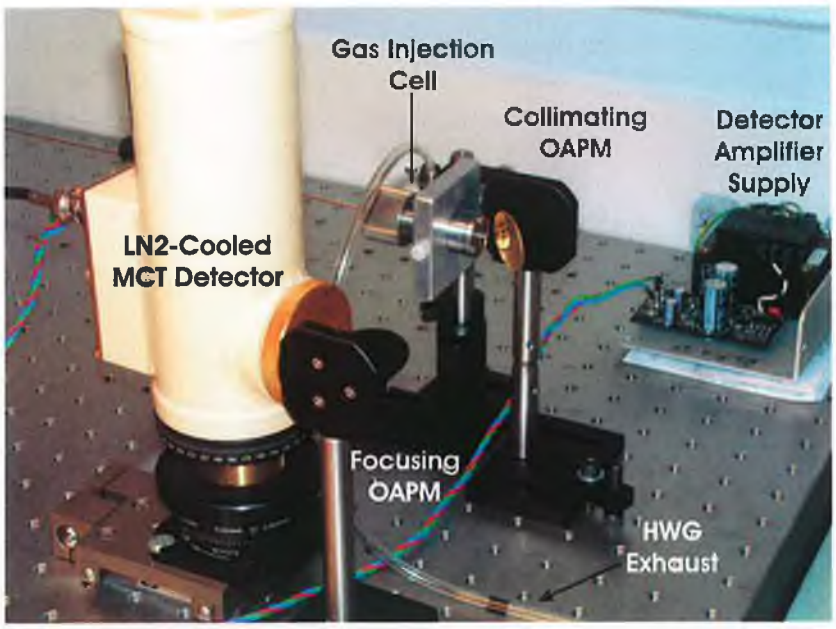

Figure 4.9: Out-coupling optics for 0.7mm i.d. HWG

Laser emission from the FP-QCL ($\lambda = 5.625\mu$m) was coupled into the 0.7mm i.d., 89.9cm long HWG for detecting acetone in nitrogen. Acetone/N_2 mixtures were generated using the apparatus explained previously, collected in gas bags, and diluted in N_2-purged sealed 10ml volumetric flasks using a 10μl gas syringe.

4.6 MIR Detectors

A great many different types of IR detection technologies exist, generally divided into *thermal devices* and *photon devices* [81]. Thermal devices use the change in

some temperature-dependent parameter from optical absorption e.g. bolometers and pyroelectric detectors. Photon devices are based on a quantum event triggered by optical absorption, such as photoelectric emission or photoconductivity.

IR detectors span a large range in terms of size, complexity and expense. To develop a chemical sensor using a QCL, compactness, linear sensitivity and high speed operation were paramount, as well as a reliable detection principle. To this end, semiconductor photon devices were investigated.

4.6.1 Project Requirements

A wide range of IR detector materials were available, including silicon, germanium, lead salts (e.g. PbS and PbSe), mercury cadmium telluride (HgCdTe, or MCT), deuterated triglycine sulfate (DTGS), indium gallium arsenide (InGaAs), indium antimonide (InSb), and indium arsenide (InAs). A review of available mid infrared detectors was carried out to find the most suitable device for use with a QCL emitting at $\lambda = 6.0\mu$m.

As some materials had cut-off wavelengths (λ_{co}) below the QCL emission wavelength, silicon ($\lambda_{co} = 1.1\mu$m), Ge ($\lambda_{co} = 1.7\mu$m), InGaAs ($\lambda_{co} = 2.2\mu$m), PbS ($\lambda_{co} \sim 4\mu$m with cooling), InAs ($\lambda_{co} = 3.5\mu$m), and InSb ($\lambda_{co} = 5\mu$m) were not included in the detector review.

The majority of MIR detectors were photoconductive and photodiode MCT devices, with a substantial difference in response times e.g one range of photoconductive MCTs had $\tau_{90} = 0.5\mu$s, whereas the photodiode MCTs from a different supplier had $\tau_{90} = 7$ns. The QCL was operated in pulsed mode at duty cycles of the order of 1% to prevent damage to the QCL by thermal stress. As such, the current pulses driving the laser were of the order of 20ns, as were the emitted laser pulses. Therefore photodiode detectors were required to resolve the pulses.

One of the most critical aspects of detector selection was the D* figure at the laser wavelength. Available detectors had D* ranges from 8×10^7 to 7×10^{10} cm$\sqrt{\text{Hz}}\,\text{W}^{-1}$. The method of detector cooling was equally important, as most thermoelectrically cooled devices exhibited lower D* than their liquid nitrogen cooled counterparts.

Some detectors were equipped with windows to protect the sensing element. Numerous window options were available, including barium fluoride (BaF_2), silicon, germanium (Ge), sapphire, CaF_2, cadmium telluride (CdTe), and zinc selenide (ZnSe). Another option that was available with some detectors was an integrated preamplifier stage.

4.6.2 Mercury Cadmium Telluride (HgCdTe) Detector

A mercury cadmium telluride (HgCdTe, or MCT) IR photodiode detector, configured for photovoltaic operation, was purchased (Kolmar Technologies; ref. KPMV8-0.5-J1/DC; **Appendix C**). Detector specifications included $D^* = 7 \times 10^{10}$ $cm\sqrt{Hz}\,W^{-1}$, an active area of $0.5 \times 0.5mm^2$, $\lambda_{co} \geq 8\mu m$, minimum $\tau_{90} = 7ns$, BaF_2 window and an integrated preamplifier. Although more sensitive than thermoelectrically cooled IR detectors, liquid nitrogen cooling to 77K was required for a satisfactory noise performance. To accommodate this, the detector came installed within a Dewar that had a 12 hour hold time.

4.7 Data Acquisition

For the FEWS liquid water and HWG gaseous propylene experiments, MIR absorption signals were measured using a digital storage oscilloscope (Tektronix) and recorded manually. This was improved upon with a Saturn FastScan DAQ card (AMO GMbH), capable of dual channel million-sample averaging and with a maximum sampling rate of 100MHz.

4.7.1 Pulse Amplitude Referencing

It has been documented in the literature that one of the major sources of noise in a pulsed laser system is pulse to pulse intensity variation [18, 82, 83, 84, 85]. Relative intensity noise from 3-level QCLs has been attributed to spontaneous emissions and non-radiative electron-phonon scattering losses and was found to scale in a power series with the number of active region gain stages [85]. However, another potential source of intensity noise was cited as being the QCL supply electronics [18]. A study was carried out to determine the relationship between laser supply current noise and laser intensity fluctuations. Intensity noise can have drastic consequences on the capabilities of a QCL spectrometer, as the signal-to-noise ratio (SNR) decreases with increasing intensity fluctuations.

The Saturn FastScan DAQ card was initially used to average the MCT detector signal, improving SNR. It was then employed to investigate a correlation between laser current and emission noise.

The possibility of using the TPG-128 pulse generator as a reference was investigated. First of all, evidence of an actual correlation between current pulse and laser emission noise had to be established, if any existed at all. Then a process to reference the laser pulses against the current pulses had to be implemented,

e.g. whether to directly ratio the corresponding pulse amplitudes or use lineshape fitting to calculate pulse areas.

Previously, it was impossible to analyse the QCL output and pulse generator together as there was no way to store both datasets while simultaneously sampling both. With the implementation of the Saturn FastScan DAQ system however, both signals could be sampled and stored separately. One channel was used to acquire the MCT signal in response to the MIR laser emission, while the other was assigned to collecting current pulse data from a secondary output on the TPG128 pulse generator. Triggering was accomplished using a triggering output on the TPG128 that preceded the main output pulse by about 100ns.

A program was written in LabVIEW 7.0 to automatically extract pulse amplitudes from *.sdf* file folders, thus saving time by removing the need to convert and open each *.sdf* file. Incorporating a program that was developed by Martin Bruckerscheifer (Georgia Institute of Technology) that translated *.sdf* files, the program was run post-experiment on the folder containing the experimental scans, extracting the MCT detector and reference pulse amplitudes and writing both datasets to a text file. The data was then readily plotted using Microsoft Excel or Microcal Origin.

4.8 Summary

Although currently QCLs are expensive devices (approximately $20,000 for a room temperature device at a custom wavelength), as the design and construction process of QCL matures the author expects to see a drop in prices in the coming years. This will be aided by the proliferation of research carried out presently into both QCL applications (driving the demand) and alternative designs and materials for the lasers (enabling new manufacturers to enter the market).

Two quantum cascade lasers were used as spectroscopic sources for sensing a range of chemicals, including the biomarkers acetone and formaldehyde. A common-base optical configuration for optically coupling the lasers to optical fibres, hollow waveguides and open path cells was also developed. Although gas phase analytes were primarily investigated, water and acetic acid were also analysed. To minimise spectroscopic noise from laser amplitude fluctuations, a series of data comparison regimes were investigated to allow pulse amplitude referencing.

Bibliography

[1] Beck M., Hofstetter D., Aellen T., Blaser S., Faist J., Oesterle U. and Gini, E., *J. Crys. Growth* **251 (1–4)** 697–700 (2003)

[2] Blaser S., Yarekha D.A., Hvozdara L., Bonetti Y., Muller A., Giovannini M. and Faist, J., *Appl. Phys. Lett.* **86 (4)** Art. No. 041109 (2005)

[3] Shore K.A., *Laser Focus World* **38 (6)** 85 (2002)

[4] Martini R., Gmachl C., Paiella R., Capasso F., Whittaker E.A., Liu H.C., Hwang H.Y., Sivco D.L., Baillargeon J.N. and Cho A.Y., *Elec. Lett.* **37 (21)** 1290–1292 (2001)

[5] Martini R., Bethea C., Capasso F., Gmachl C., Paiella R., Whittaker E.A., Hwang H.Y., Sivco D.L., Baillargeon J.N. and Cho A.Y., *Elec. Lett.* **38 (4)** 181–183 (2002)

[6] Namjou K., Cai S., Whittaker E.A., Faist J., Gmachl C., Capasso F., Sivco D.L. and Cho A.Y., *Opt. Lett.* **23 (3)** 219–221 (1998)

[7] Sharpe S.W., Kelley J.F., Hartman J.S. Gmachl C., Capasso D., Sivco D.L., Baillargeon J.N. and Cho A.Y., *Opt. Lett.* **23 (17)** 1396–1398 (1998)

[8] Kosterev A.A., Curl R.F., Tittel F.K., Gmachl C., Capasso F., Sivco D.L., Baillargeon J.N., Hutchinson A.L. and Cho A.Y., *Appl. Opt.* **39 (24)** 4425-4430 (2000)

[9] Murry S., Hwang W.Y. and Baillargeon J., *III-Vs Review* **14 (3)** 48–50 (2001)

[10] Hvozdara L., Pennington N., Kraft M., Karlowatz M. and Mizaikoff B., *Vib. Spec.* **30 (1)** 53–58 (2002)

[11] Weber W.H., Remillard J.T., Chase R.E., Richert J.F., Capasso F., Gmachl C., Hutchinson A.L., Sivco D.L., Baillargeon J.N. and Cho A.Y., *Appl. Spec.* **56 (6)** 706–714 (2002)

[12] Wysocki G., Kosterev A.A. and Tittel F.K., *Appl. Phys. B* **80 (4-5)** 617–625 (2005)

[13] Lackner M., Forsich C., Winter F., Anders S. and Strasser G., *Opt. Comms.* **216** 357–360 (2003)

[14] Burkert A., Paa W., Schmidl G., Triebel W. and Eigenbrod C., *Acta Astronautica* **55** 199–209 (2004)

[15] Baren R.E., Parrish M.E., Shafer K.H., Harward C.N., Shi Q., Nelson D.D., McManus J.B. and Zahniser M.S., *Spec. Acta A* **60** 3437–3447 (2004)

[16] Nelson D.D., McManus J.B., Shorter J.H. and Zahniser M.S., *Appl. Phys. B* **75** 343–359 (2002)

[17] Kosterev A.A., Tittel F.K., Köhler R., Gmachl C., Capasso F., Sivco D.L., Cho A.Y., Wehe S. and Allen M.G., *Appl. Opt.* **41 (6)** 1169–1173 (2002)

[18] Nelson D.D., McManus J.B., Urbanski S., Herndon S. and Zahniser M.S., *Spec. Acta A* **60** 3325–3335 (2004)

[19] Jimenez R., Taslakov M., Simeonov V., Calpini B., Jeanneret F., Hofstetter D., Beck M., Faist J. and Van den Bergh H., *Appl. Phys. B* **78 (2)** 249–256 (2004)

[20] da Silva M.G., Vargas H., Miklos A. and Hess P., *Appl. Phys. B* **78 (6)** 677–680 (2004)

[21] Sonnabend G., Wirtz D., Vetterle V. and Schieder R., *Astronomy & Astrophysics* **435 (3)** 1181–1184 (2005)

[22] Lendl B., Frank J., Schindler R., Müller A., Beck M. and Faist J., *Anal. Chem.* **72** 1645–1648 (2000)

[23] Edelmann A., Ruzicka C., Frank J., Lendl B., Schrenk W., Gornik E. and Strasser G., *J. Chrom. A* **934 (1–2)** 123–128 (2001)

[24] Kölhed M., Haberkorn M., Pustogov V., Mizaikoff B., Frank J., Karlberg B. and Lendl B., *Vib. Spec.* **29** 283–289 (2002)

[25] Schaden S., Haberkorn M., Frank J., Baena J.R. and Lendl B., *Appl. Spec.* **58 (6)** 667–670 (2004)

[26] Kölhed M., Schaden S., Karlberg B. and Lendl B., *J. Chrom. A* **1083** 199–204 (2005)

[27] Pauling L., Robinson A.B., Teranishi R. and Cary P., *Proc. Nat. Academy Sci. USA* **68 (10)** 2374–2376 (1971)

[28] Manolis A., *Clin. Chem.* **29 (1)** 5–15 (1983)

[29] Cheng W.H. and Lee W.J., *J. Lab. Clin. Med.* **133 (3)** 218–228 (1999)

[30] Miekisch W., Schubert J.K., Vagts D.A. and Geiger K., *Clin. Chem.* **47 (61)** 1053–1060 (2001)

[31] Miekisch W., Schubert J.K. and Noeldge-Schomburg G.F.E., *Clinica Chim. Acta* **347 (1–2)** 25–39 (2004)

[32] Ament W., Huizenga J.R., Kort E., van der Mark T.W., Grevnik R.G. and Verkerke G.J., *Int. J. Sports Med.* **20** 71–77 (1999)

[33] Narasimhan L.R., Goodman W., Kumar C. and Patel N., *PNAS 98* **8** 4617–4621 (2001)

[34] Chen S., Mahadevan V. and Zieve L., *J. Lab. Clin. Med.* **75** 622–627 (1970)

[35] Ebeler S.E., Clifford A.J. and Shibamoto T. *J. Chrom. B* **702 (1–2)** 211–215 (1997)

[36] Phillips M., *Lancet* **353 (9168)** 1930–1933 (1999)

[37] Spanel P., Smith D., Holland T.A., Al Singary W. and Elder J.B., *Rapid Commun. Mass Spectrom.* **13 (14)** 1354–1359 (1999)

[38] Kato S., Burke P.J., Fenick D.J., Taatjes D.J., Bierbaum V.M. and Koch T.H., *Clin. Res. Toxicol.* **13 (6)** 509–516 (2000)

[39] Kato S., Burke P.J., Koch T.H. and Bierbaum V.M., *Anal. Chem.* **73 (13)** 2992–2997 (2001)

[40] Li J.Z., Dasgupta P.K. and Luke W., *Anal. Chim. Acta* **531 (1)** 51–68 (2005)

[41] von Lilienfeld-Toal H., Weidenmüller M., Xhelaj A. and Mäntele W., *Vib. Spec.* **38** 209–215 (2005)

[42] Martin W.B., Mirov S. and Venugopalan R., *Appl. Spec.* **59 (7)** 881–884 (2005)

[43] Kosterev A.A., Tittel F.K., Durante W., Allen M., Kohler R., Gmachl C., Capasso F., Sivco D.L. and Cho A.Y., *Appl. Phys. B* **74 (1)** 95–99 (2002)

[44] Roller C., Kosterev A.A., Tittel F.K., Gmachl C. and Sivco D.L., *Opt. Lett.* **28 (21)** 2052–2054 (2003)

[45] Menzel L., Kosterev A.A., Curl R.F., Tittel F.K., Gmachl C., Capasso F., Sivco D.L., Baillargeon J.N., Hutchinson A.L., Cho A.Y. and Urban W., *Appl. Phys. B* **72 (7)** 859-863 (2001)

[46] Bakhirkin, Y.A., Kosterev, A.A., Roller, C., Curl, R.F., Tittel, F.K., *Appl. Opt.* **43 (11)** 2257–2266 (2004)

[47] Hvozdara L., Gianordoli S., Strasser G., Schrenk W., Unterrainer K., Gornik E., Murthy C.S., Kraft M., Pustogow V. and Mizaikoff B., *Physica E* **7** 37–39 (2000)

[48] Schilt S., Thevenaz L. and Courtois E., *Spec. Acta A* **58 (11)** 2533–2539 (2002)

[49] Garcia M., Normamd E., Stanley C.R., Ironside C.N., Farmer C.D., Duxbury G. and Langford N., *Opt. Comms.* **226** 39–43 (2003)

[50] Kosterev A.A., Curl R.F., Tittel F.K., Köhler R., Gmachl C., Capasso F., Sivco D.L. and Cho A.Y., *Appl. Opt.* **41 (3)** 573–578 (2002)

[51] Beyer T., Braun M. and Lambrecht A., *J. Appl. Phys.* **93 (6)** 3158–3160 (2003)

[52] Gagliardi G., Tamassia F., De Natale P., Gmachl C., Capasso F., Sivco D.L., Baillargeon J.N., Hutchinson A.L. and Cho A.Y. *Eur. Phys. J. D* **19 (3)** 327–331 (2002)

[53] Morimoto Y., Durante W., Lancaster D.G., Klattenhoff J. and Tittel F.K., *Amer. J. Phyisiology* **280 (1)** H483–H488 (2001)

[54] Schilt S., Vicet A., Werner R., Mattiello M., Thevenaz L., Salhi A., Rouillard Y. and Koeth J., *Spec. Acta. A* **60 (14)** 3431–3436 (2004)

[55] Janusch M., Mizaikoff B., Kellner R. and Katzir A., *Sensors and Actuators B* **38** 83–87 (1997)

[56] Regan F., Meaney M., Vos J.G., MacCraith B.D. and Walsh J.E., *Anal. Chim. Acta* **334** 85–92 (1996)

[57] Lu Y., Han L., Brinker C.J., Niemczyk T.M. and Lopez G., *Sensors and Actuators B* **36** 517–521 (1996)

[58] Weinstock B., Yang H. and Griffiths P., *Vib. Spec.* **35** 145–152 (2004)

[59] Lima R.R., Carvalho R.A.M., Nascimento Filho A.P., Silva M.L.P. and Demarquette N.R., *Sensors and Actuators B* **108** 435–444 (2005)

[60] Takahashi K., Yosjide N. and Yokota M., *Sumitomo Electric Tech. Rev.* **23** 203–210 (1984)

[61] Harrington J.A., *Infrared Fibers and Their Applications* 105–137 (Ch. 6) (2004)

[62] Moser F., Bunimovich D., DeRowe A., Eyal O., German A., Gotshal Y., Levite A., Nagli L., Ravid A., Scharf V., Shalem S., Shemesh D., Simchi R., Vasserman I. and Katzir A., *IEEE Selected Topics Q. Electron.* **2** 872–879 (1996)

[63] Kimura M., Kachi S. and Shiroyama K., *Proc. SPIE* **618** 85–88 (1986)

[64] Sakuragi S., *Proc. SPIE* **320** 2–9 (1982)

[65] Bunimovich D. and Katzir A., *Appl. Opt.* **32** 2045–2048 (1993)

[66] Katzir A., Silver Halide Crystals & Fibers, http://www.tau.ac.il/~applphys/agclbr.html

[67] Barkay N., Levite A., Moser F. and Katzir A., *J. Appl. Phys.* **64** 5256–5258 (1988)
Barkay N. and Katzir A., *J. Appl. Phys.* **74** 2980–2982 (1993)

[68] German A., Barkay N. and Katzir A., *Appl. Opt.* **33** 2734–2736 (1994)

[69] Kupper L., Heise H.M. and Butvina L.N., *J. Mol. Struct.* **563/564** 173–181 (2001)

[70] Grigorjeva L., Millers D., Kotomin E., Eglitis R. and Lerman A.A., *J. Phys. D* **29** 578–583 (1996)

[71] Yuen L.S., Peters J.E. and Lucht R.P., *Appl. Opt.* **36 (15)** 3271–3277 (1997)

[72] Harrington J.A., *Infrared Fibers and Their Applications* 39–56 (Ch. 6) (2004)

[73] Marcatili E.A.J. and Schmeltzer R.A., *Bell Syst. Tech. J.* **43** 1783–1809 (1964)

[74] Gamire E., McMahon T. and Bass M., *IEEE J. Quant. Elec.* **QE-16** 23–32 (1980)

[75] Miyagi M. and Kawakami S., *J. Lightwave Techn.* **LT-2** 116–126 (1984)

[76] Miyagi M., *Appl. Opt.* **20** 1221–1229 (1981)

[77] Miyagi M., Hongo A. and Kawakami S., *IEEE J. Quant. Electron.* **QE-19** 136–144 (1983)

[78] Hvozdara L., Gianordoli S., Strasser G., Schrenk W., Unterrainer K., Gornik E., Murthy C.S., Kraft M., Pustogow V., Mizaikoff B., Inberg A. and Croitoru N., *Appl. Opt.* **39 (36)** 6926–6930 (2000)

[79] Charlton C., de Melas F., Inberg A., Croitoru N. and Mizaikoff B., *IEE Proc.-Optoelectronics* **150 (4)** 306–309 (2003)

[80] Croitoriu N., Dror J., Goldenberg E., Mendelovic D., Israel G., US Patent Number 4,930,863, *"Hollow fiber waveguide and method of making same"* (1989)

[81] Wilson J. and Hawkes J., *Optoelectronics (Third Ed.)* (Prentice Hall Europe 1998), Chapter 7

[82] Normand E., Duxbury G. and Langford N., *Opt. Comms.* **197** 115–120 (2001)

[83] Zhang Y.G., Nan K.J. and Li A.Z., *Spec. Acta A* **58** 2323–2328 (2002)

[84] Taubman M.S., Myers T.L., Cannon B.D. and Williams R.M., *Spec. Acta A* **60** 3457–3468 (2004)

[85] Gensty T., Elsäßer W., Mann C., *Opt. Express* **13** (6) 2032–2039 (2005)

Chapter 5

Results and Analysis of Chemical Sensing

A range of analytes was interrogated using both experimental sensing systems. While the rare-earth based NIR fluorescence probe was limited in application to water sensing, the abundance of fundamental absorptions in the MIR allowed for a number of chemicals to be sensed using the two quantum cascade lasers. The 6.0μm DFB-QCL was used to detect water and propylene, and a number of chemicals with C=O bonds were detectable with the 5.6μm FP-QCL, such as acetic acid, acetone and formaldehyde. MIR absorption spectra of these chemicals acquired from the Jet Propulsion Laboratory and Virtual Planetary Laboratory spectroscopic database website [1], collated primarily from the Pacific Northwest National Laboratory (PNNL), are presented in Figure 5.1.

Damage sustained by the DFB-QCL during inspection meant that water and propylene experiments had to be put on hold. As a suitable off-the-shelf replacement laser could not be sourced - either the wavelength (6μm) was not available or laser emission was extensively multimode - it was decided to acquire a laser that spectrally overlapped with a different molecular absorption feature, namely the carbon-oxygen double bond stretching vibration (C=O). Although the replacement laser was a Fabry-Perot device and exhibited multimode emission at laser diode driver (LDD) voltages up to 11.0V and over the recommended QCL operating temperature range of $\pm$30°C, single mode operation was seen for LDD voltages greater than 11V.

Alpes Lasers QCLs can be run at duty cycles up to 5% with a maximum pulse length of 100ns. However, it was found that this can lead to periodic heating of the laser, shifting the emission wavelength by means of altering the effective refractive index of the DFB-QCL's etched Bragg grating or the QCL

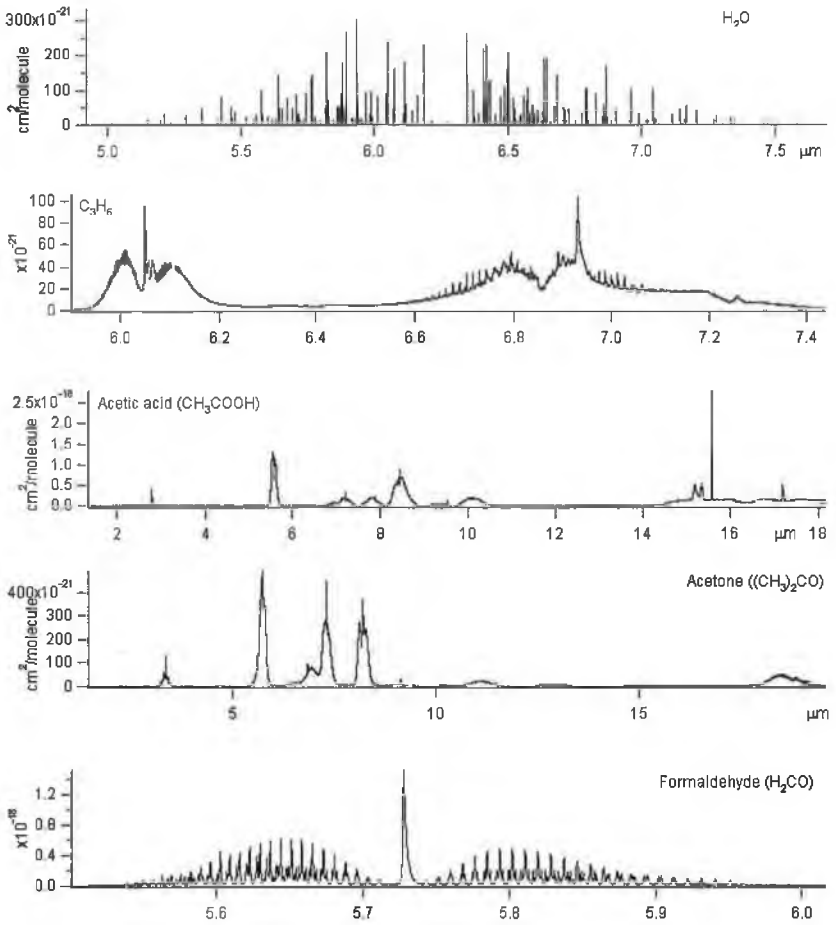

Figure 5.1: MIR absorption cross-sections for water, propylene (C_3H_6), acetic acid ($C_2H_4O_2$), acetone (C_3H_6O) and formaldehyde (H_2CO) (*spectra courtesy JPL/VPL*)

active region in the case of the FP-QCL. In order to minimise heating effects, both lasers were run at a pulse period of 5.5μs and a pulse length of 20ns, giving a duty cycle of 0.36%. The DFB-QCL was driven with a LDD voltage of 28V and held at a temperature of 10.0°C while the FP-QCL was driven at 13V at 5.0°C.

5.1 Data Analysis

The Beer-Lambert Law was used extensively to quantify the performance of the various NIR and MIR sensing mechanisms:

$$A = \log_{10} \frac{I_0}{I} \tag{5.1}$$

where I_0 is the laser signal with no absorbing analyte, I is the attenuated signal due to absorption and A is the absorbance.

Error bars were calculated by treating absorbance as a function of intensity i.e. $A = \mathrm{f}(I)$. For a general function $y = \mathrm{f}(x)$, the error in y, Δy, is expressed in

relation to the error Δx as

$$\Delta y(a) = \Delta x \frac{\mathrm{d}y}{\mathrm{d}x}\bigg|_{x=a} \tag{5.2}$$

Re-expressing Equation 5.1 as

$$A = \log_{10} I_0 - \log_{10} I = \frac{\ln I_0 - \ln I}{\ln 10} \tag{5.3}$$

and treating I_0 as constant, differentiating Equation 5.3 gives

$$\frac{\mathrm{d}A}{\mathrm{d}I} = -\frac{1}{I \ln 10} \tag{5.4}$$

In terms of errors, this signifies that the absorbance error can be related to the intensity noise ΔI by

$$\Delta A(I) = \frac{\Delta I}{I} \frac{1}{\ln 10} \tag{5.5}$$

The *limit of detection* is defined as the concentration derived from the smallest measure x_L that can be detected with reasonable certainty for a given analytical procedure [2]

$$x_L = \overline{x_{bi}} + k s_{bi} \tag{5.6}$$

where $\overline{x_{bi}}$ and s_{bi} are the mean and standard deviation of the blank measures i.e. of I_0 and k is a numerical factor chosen according to the confidence level desired (usually $k = 3$). In terms of concentration, this becomes

$$c_L = \overline{c_{bi}} + k s_{bi} S \tag{5.7}$$

where S is the *inverse sensitivity* $\mathrm{d}c/\mathrm{d}A$. As a "blank concentration" gives zero absorbance, $\overline{x_{bi}} = 0$, the limit of detection is therefore defined as [3]

$$c_L = k s_{bi} S \tag{5.8}$$

Limits of detection (LOD) were calculated using ICH[1] Guidelines on Method Validation Methodology as

$$LOD = 3\,\sigma_0 \frac{\mathrm{d}c}{\mathrm{d}A} = \frac{3\,\sigma_0}{m} \tag{5.9}$$

where σ_0 is the standard deviation of the I_0 response, $k = 3$, and $\mathrm{d}A/\mathrm{d}c$ is the sensitivity of the system. Plotting a calibration curve of absorbance versus concentration, the slope of the best-fit calibration curve $m = \mathrm{d}A/\mathrm{d}c$ was used to determine LOD.

[1]International Conference on Harmonization (of Technical Requirements for Registration of Pharmaceuticals for Human Use)

5.2 Relative Humidity Sensing

Full scale (0-100%) relative humidity (RH) sensing was feasible with the Laboratory-based Prototype, but the stability of the system over time was not optimal (Figure 5.2).

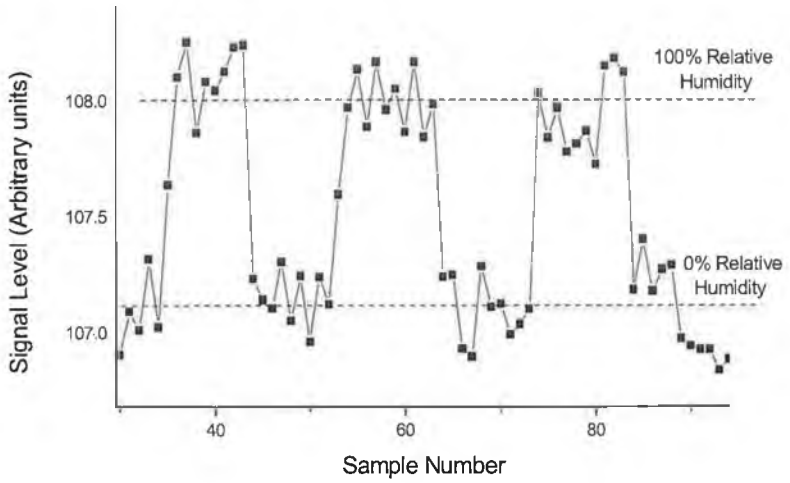

Figure 5.2: Full scale Relative Humidity measurements taken with the Laboratory-based Prototype

In the next iteration of the sensing system, a number of instrumental and electronic improvements were introduced (cf. **Chapter 3.1.2**). Chief amongst them was a method for real time monitoring of the PbS detector temperature. This became necessary due to increased scattering of the Reference beam at higher humidities. The critical effect the detector temperature has on sensitivity can be seen in Figure 5.3, where the detector was allowed reach thermal equilibrium with its surroundings after initial cooling using the mounted Peltier cooler. An in-built thermistor allowed the detector temperature to be monitored. The output signal, and correspondingly the detector response, was found to vary inversely with temperature. This is due to the temperature dependence of the detector resistance. As the detector is a photoconductive device, incident radiative intensity changes are expressed as a change in the voltage applied across the detector.

The thermistor resistance (R_{TH}) is known to have an exponential relationship with temperature T_{TH} (Figure 5.4; Equation 5.10)

$$R_{TH} = 3.0861 \exp(-0.0449 T_{TH}) \tag{5.10}$$

A voltage divider was used to monitor the thermistor resistance and so track temperature shifts. The fitted equation was employed in LabVIEW to convert the voltage signal to a temperature reading.

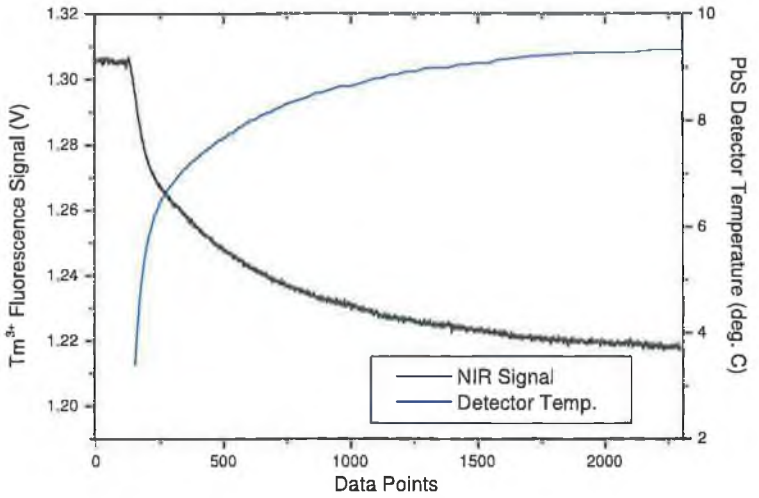

Figure 5.3: PbS detector responsivity varying with temperature

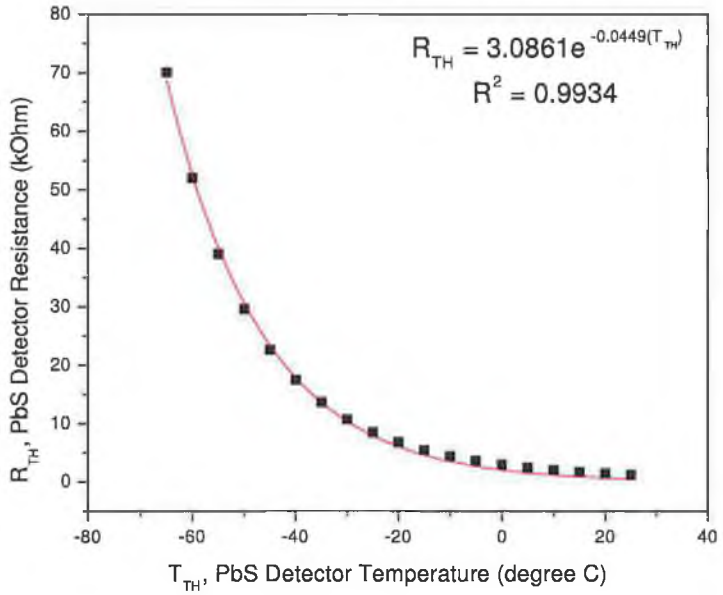

Figure 5.4: Thermistor curve for PbS Quad Detector

Using the nitrogen mixing apparatus (Figure 3.9) and a Eirelec (Dundalk, Co. Louth, Ireland) relative humidity capacitive sensor for calibration, a number of experiments were carried out to determine the response of the Industrial Prototype to RH changes. As can be seen in Figure 5.5, the stability of the system was much improved. The small fluctuation present in the first 100% RH mixing procedure correlated with a small change in the temperature of the PbS detector, as monitored using LabVIEW. The mixing apparatus was left running for a few

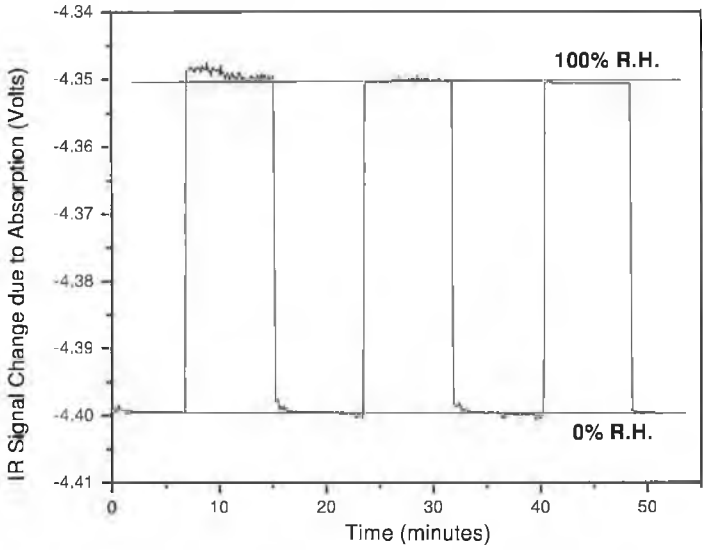

Figure 5.5: Full scale Relative Humidity measurements taken with the Industrial Prototype

minutes prior to data acquisition to allow the sought RH value to stabilise. This was checked by the Eirelec RH sensor mounted on the exhaust line.

Smaller relative humidities were achieved by mixing the "wet" (humidified) N_2 stream with the "dry" N_2 stream, with a lower RH concentration limit set by the flow capabilities of the MFCs (2%). Signal stability was limited by temperature fluctuations (Figure 5.6) but once thermally stabilised, a marked improvement was seen(Figure 5.7).

Absorbance data were derived from Figure 5.7 and a linear trend was fitted to the data (Figure 5.8). The LOD was calculated as 3.71% RH. Detection of RH levels higher than 50% was impeded by condensation inside the gas cell.

The capability of using the coaxial $\lambda = 685$nm pump beam to reference detector thermal drift was limited by Rayleigh scattering at high RH levels. While scattering did not significantly affect the quasi-collimated NIR probe beam, the narrow collimated pump beam was affected. Referencing with the pump laser beam was not found to appreciably improve signal to noise ratios and was not used in the experiments described previously.

An improvement in system stability has been achieved by removing the multiplexer switch and redesigning the optical configuration, replacing the PbSe NIR detector with a more sensitive PbS device, and monitoring the detector temperature. The incorporation of these improvements into a single modular sensing platform has resulted in a modulatable RH sensor (the Industrial Prototype).

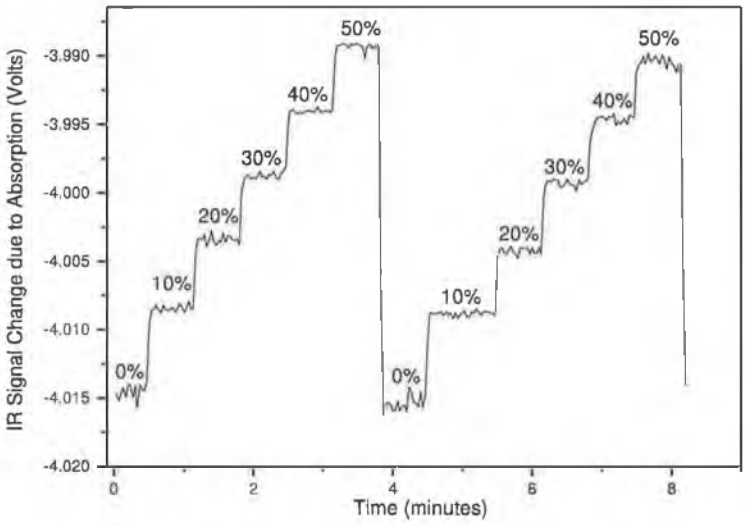

Figure 5.6: Two 0–50% RH scans using the Industrial Prototype

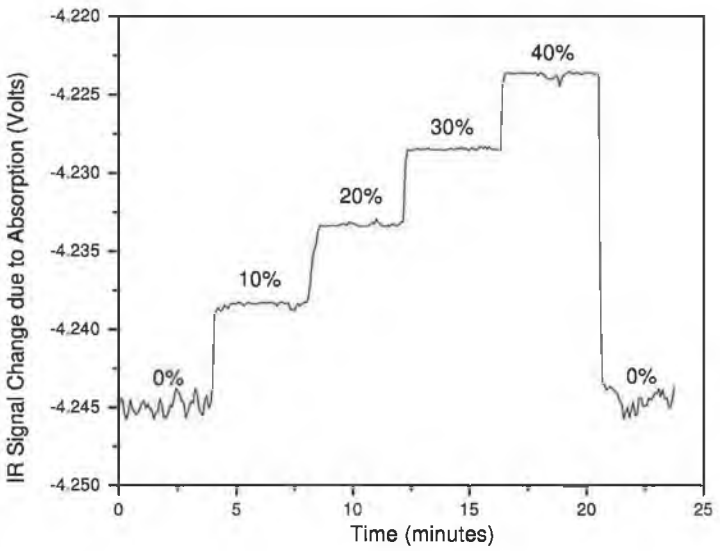

Figure 5.7: Stability of temperature stabilised Industrial Prototype

The sensor has been successfully demonstrated using a nitrogen humidifier and is capable of full scale (0–100%) RH sensing with a limit of detection of 3.71% RH over an optical path length of 10cm. Further improvements in sensitivity and LOD could be achieved by using a longer or multi-pass optical cell, or the addition of a further amplification stage onto the platform's detector electronics.

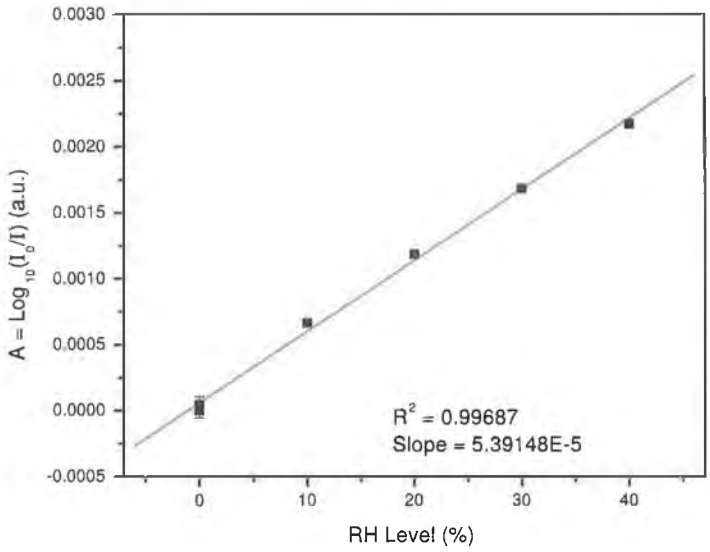

Figure 5.8: Relative humidity absorbance

5.3 Quantum Cascade Laser Spectroscopy

Two QCLs were used in a number of spectroscopic configurations to establish their suitability for sensing a number of chemicals. Liquid water and gaseous propylene were detected using the $\lambda = 6\mu$m DFB-QCL as a spectroscopic source, while the $\lambda = 5.625\mu$m FP-QCL was used to detect acetic acid in liquid phase, and gaseous formaldehyde and acetone. A number of methods to reduce spectroscopic noise caused by QCL intensity fluctuations were investigated.

5.3.1 Pulse Amplitude Referencing

Initial spectroscopic experiments with the DFB-QCL were carried out using a digital storage oscilloscope to record laser intensity readings from which absorbance data was eventually derived. It was observed that without an absorbing chemical in the optical path, the laser signal fluctuated. Later experiments using the FP-QCL and the Saturn FastScan DAQ system confirmed that the laser intensity varied over time (Figure 5.9). As the optical intensity fluctuations were a key contributor to absorbance noise, it became necessary to minimise the effects of the fluctuations in order to optimise the system's *signal-to-noise ratio* (SNR).

Averaging sample signals over a longer period diminished the effects of this noise considerably, but a method was sought to further reduce the fluctuation effects by referencing changes in laser intensity with variations in the drive current.

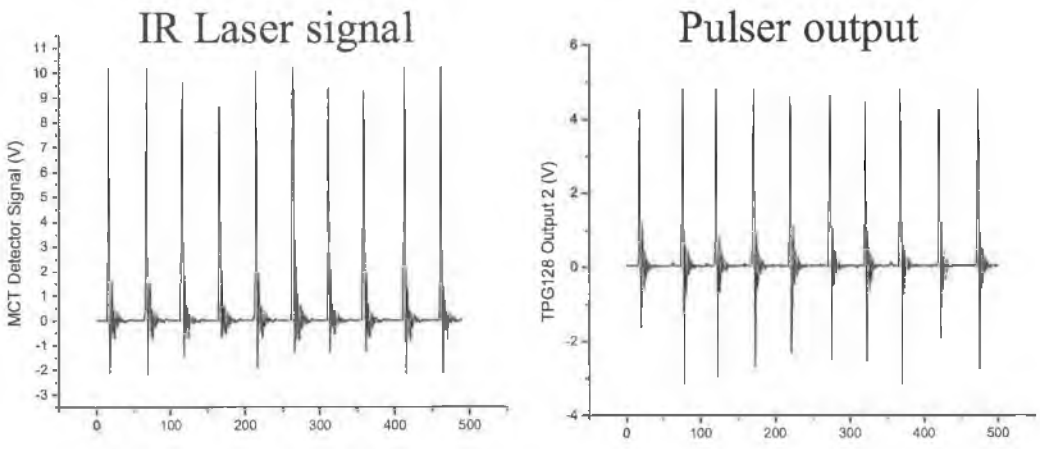

Figure 5.9: Pulse-to-pulse fluctuations in laser (left) and current pulser (right). Both datasets graphed with apparent increased duty cycle

Due to the maximum sampling rate of 100MHz for the DAQ card and the very short laser pulse widths (20ns), each pulse was not perfectly resolved during each scan. This ultimately led to averaged pulses without a true peak value. In an attempt to resolve this, and thus eliminate inconsistencies resulting from the digital sampling process, line fitting was employed to derive a "true" peak for each averaged pulse. It emerged that a Lorentzian lineshape best fitted the pulses (Figure 5.10), and to improve the SNR further, the area under each fitted curve was used for spectroscopic evaluation. An example of the SNR improvement using the Lorentzian fitting was seen in an experiment where dry nitrogen was flowed though a 10cm open path cell. Although the Lorentzian fitting improved the SNR, the actual fitting mechanism had to be carried out manually in Microcal Origin 6.0 for each averaged pulse. As a regular scan to probe an IR-absorbing material can have up to as many as 150 averaged pulses (for collecting sufficient data to derive an expanded zero intensity (I_0) and to allow any mixing in the sample to stabilise), fitting each of these averaged pulses was extremely laborious.

The possibility of using the TPG-128 pulse generator as a reference was investigated. First of all, evidence of an actual correlation between current pulse and laser emission noise had to be established, if any existed at all. Then a process to reference the laser pulses against the current pulses had to be implemented, e.g. whether to directly ratio the corresponding pulse amplitudes or use Lorentzian fitting to calculate pulse areas.

Previously, it was impossible to analyse the QCL output and pulse generator together as there was no way to store both datasets while simultaneously sampling both. With the implementation of the Saturn FastScan DAQ system however,

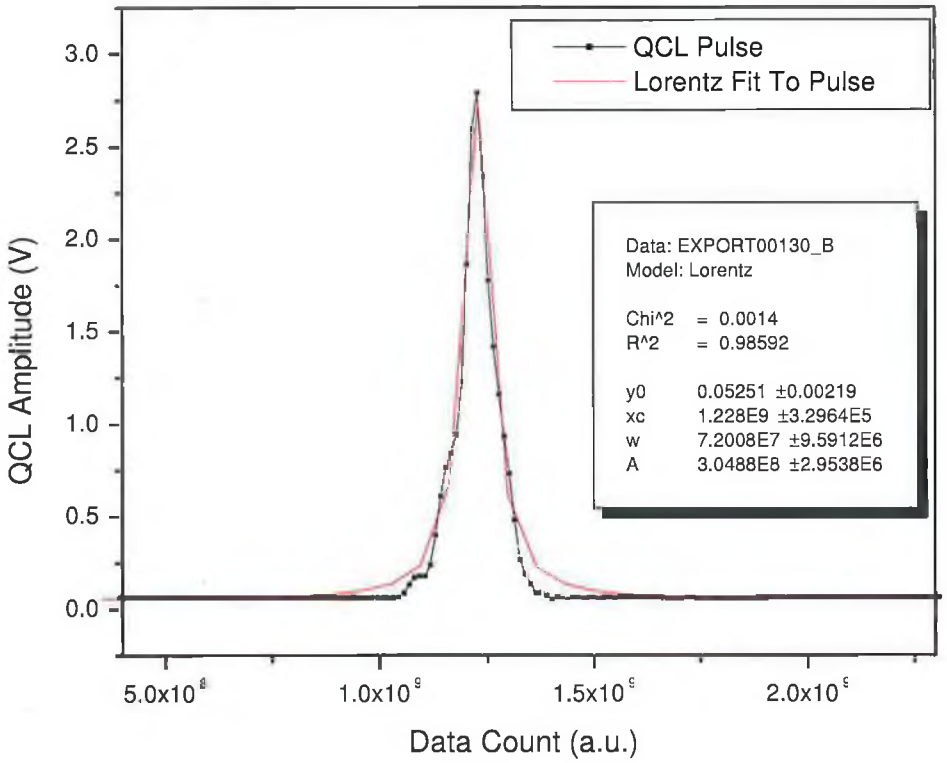

Figure 5.10: Example of Lorentzian fitting to QCL signal ($R^2 = 0.98592$)

both signals could be sampled and stored separately. One channel was used to acquire the MCT signal in response to the MIR laser absorption, while the other channel was assigned to collect current pulse data from a secondary output on the TPG128 pulse generator. Triggering was accomplished using a triggering output on the TPG128 that preceded the main output pulse by about 100ns. Using this data acquisition setup, evidence was found of a correlation between the QCL fluctuations and the current pulse generator. The current pulse data was found to trace the amplitude fluctuations of the MCT signal (Figure 5.11). A SNR value of 134 for the the raw infrared MCT signal was calculated.

These data were analysed further to determine which comparison regime might yield better results. Both the averaged laser pulses and the averaged current pulses were curve fitted using a Lorentzian lineshape. Figure 5.12 shows a graph of the pulse generator amplitudes plotted against the IR signal from the MCT detector. Similarly, Figure 5.13 displays the fitted curve areas from the two channels plotted against one another. Comparing the regression coefficients for both, it appeared that the amplitude fluctuations matched better than the fitted

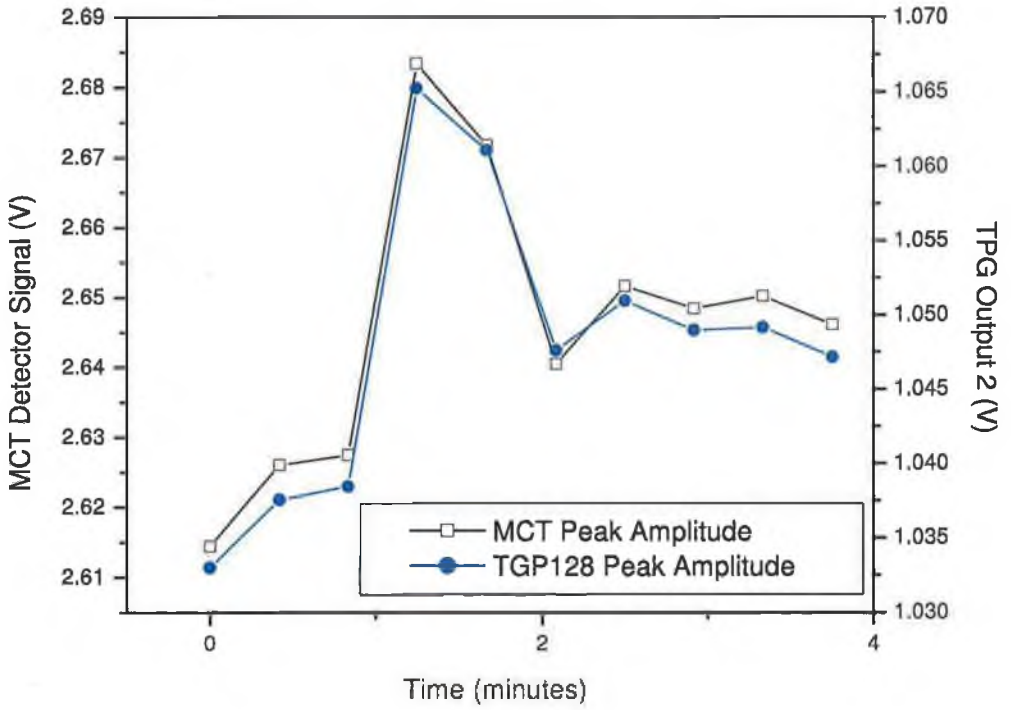

Figure 5.11: Dataset showing similarities between laser emission and pulser signal curve area fluctuations (R^2 (amplitude) = 0.9903; R^2 (area) = 0.9878).

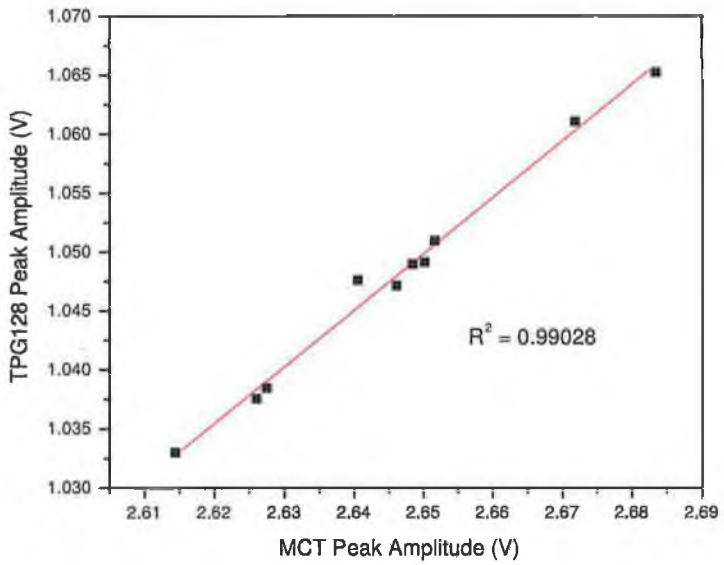

Figure 5.12: Linear fit of averaged pulse amplitude data

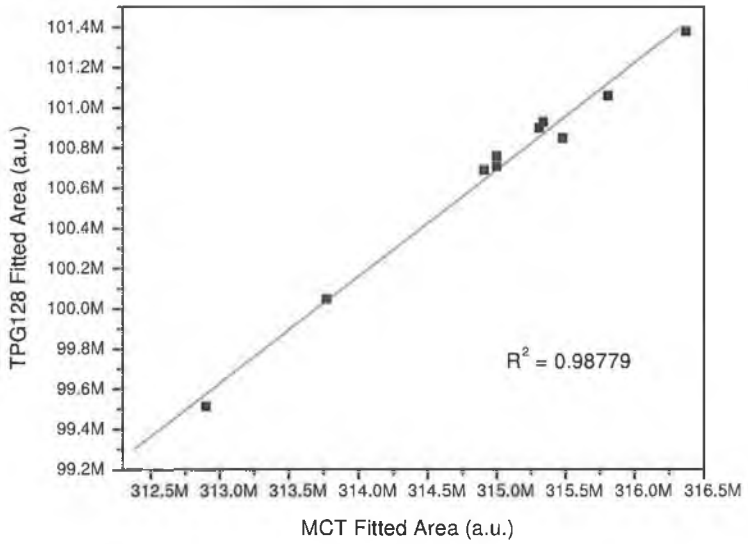

Figure 5.13: Linear fit of averaged Lorentzian fit data

This suggested that using the amplitude of the current pulses to reference the MIR signal would yield better results than referencing with the fitted curve areas. A comparison of the SNR improvement using referencing also supports this conclusion: the SNR of the referenced Lorentzian fitted areas was 482, while the SNR resulting from referencing the pulse amplitudes was 552. An additional benefit of using this method was the elimination of errors which may have arisen from attempting to fit non-uniform pulses.

Once a reference protocol had been established, a program was written in LabVIEW 7.0 to automatically extract pulse amplitudes from *.sdf* file folders, thus saving time by removing the need to convert and open each *.sdf* file. Incorporating a program that was developed by Martin Bruckerscheifer (Georgia Institute of Technology) that translated *.sdf* files, the program was run post-experiment on the folder containing the experimental scans, extracting the MCT detector and reference pulse amplitudes and writing both datasets to a text file. The data was then readily plotted using Microsoft Excel or Microcal Origin.

5.3.2 Liquid Sensing

(a) Water Sensing with Evanescent Wave Spectroscopy

An unclad silver halide ($AgCl_{0.40}Br_{0.60}$) fibre of diameter 700μm was used to carry out fibre optic evanescent wave spectroscopy (FEWS) of liquid water. Water and

methanol mixtures were generated by injecting a set amount of water using a pipette into a volumetric flask, which was then topped up to the set volume mark with methanol.

The results of analysing the series of water and methanol mixtures are presented in Figure 5.14. There was visible reduction in signal due to increased evanescent water absorption, but the repeatability was hindered due to adsorbtion of water onto the fibre surface. Normalizing each series to its zero analyte concentration (0%) highlighted the similar intensity drops from sequential injecting (Figure 5.15).

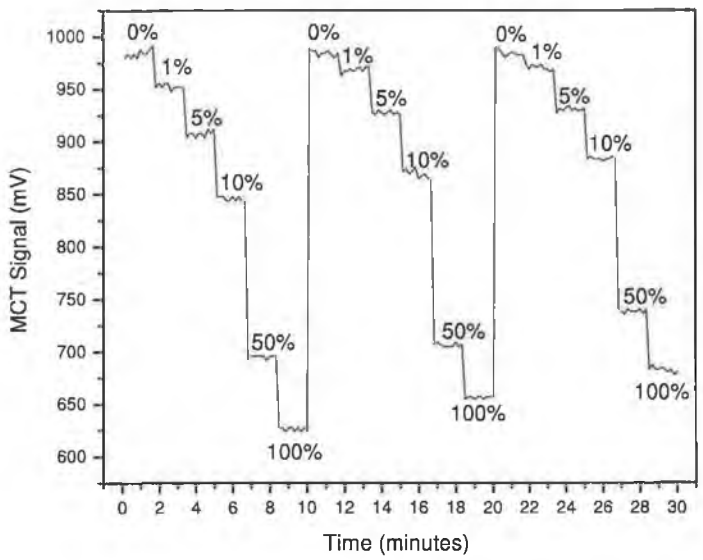

Figure 5.14: FEWS water/methanol series

Absorbance data were derived from the non-normalised scan series, using a new zero intensity I_0 for each of the three scans to calculate absorbance A from the Beer-Lambert Law. The absorbance results of the water FEWS experiment with the $\lambda = 6\mu$m DFB-QCL are presented in Figure 5.16. A linear relationship was seen for concentrations less than 10%. For higher concentrations, the absorbance deviates from the Beer-Lambert relationship, a well known effect attributed to increasing number of molecular interactions at high concentrations. A LOD of 0.640% water concentration by volume was calculated. In this case, the error bars correspond to the error in repeating the experiment. Sensor repeatability was limited by water adsorption onto the surface of the fibre, thus interfering with the evanescent field propagating into the solution. Insertion of the fibres into the flow cell and sealing with Teflon septa occasionally led to small bends

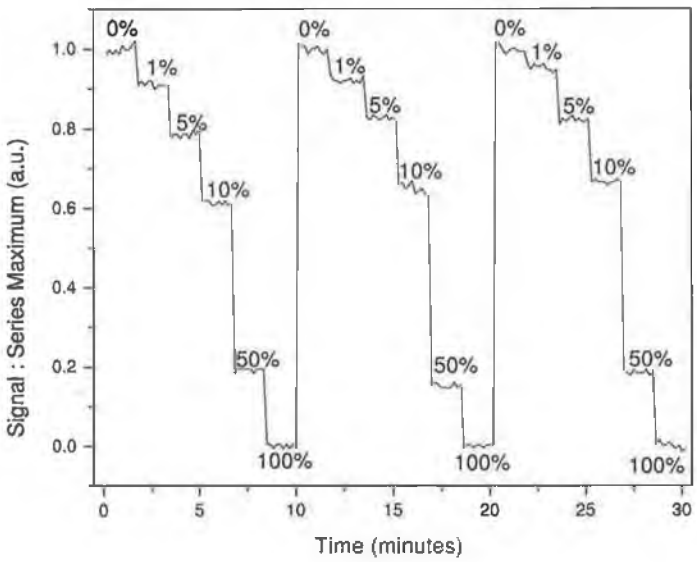

Figure 5.15: Normalised water absorption series

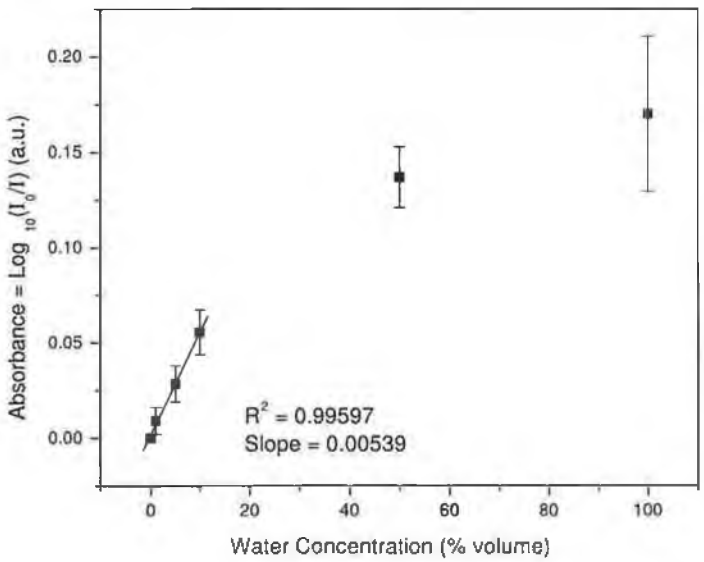

Figure 5.16: Evanescent absorbance of water

("kinks") in the fibre, degrading the IR transmission.

Aging effects also contributed to fibre degradation. Optimising the coupling between the focused laser light onto the fibre end was difficult as the MCT detector and coupling optics had to be aligned correctly to fully ascertain the level of QCL light entering the fibre. Alignment was initially estimated for the whole

fibre arrangement and then positional fine tuning of the mirrors, laser, detector and fibre ends was carried out. Due to the labour intensive nature of the optical alignment, fibres were often left in the flow cell for long periods of time. Although the glass cell protected fibres from UV exposure, repeated experiments with solvents and water accelerated the natural aging of the fibres. Blackening of the fibre end-faces was also seen on occasion, indicating surface degradation due to UV exposure.

(b) Acetic acid Sensing in Liquid Cell

Acetic acid in solution with ethanol was analysed with the $\lambda = 5.625\mu$m FP-QCL using the 150μm-long NaCl windowed open path cell. The Saturn FastScan DAQ system was used to sample and analyse the MCT detector signal. Acetic acid was injected into 100ml volumetric flasks using a range of pipettes and ethanol was used to dilute the samples by filling the volumetric flasks. Continuous flow analysis was made possible by employing a peristaltic pump to deliver samples to the cell. Absorbance data for concentrations in the range 0.5–10% (volume) are shown in Figure 5.17. Linear absorbance was seen for this concentration range in accordance with the Beer-Lambert Law, with a LOD of 1.255% by volume. Using the acetic acid and ethanol densities of 1.049 and 0.789g/ml, this can be expressed in terms of mass as 1.667%.

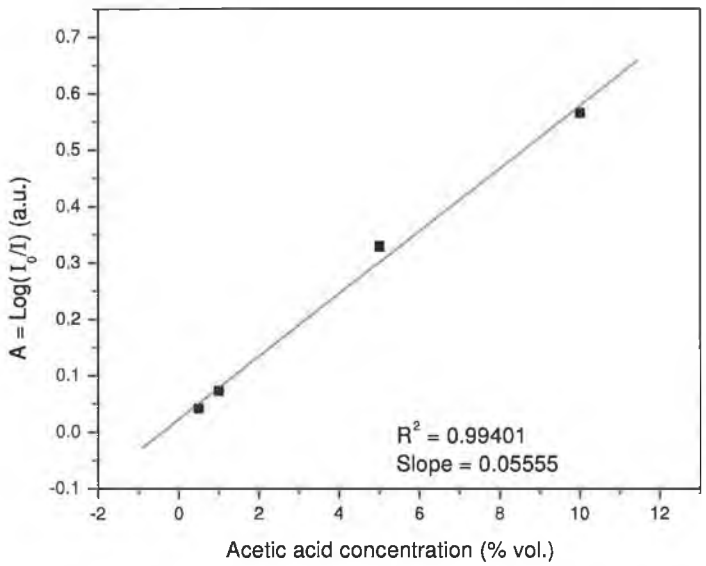

Figure 5.17: Acetic acid absorbance in 150μm open path cell

The sensitivity of the sensor could be increased by using a longer optical path length, enabling detection at lower concentrations. The calculated LOD for a 1mm OPL is 0.188% by volume, assuming no change in the zero concentration signal noise.

5.3.3 Gas Sensing

(a) Propylene Sensing with Hollow Waveguide

The 55.6cm long, 2mm inner diameter Ag/AgI silica hollow waveguide was used in conjunction with the $\lambda = 6\mu$m DFB-QCL to sense propylene. Propylene was extracted from a gas bag using a 10μl gas syringe and injected into a sealed air-filled volumetric flask of total volume 211ml. By varying the volume of propylene injected into the flask, a range of propylene concentrations in air were generated. A LOD of 3.71 parts per million by volume (ppmv) was calculated from the absorbance data shown in Figure 5.18.

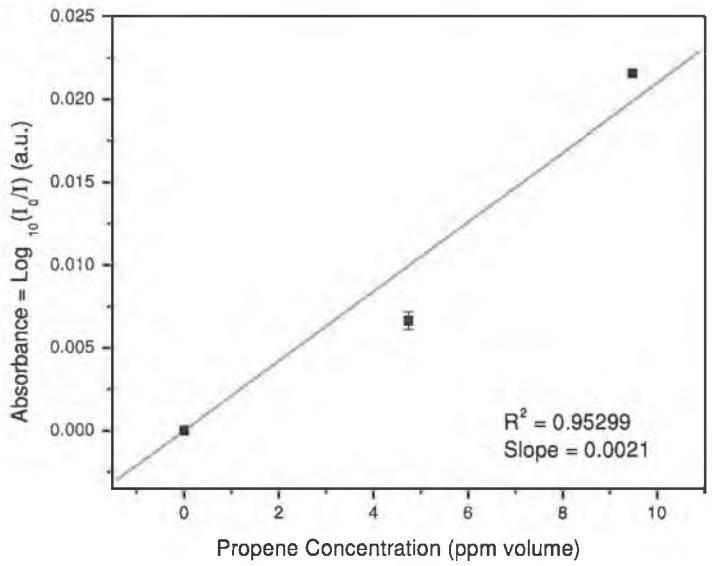

Figure 5.18: Propylene absorbance in 2mm i.d. HWG

Sensing higher concentrations of propylene in air was hindered by the mixing procedure. Ambient air was drawn into the mixing volumetric flask through the creation of a partial vacuum due to sample extraction, thus diluting the propylene concentration. Water vapour in the air used for generating mixtures may also have contributed to spurious absorptions.

(b) Formaldehyde Sensing in Open Path Cell

Two masses of paraformaldehyde, 1.8 and 3.7mg, were sublimated at 150°C under a nitrogen atmosphere to produce gaseous formaldehyde mixtures. Both the sublimation apparatus and the open path gas cell were purged with nitrogen and sealed before heating, so that a fixed volume of formaldehyde was present in the gas OPC during the experiment. The total volume of the gas OPC and the sublimation apparatus was 108.25ml, resulting in a molar concentration of 1.363% and 2.802% for the 1.8 and 3.7mg masses, respectively.

The $\lambda = 5.625\mu$m FP-QCL was used to interrogate the formaldehyde mixtures and the Saturn FastScan DAQ system was used to interpret the results using pulse amplitude referencing (Figure 5.19). The reduction in absorption from an initial maximum value can be attributed to cooling of the formaldehyde in the OPC, leading to recrystallization of the formaldehyde on the inner cell walls. This was confirmed as being the case using a FTIR spectrometer (Figure 5.20), where the formaldehyde absorbance at $\lambda = 5.67\mu$m was seen to increase as the paraformaldehyde sublimated. It reached a maximum absorbance value and then decreased over time. Due to the limited number of scans undertaken with the QCL, absorbance data were not compiled for formaldehyde sensing with the open path cell.

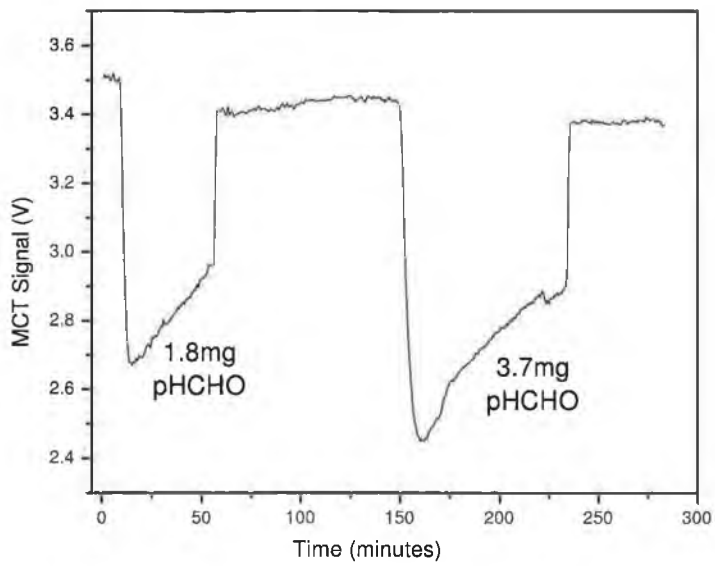

Figure 5.19: Sublimated paraformaldehyde absorption in 10cm open path gas cell

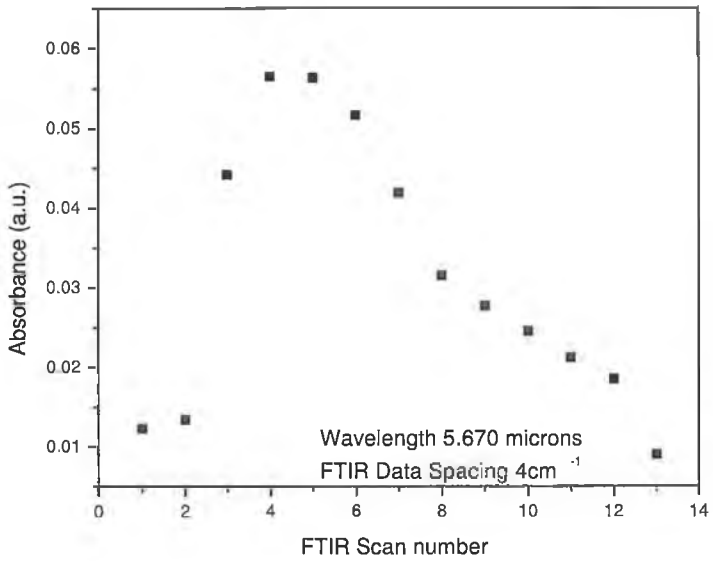

Figure 5.20: Absorbance of cooling formaldehyde

(c) Acetone Sensing in Open Path Cell

A gas mixing apparatus was constructed to generate gaseous samples of acetone at room temperature. By bubbling nitrogen through a sequence of three liquid acetone-filled gas bottles using a mass flow controller (MFC), acetone-saturated N_2 was generated. The maximum acetone content of the mixture was 34% (by molarity), the acetone saturation limit in N_2. This was then diluted using a second N_2 MFC, allowing a molar concentration range of 1.19–34.0% to be generated.

The capability of the 5.625μm FP-QCL as a spectroscopic source for acetone sensing was assessed using the open path gas cell. The Saturn FastScan DAQ system was used to acquire the MCT detector signal and to reference out laser intensity variations with pulse amplitude referencing.

The results of analysing mixtures in the 0–34.0% range, corresponding to 0–100% acetone-saturated N_2 and dry N_2 mixing ratios, are presented in Figure 5.21. The slower system response at the 1.7% level is attributed to the N_2 not being fully saturated with acetone.

Absorbance data were derived (Figure 5.22) and a LOD of 0.132% molar concentration was calculated. The absorbance at concentrations greater than 13.6% (a mixing ratio of 40%) was seen to deviate from the Beer-Lambert Law, similar to the effect seen in high concentration evanescent wave spectroscopy of water samples.

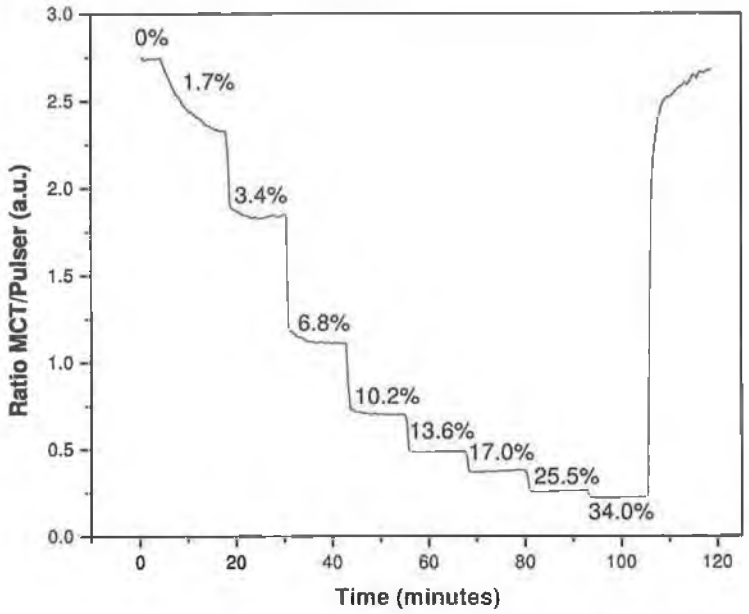

Figure 5.21: IR absorption of gaseous acetone in N_2 in open path gas cell, using averaged pulse amplitude referencing

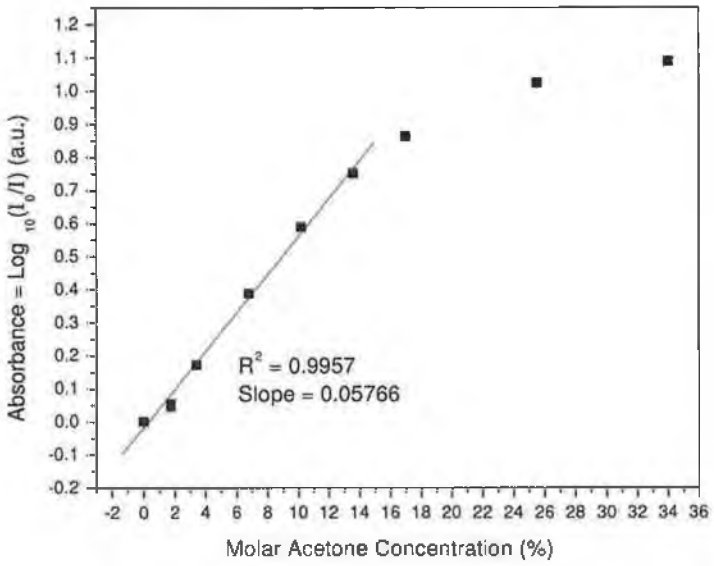

Figure 5.22: Acetone absorbance in 10cm open path cell

(d) Acetone Sensing in Hollow Waveguide

One method of increasing the sensitivity and lowering the limit of detection is to increase the optical path length L, as absorbance is proportional to L (at

low concentrations). The 10cm long gas OPC was replaced with a 89.9cm long, 0.7mm inner diameter Ag/AgI silica hollow waveguide. Gaseous acetone was used to determine the sensing performance of the FP-QCL and HWG, using the same gas mixing apparatus described in the previous section.

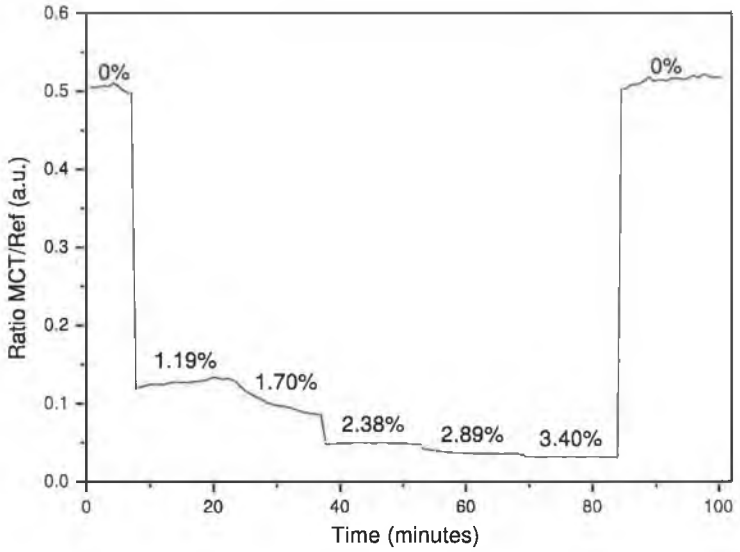

Figure 5.23: IR absorption of acetone/N_2 mixtures in 0.7mm i.d. HWG, using averaged pulse amplitude referencing

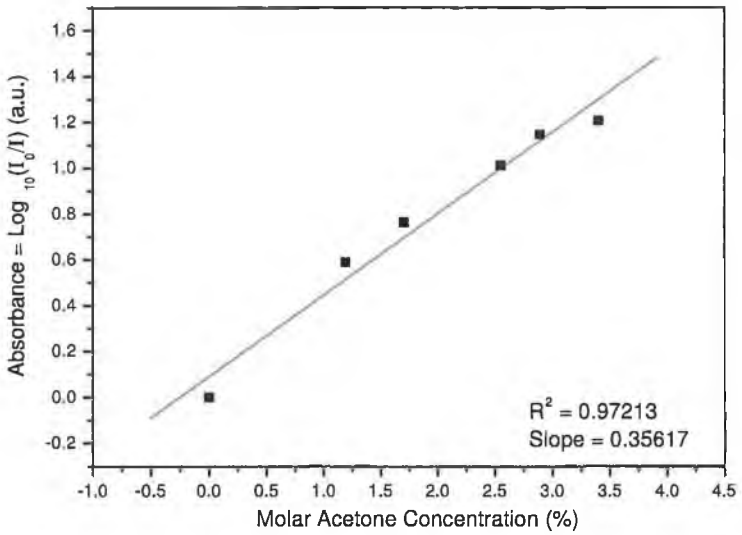

Figure 5.24: Acetone absorbance in 0.7mm i.d. HWG

Absorption and absorbance data from the acetone HWG experiment are pre-

sented in Figures 5.23 and 5.24 for an acetone concentration range of 0–3.4%. A LOD of 0.028% or 280ppm (molar) was calculated for sensing gaseous acetone in the HWG.

5.4 Summary

The outcomes of a number of experiments demonstrating different sensing configurations have been presented. By refining the optical configuration developed for the Laboratory-based Prototype and implementing temperature monitoring, a LOD of 3.71% RH was achieved with the ZBLAN:Tm^{3+} fluorescence spectroscopic sensor. Although RHs levels up to 100% were sensed successfully, extensive N_2 purging of the sensor head was required due to condensation at high RHs. Further optimisation of the amplification electronics and extension of the optical path length would facilitate lowering the LOD in conjunction with detector temperature referencing. Referencing with the pump laser beam was not found to appreciably improve signal to noise ratios.

MIR spectroscopy was performed using two quantum cascade lasers, the latter of which was used in conjunction with a pulse amplitude referencing system to reduce the effects of laser intensity fluctuations caused by driver current noise. A four-fold SNR improvement was achieved using pulse amplitude referencing.

Fibre optic evanescent wave spectroscopy was implemented with the DFB-QCL, ultimately leading to a wide detection range of <1%–100% water in methanol by volume. Although the repeatability was not optimal due to degradation of the silver halide fibre over time, the system achieved sufficient sensitivity to monitor water concentrations in solvents, a key requirement of pharmaceutical drug manufacturing where solvents are spiked with water to induce crystallisation.

Using a similar optical configuration, absorption spectroscopy with hollow waveguides was carried out with both lasers. Propylene and gaseous acetone were analysed, two environmentally and medically relevant gases. Although the propylene sensor was capable of sensing in the lower region of exhaust propylene concentrations i.e. 0–1000ppm [5] with a LOD of 3.42ppmv, further development of the sensor was halted when the DFB-QCL was damaged during inspection. Acetone was sensed in a molar concentration range of 0.028–34%, but as the minimum recorded distinction between acetone levels in normal and diabetic breath is 0.95ppmv [4], further work is required to fully realise the potential optical sensing poses for diabetic breath analysis and monitoring.

Open path cells were used for absorption spectroscopy with the FP-QCL ex-

clusively. Formaldehyde sensing was carried out using sublimated paraformaldehyde but crystallisation upon cooling affected the stability of the gas mixture in the cell. In spite of this, concentrations of 1.363% and 2.802% by mass were sensed. However to reach the levels required for atmospheric monitoring or medical applications, a more reliable formaldehyde generation technique would have to be pursued. Gaseous acetone was also detected using the same 10cm cell as a preliminary test prior to conducting acetone HWG experiments. Liquid sensing was performed on acetic acid samples in ethanol, achieving a LOD of 0.188% by volume.

It has been established that infrared spectroscopic sensing can be applied to a wide range of applications e.g humidity sensing, solvent water content monitoring, and trace biomarker analysis. A relative humidity sensor, suitable for industrial deployment, has been developed based on NIR Tm^{3+} fluorescence. A robust and versatile optical configuration has been implemented for coupling divergent QCL emission into a range of waveguides for spectroscopic sensing. These include silver halide optical fibres, hollow waveguides, and liquid and gas open path cells. The effects of pulse-to-pulse laser intensity fluctuations have been minimised by implementing pulse amplitude referencing.

Bibliography

[1] http://vpl.ipac.caltech.edu/spectra/frontpage.htm

[2] McNaught A.D. and Wilkinson A., *IUPAC Compend. Chem. Terminology (2nd Ed.)* (1997)

[3] Thomsen V., Schatzlein D. and Mercuro D., *Spectroscopy* **18 (12)** 112–114 (2003)

[4] Deng C., Zhang J., Yu X., Zhang W. and Zhang X., *J. Chrom. B* **810** 269–275 (2004)

[5] Wu M.C. and Micheli A.L., *Sensors and Actuators B* **100 (3)** 291–297 (2004)

Chapter 6

Discussion, Conclusion and Further Work

6.1 Overview

The objective of this thesis was to apply novel infrared optical sources to a variety of optical sensing roles, including relative humidity sensing and trace chemical analysis. A number of potentially important industrial and diagnostic applications have been demonstrated. This was accomplished by using rare-earth doped glass NIR fluorescence to detect the moisture content of a gas, and by designing and constructing a flexible optical configuration for use with MIR quantum cascade lasers to sense a variety of analytes in gas and liquid phase.

In terms of the relative humidity (RH) sensor, a device suitable for industrial deployment,the Industrial Prototype, was developed following the proof-of-concept work carried out with the Laboratory-Based Prototype. The fluorescence of Tm^{3+} in a ZBLAN glass bead was successfully used as a spectroscopic source for sensing RH. Through refinement of the optical and electronic components, temperature stabilisation of the detector and stable RH measurements were carried out in nitrogen.

Two quantum cascade lasers were used to develop MIR spectroscopic sensors. A distributed feedback quantum cascade laser (DFB-QCL) emitting at 6.0μm was incorporated into a fibre optic evanescent wave sensing platform for detecting water in methanol, demonstrating the laser's capability for sensing the water content in solvents. Pharmaceutical drug manufacturing relies on water-spiking solvents to generate crystallisation, and requires a continuous method of sensing water in a chemically active and dynamic environment. Although a large water concentration range was detectable with the silver halide fibre optic sensing ap-

proach (<1%–100% by volume), the repeatability of the evanescent wave sensing system was restricted by surface water adsorption and fibre aging. One potential solution to this problem would be to adopt an alternative, more robust fibre optic material e.g. sapphire.

The DFB-QCL was also used with a hollow waveguide (HWG) to sense gaseous propylene. The QCL hollow waveguide experiment was very sensitive to low (ppmv) propylene concentrations, though there was an issue with the repeatability of the gas mixing.

A Fabry-Perot laser (FP-QCL) was used in open path and HWG absorption spectroscopy to detect acetic acid, acetone and formaldehyde, all of which are important breath biomarkers. Acetic acid in the breath is related to liver function impairment, acetone is a well-known component of diabetics' breath, and formaldehyde is linked to a number of cancers.

A pulse amplitude referencing system was designed to reduce the effect laser driver pulses had on pulse-to-pulse laser intensity. An investigation into this effect using a two-channel data acquisition system, the Saturn FastScan system, revealed that the QCL intensity fluctuations matched pulse amplitude shifts in the QCL pulse generator. This was used as the basis of a referencing regime to compare and correct MIR absorption data.

A summary of the results attained in this work is provided in Table 6.1.

6.2 Future Work

The DFB-QCL laser was damaged shortly after the propylene HWG experiments were carried out, so the majority of the ideas proposed in this section refer to the FP-QCL.

To better address the needs of medical breath diagnosis, improvements in the minimum detectable sensitivity currently attainable with QCL absorption spectroscopy must be implemented. This is due to the very low concentrations of biomarkers in exhaled breath (ppm–ppb). Increasing the optical path length is one method of achieving this. The longest path length used in the work described here was 89.9cm (for detecting acetone with a LOD of 280ppm), but to detect lower concentrations either a longer waveguide or an alternative optical configuration (e.g. using a multiple reflection, multi-pass cell) must be used. Using a longer waveguide may prove unwieldy in the case of HWGs, as they suffer bending losses. An alternative waveguide that does not is the omnidirectional hollow waveguide, based on photonic bandgap fibre technology. This could be

Analyte	Technique	LOD	Range
Relative Humidity	ZBLAN:Tm^{3+} NIR fluorescence	3.71% RH	0–100% RH
Water	FEWS with 6μm DFB-QCL	0.64% (vol.)	0.1–100% (vol.)
Acetic acid	150μm OPC and 5.625μm FP-QCL	1.255% (vol.)	0.5–10% (vol.)
Propylene	2mm i.d. HWG and 6μm DFB-QCL	3.42ppmv	0–9.5ppmv
Formaldehyde	10cm OPC and 5.625μm FP-QCL	n/a	1.4–2.8% (molar conc.)
Acetone	10cm OPC and 5.625μm FP-QCL	0.132% (molar conc.)	1.19–34.0% (molar conc.)
	2mm i.d. HWG and 5.625μm FP-QCL	280ppm (molar conc.)	1.19–3.40% (molar conc.)

Table 6.1: Summary of chemicals detected using rare earth NIR fluorescence and QCL spectroscopy.

investigated as a suitable waveguide and gas confinement system for producing a hand-held clinical diagnostic device using QCLs.

Another method of improving sensitivity would be to enhance the spectral overlap between laser and analyte. QCLs can be temperature-tuned by changing the heat-sink temperature or by changing the DC voltage driving the laser. In practice, both methods have the effect of heating or cooling the laser. For DFB-QCLs, temperature tuning is due mainly to the refractive index temperature dependence of the Bragg grating period, giving in a temperature shift of 6×10^{-5}/K for wavelength. As the operating range of Alpes Lasers' QCLs is 60°C (60K, defined by the Peltier cooler range of ±30°C), this results in a tuning range of approximately 0.4% of peak emission wavelength. For FP-QCLs, tuning is accomplished by the temperature dependence of the device gain, which is manifested as a wavelength change of 1.3^{-4}/K and results in a wider tuning range of 0.8% over a 60K range.

Shifting the laser wavelength could be implemented relatively simply by changing the heat-sink temperature or the DC supply, but true optimisation would have to take into account the optical power loss that modifying the QCL operating parameters could bring about; higher optical powers are achieved for lower temperatures and higher DC voltages, but the laser emission wavelength may not overlap

adequately with an analyte's absorption feature. A full spectral characterisation would be required to fully exploit this aspect of QCLs.

To improve gas mixing, the use of commercially-supplied gases and mass flow controllers (MFCs) would undoubtedly bring about a marked improvement in mixing repeatability and stability. For some analytes, a difficulty may lie in the cost of getting MFCs calibrated for accurate analyte delivery and flow control, and for combined analyte and N_2 mixtures to facilitate dilution to ppm or ppb levels.

An aspect of the pulse amplitude referencing that deserves further investigation is the averaging of scans and triggering. One million samples per average were sampled for both the infrared signal from the MCT detector and the reference signal from the TPG128 pulse generator. This contributed to a lengthy response time ($\sim$ 45s) which would be sufficient for some applications e.g. atmospheric monitoring but unsuitable for sensing analytes in dynamic environments e.g. in exhaust fumes. While decreasing the number of samples per average scan would undoubtedly decrease the response time of the system, this would also decrease the SNR. A more viable alternative would be to disable the Saturn FastScan's system log generator. A significant portion of the measurement duration is taken up with the FastScan software exporting the averaged signals and generating a log file. According to AMO GmbH, the fastest measurement duration for a single channel recording 10^6 samples/average is 2.56s, so there is ample scope to improve the sensor response.

6.3 Conclusion

The objectives set out at the beginning of the thesis have been completed. A relative humidity sensor, capable of industrial deployment in the present configuration, was developed based on the spectral overlap between the NIR absorption spectrum of water and Tm^{3+}-doped glass fluorescence at 1.83μm.

The spectroscopic capabilities of quantum cascade lasers have been verified in a number of sensing configurations. These include fibre optic evanescent wave spectroscopy of water in solvents, direct absorption spectroscopy of acetic acid, formaldehyde and acetone, and hollow waveguide absorption spectroscopy of propylene and acetone. Although some further development is required to increase sensitivity, the SNR, and repeatability (in the case of the FEWS water experiment), the viability of QCLs as potential spectroscopic sources for MIR sensing applications has been demonstrated.

Appendix A

685nm Laser Diode

LASER 2000

CERTIFICATE OF CONFORMITY

Year 2000 OK compliant product and services

Hugh Masterson Dublin City University Glasnevin Dublin 9 Ireland	Order no: 103201196 Laser 2000 Ref: H0178/P002680 Date: 21-Jan-02

Item Description	Serial No.	Test Specification	
PMTLD1217 (Labelled as PMT45/5623)	J 020840	Laser Diode Manufacture Info.	
		Threshold Current	40TYP mA
		Maximum Power	60 mW
		Diode Current	110TYP mA
		Diode Monitor I Im	N/A mA
		Wavelength	685.0 nm
		Readings at Max. Power Out	
		Optical Output Power	45.5 mW
		Module Input I	192.8 mA
		Laser Diode Operating I	109.7 mA
		Laser Diode Monitor I Im	N/A
		Focal length	5.00 Feet

Certified that the whole of the supplies detailed hereon have been inspected, tested and unless otherwise stated above, conform in all respects to the requirements of the order.

Signed: Date: 21-01-02

Lasers • Optics • Fibre Optics • Instrumentation

INVESTOR IN PEOPLE

Figure A.1: Test data sheet for 685nm laser diode used for initiating fluorescence in ZBLAN:Tm^{3+} glass bead at $\lambda = 1.83\mu$m

LASER 2000

TP-PMT/01-8/95 Page 1 of 1

Model "PMT" LASER DIODE OEM SYSTEM INSTRUCTIONS
GENERAL OPERATION - EXTERNAL TTL MODULATION

Introduction

These Laser Diode OEM Systems are designed for external TTL compatible modulation from CW to 20MHz.

Operation

The system operates on 5VDC input only. In operation, the standard system provides a constant current, preset at the factory, to the laser. So, the laser output power is fixed and will vary only with environmental changes. The system does not have a feedback system to regulate the laser power. So, the system will not automatically adjust for these changes. *See the section below concerning optional drive current controls.*

Note: Since the system drives the laser at a constant current, you need to understand the implications of the temperature and laser power correlation. As temperature decreases, the laser power increases. At the same time, the laser's current rating decreases. So, the possibility of a laser burn-out is increased as the temperature drops due to the preset drive current (or current adjustment with Option X22) exceeding the drive current capacity of the laser. There are a couple of methods to avoid this outcome. You can maintain a constant ambient temperature or, optionally, you can monitor the laser power and adjust the Option X22 current control to keep the laser output power under the maximum rating of the system.

Since the modulation is TTL, the external pulse generator operation must toggle between 0VDC and 5VDC. The system can be operated CW (with 0VDC on the data input) or pulsed up to 20MHz. The system will not operate until the coaxial connector is attached to a pulse generator, or a shorted termination (which allows the system to operate CW).

Optional Drive Current Control:
The Option X22 is a ¾ turn potentiometer located on the end of the system. This enables the user to adjust the drive current to the laser and therefore change the output power from zero to 100% of the rated power of the system. There is also an Option D2 which enables the current to be digitally controlled. If you have this option, then you need to refer to those separate instructions.

Caution: **Check the operating range of the power meter before setting the power. Most photodiode based meters will saturate at 2mW (without an external attenuation). Although some digital meters will indicate power greater than 2mW, this reading is usually in error with the meter always giving a reading below the actual power. Also, because the system is modulated the meter will not give a true reading. For the true laser power you must factor in the pulse width and the pulse frequency.**

Installation

Do not mount the system in a thermal insulating material, such as foam plastic. For best heat dissipation use a metal mounting fixture. A heatsink is recommended for operating temperatures above 25°C.
Heat generation can also be a problem on systems that have an output power of 5mW or greater or, that have 70mA or more of current drawn by the laser. *If either of these conditions exist for your system then a heat sink is recommended to prevent damage to the laser diode.*
The TTL modulation signal is transmitted to the system via a single coaxial cable (provided by the customer) connected to the male SMC connector located on the end of the system. A female SMC connector, and assembly instruction sheet, is provided for the customer to assemble an SMC to BNC cable (< 0.5m length recommended).

Warranty Notes:

Sealed Locking Ring: The laser diode is held in place with a locking ring. This locking ring is factory sealed. It is necessary to remove the lens in order to gain access to this ring. So, accidental breaking of this seal is unlikely.

Breaking the seal on this locking ring voids the warranty.

Lasers • Optics • Fibre Optics • Instrumentation

Figure A.2: Specification sheet for 685nm laser diode

Appendix B

PbS Photoconductive Quad Detector

CAL-SENSORS — Detector Test Data Report — Page 1 of 1

CUSTOMER: DUBLIN CITY UNIV. /IE
P.O: 59050
MODEL #: AT1S-18T(M)-4
CSI M.O.#: 13556
REL #: 01
TEST DATE: 11/28/2001

HEATSINK TEMP: 25. °C
BLACKBODY TEMP: 500. °K
FLUX DENSITY: 1.35E-05 watts/cm²
DETECTOR AREA: .01 cm²
DETECTOR TEMPERATURE: -20 °C
NOISE BANDPASS: 7.85 Hz
MODULATION FREQUENCY: 650. Hz
BIAS VOLTAGE: 50. VDC
LOAD RESISTOR: 1. MegOhms

Pk/BB CONVERSION FACTORS:	det 1	det 2	det 3	det 4
	149.70	1942.80	1942.80	149.70

PKG. UNIT #:	DET #:	Cooler Power Volt	Cooler Power Amp	Thermistor Resistance (KΩ) ambient	Thermistor Resistance (KΩ) cold	Detector Resistance (MΩ) ambient	Detector Resistance (MΩ) cold	Detector Signal (μV)	Detector Noise (μV)	Calculations S/N	Calculations Resp. (Volts/Watt)	Calculations D* (Cm·Hz^½·W⁻¹)
148	1	1.44	.97	1.30 +25°C	6.77 -20°C	1.30	4.64	2850	2.80	1018	3.15E+06	3.18E+11
	2					1.46	4.71	200	2.60	77	2.87E+06	3.09E+11
	3					1.33	4.46	215	2.80	77	3.09E+06	3.09E+11
	4					1.58	4.74	2350	2.60	904	2.60E+06	2.60E+11

Figure B.1: Test data sheet for PbS quad detector used in ZBLAN:Tm^{3+} fluorescence-based RH sensor

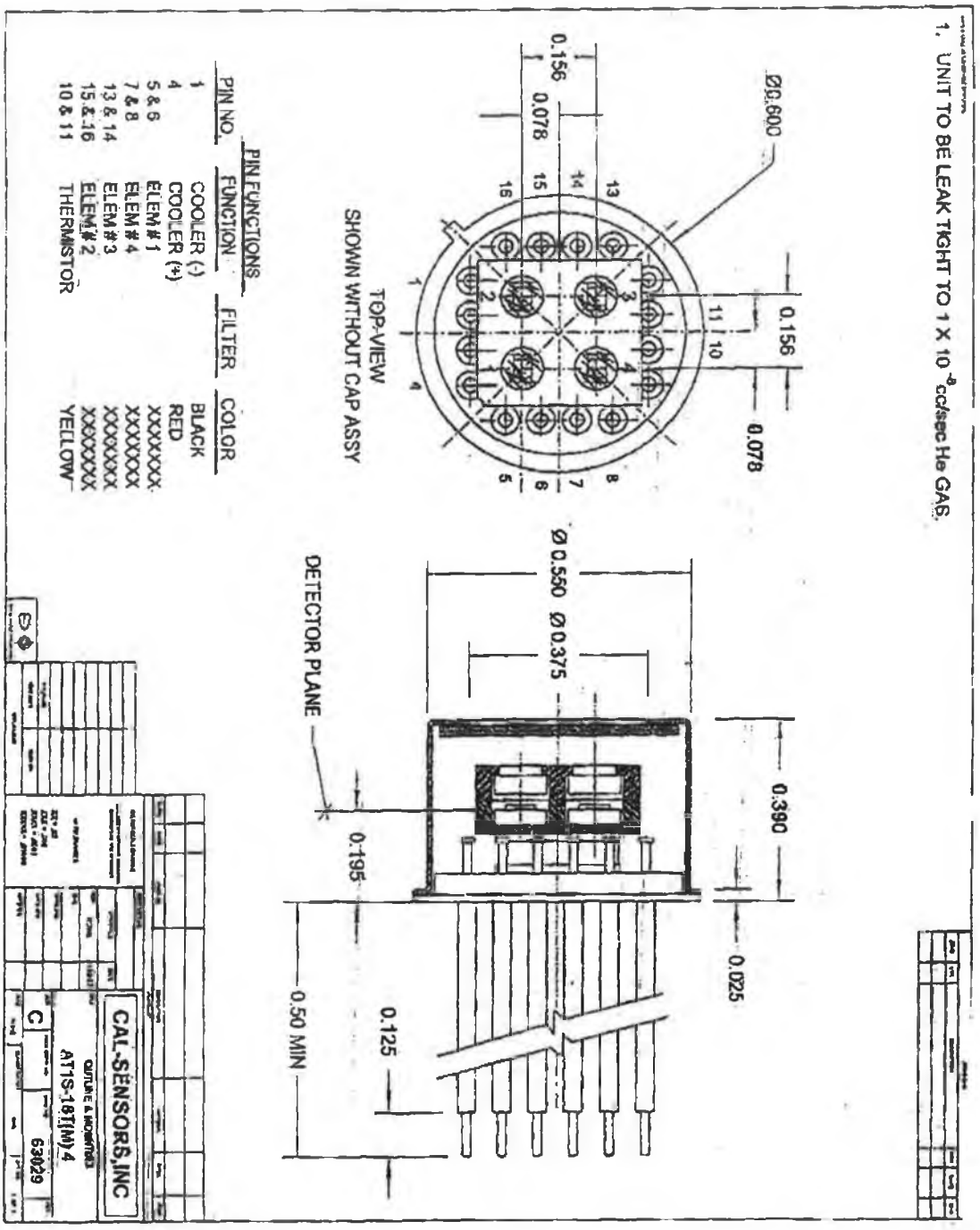

Figure B.2: Specification sheet for PbS quad detector

Appendix C

HgCdTe (MCT) Photodiode Detector

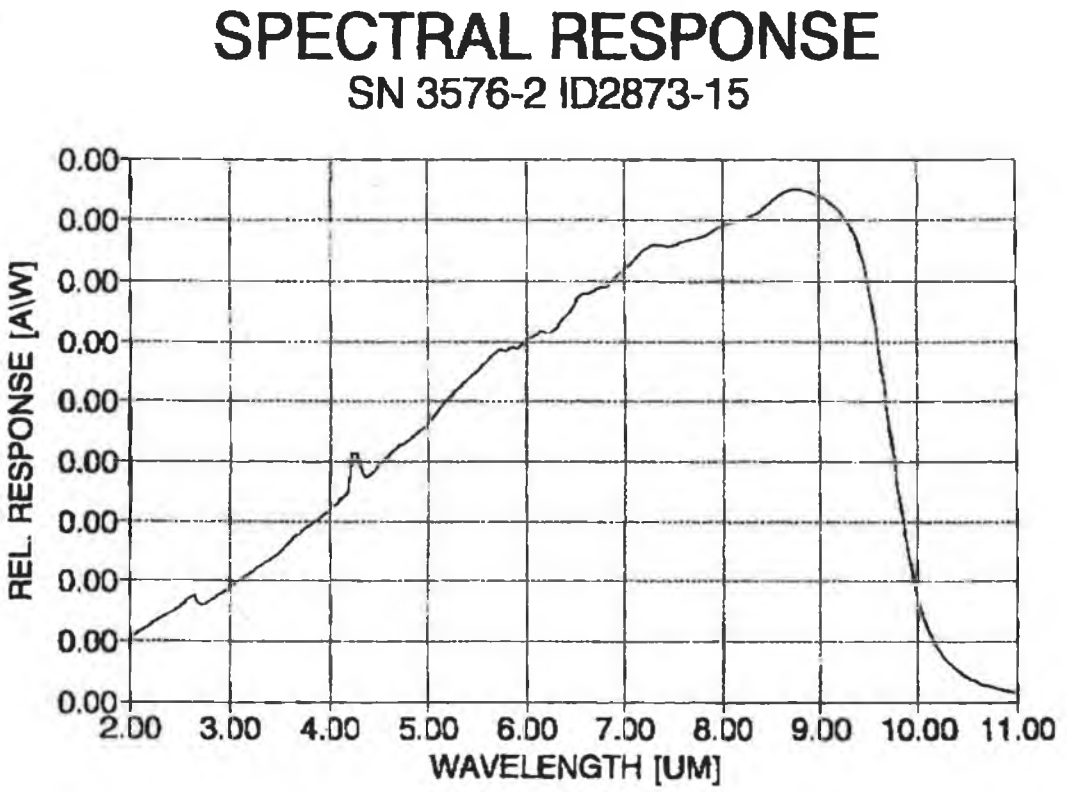

Figure C.1: Spectral response of MCT detector.

KOLMAR TECHNOLOGIES

Series KMPV HgCdTe Photodiodes with Integral Amplifiers

Features

- **High D* at high frequencies**
- **Bandwidth to 50 MHz**
- **Fast risetime: 7ns**
- **Sizes 2.0 mm to 0.05 mm**
- **Wavelength cutoff: 11.5, 8, 4.5 µm**
- **Linear**
- **Custom configurations available**

Applications

The KMPV is designed to be used in systems and instruments which require a very sensitive, linear, high speed detector/amplifier:

- Step-scan FTIR
- Time resolved spectroscopy
- Range finders
- Trace gas spectroscopy
- Chemical aerosols detection

Description

The KMPV series is an integrated high frequency infrared detector/amplifier sensor with wavelengths of 2µm to 12µm. The HgCdTe photodiode is coupled to an internal DC to 20MHz (or 50MHz) bandwidth transimpedance amplifier. The output can be ordered as DC, AC or both AC and DC. The broadband D* is greater than 1 x 10^{10} Jones. The standard Dewar is side-looking with a 10 hour hold time. The standard IR window is ZnSe anti-reflection coated for 2µm to 13µm.

The KMPV is designed for applications in which photoconductive HgCdTe detectors are beyond their capabilities: applications which require bandwidth greater than 1MHz or greater linear dynamic range with photon flux.

Spectral Detectivity

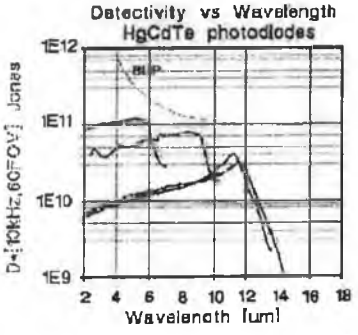

Frequency Response

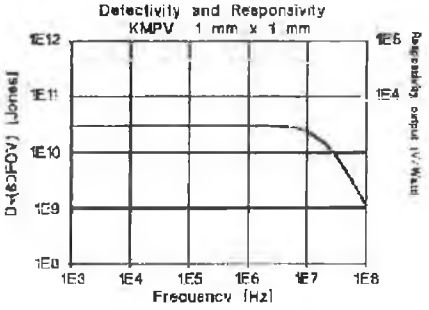

KOLMAR TECHNOLOGIES, INC.
3 GRAF RD. UNIT 9, NEWBURYPORT, MA 01950 USA
978 462 2905 - FAX 978 462 2893 email office@kolmartech.com

Figure C.2: Specification sheet for HgCdTe (MCT) photodiode detector used in QCL spectroscopy